# FREEFORM SOLAR CONCENTRATING OPTICS

by

Brian Wheelwright



A Dissertation Submitted to the Faculty of the

DEPARTMENT OF OPTICAL SCIENCES

In Partial Fulfillment of the Requirements

For the Degree of

DOCTOR OF PHILOSOPHY

In the Graduate College

THE UNIVERSITY OF ARIZONA

2015

THE UNIVERSITY OF ARIZONA
GRADUATE COLLEGE

As members of the Dissertation Committee, we certify that we have read the dissertation prepared by Brian Wheelwright, titled "Freeform Solar Concentrating Optics", and recommend that it be accepted as fulfilling the dissertation requirement for the Degree of Doctor of Philosophy.

_______________________________________________ Date: 8/3/2015
J. Roger P. Angel

_______________________________________________ Date: 8/3/2015
R. John Koshel

_______________________________________________ Date: 8/3/2015
Raymond Kostuk

Final approval and acceptance of this dissertation is contingent upon the candidate's submission of the final copies of the dissertation to the Graduate College.

I hereby certify that I have read this dissertation prepared under my direction and recommend that it be accepted as fulfilling the dissertation requirement.

_______________________________________________ Date: 8/3/2015
Dissertation Director: J. Roger P. Angel

## STATEMENT BY AUTHOR



SIGNED: Brian Wheelwright

**ACKNOWLEDGEMENTS**

I am indebted to my advisor and mentor, Roger Angel, for his tireless work in engaging students in the cause to reduce the cost of solar power through optical innovation. Roger's passion, creativity, and keen intellect have shaped me as a researcher and inspired this work. I also gratefully acknowledge the guidance and instruction of Optical Sciences professors John Koshel, Ray Kostuk, Jose Sasian, Jim Burge, and the Steward Observatory Mirror Lab staff. I would like to thank all of the students I've worked with over the years, especially Blake Coughenour, Rodolfo Peon, Andrew Geary, Kimberly Hammer, Justin Hyatt, Andy Whiteside, Dima Reshidko, Jon Weiser, JJ Mrkonich, and Mira Frenkel. For the past two years, I've had the great privilege of collaborating with ASU professor Zachary Holman. I thank him and his team, particularly Jason Yu and Kate Fisher, for the fruitful relationship our labs have cultivated.

I also acknowledge the generous support of the ARCS Foundation and my donors Christy and Daryl Burton. Since 2013 I have also enjoyed a generous NDSEG Fellowship without which I could not have pursued this line of research.

I gratefully acknowledge the TechLaunch Arizona Proof of Concept (POC) program, REN TRIFF Exploratory Grant program, and GPSC Research Grants, which have all provided seed funding to pursue new ideas. I also acknowledge funding from ARPA-E ("PV Mirror: A Solar Concentrator Mirror Incorporating PV Cells" #DE-AR000474), SunShot CSP ("Advanced Manufacture of Collectors" #DE-EE0005796), and Research Corporation (Grant #22171).

# DEDICATION

To Janny, whose endless love, encouragement, support, and sacrifice have motivated me take risks and work on problems that I’m passionate about. And to my parents who instilled a love of learning from a young age.

# TABLE OF CONTENTS

Page

# LIST OF TABLES

## LIST OF FIGURES

## ABSTRACT

Notwithstanding several years of robust growth, solar energy still only accounts for <1% of total electrical generation in the US. Before solar energy can substantially replace fossil fuels subsidy-free at utility scale, further cost reductions and efficiency improvements are needed in complete generating systems. Flat panel silicon PV modules are by far the most dominant solar technology today, but have little room for improvement in efficiency and are limited by balance of system costs. Concentrated PV (CPV) is an alternate approach with long-term potential for much higher efficiency in sunny climates. In CPV modules, large area optics collect and concentrate direct sunlight onto small multi-junction cells with >40% conversion efficiency. Concentrated Solar Power (CSP) uses mirrors to concentrate sunlight onto thermally absorbing receivers, which generate electricity with convention thermal cycles.

In this dissertation, four new optical approaches to CPV and CSP with potential for lower cost are analyzed. Common to each approach is the use of large square glass reflectors, which have very low areal cost (~\$35/m$^2$) and field-proven reliability in the

CSP industry. Chapter 2 describes a freeform toroidal lens array used to intercept the low concentration line focus of a parabolic trough to produce multiple high concentration foci (>800X) for multi-junction cells. In Chapter 3, three embodiments of dish mirrors and freeform lenslet arrays are explored, including an off-axis system. In each case, a dish mirror illuminates a freeform lenslet array, which divides sunlight equally to a sparse matrix of multi-junction cells. The off-axis optical system achieves +/-0.45° acceptance angle and averages 1215X geometric concentration over 400 multi-junction cells. Chapter 4 proposes a new architecture for CSP central receivers that achieves extremely high collection efficiency (>70%) with unconventional heliostat field tracking. In Chapter 5, the design and preliminary testing of a spectrum-splitting hybrid PV/thermal generator is discussed. This system has the advantage of 'drop-in' capability in existing CSP trough plants and allows for thermal storage, an important mitigation to the intermittency of the solar resource.

# CHAPTER 1: INTRODUCTION TO THE SOLAR RESOURCE

The pervasiveness of human impact on water, carbon, and nitrogen cycles leads many scholars to suggest that Earth is now in a new epoch, the Anthropocene, or Age of Humans. As human civilization continues to consume more energy, the use of conventional sources becomes untenable. Sunlight is by far the most abundant energy source available to mankind. This chapter introduces the solar resource and current methods of solar generation with concentration.

## 1.1 SOLAR SPECTRUM AND GEOMETRY

In the absence of atmospheric absorption, the solar spectrum very nearly matches the spectrum of a 6000 K blackbody. The solar spectrum reaching Earth's surface varies according to atmospheric conditions and the obliquity of the sun's rays through the atmosphere. Sunlight from zenith (straight up) passes through one air mass (AM1). Due to the curvature of the Earth's atmosphere, the effective air mass is a function of the Sun's zenith angle from vertical, $\theta_{ZA}$ (Kasten & Young, 1989):

$$AM = \frac{1}{\cos(\theta_{ZA}) + 0.50572(96.07995 - \theta_{ZA})^{-1.6364}} \quad (1.1)$$

AM0 refers to the extraterrestrial solar spectrum above Earth's atmosphere, and resembles the emission spectrum of a 5778K blackbody with known Fraunhofer lines from elemental absorption. AM1.5, a standard spectrum used in the PV industry, refers to the solar spectrum after passing through the atmosphere at an obliquity of ~48.8°.

Figure 1.1 plots three different solar spectra calculated with NREL's Simple Model of the Atmospheric Radiative Transfer of Sunshine (SMARTS). AM0, AM1.5, and AM10 are plotted using the same default turbidity, humidity, temperature, and other atmospheric parameters (see Appendix A). AM10 corresponds to a solar elevation of only 5º above the horizon, a common lower limit in solar fields. AM10 is significantly red-shifted compared to the AM1.5 spectrum. Note that Figure 1.1 only shows the direct sunlight component, or direct normal insolation (DNI). See Section 1.2 for a full discussion of the direct and diffuse components of the solar resource.

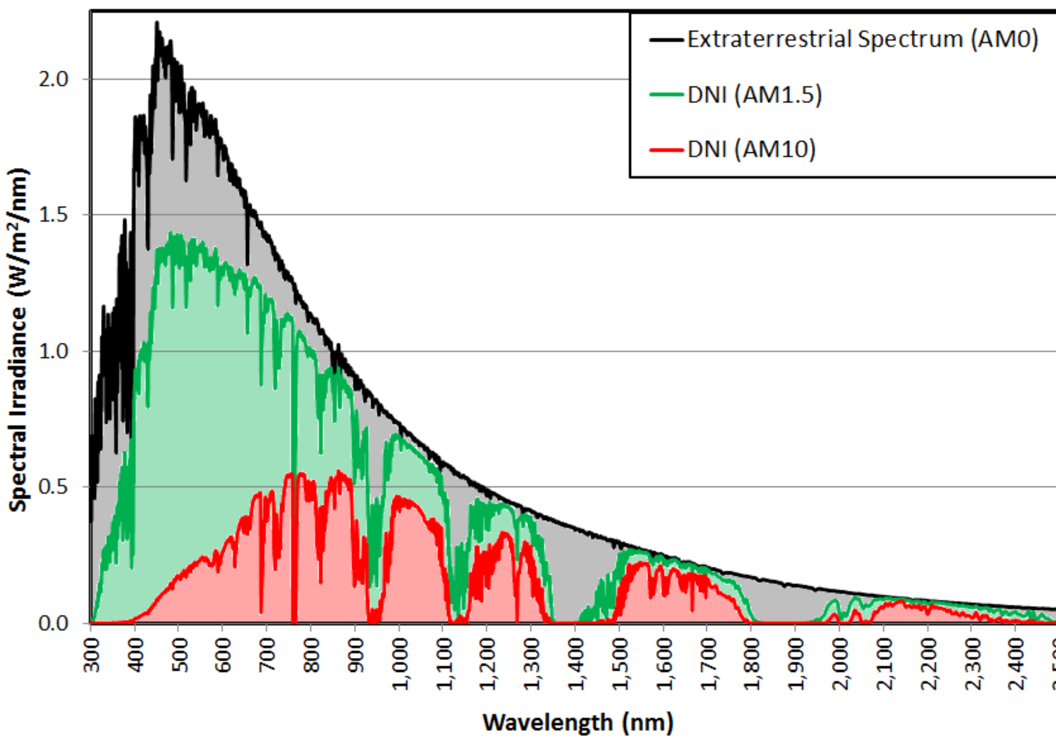


Figure 1.1: Solar spectra AM0, AM1.5, and AM10.

On average, the solar disk subtends +/-0.266º when viewed from Earth. For the purposes of this work, higher order effects such as the variable Earth-Sun distance can be ignored. Site latitude is the most important driver to the variations in solar path across the sky. In northern latitudes above the topic of cancer (φ>23.5°), the sun rises on the summer solstice to the northeast, transits to the south of zenith, and sets in the northwest. Between the fall and spring equinox, the Sun is always in the southern sky, transiting from the southeast to southwest. Figure 1.2 gives an illustration of the solar path in azimuth-elevation space for a typical site at northern latitudes.

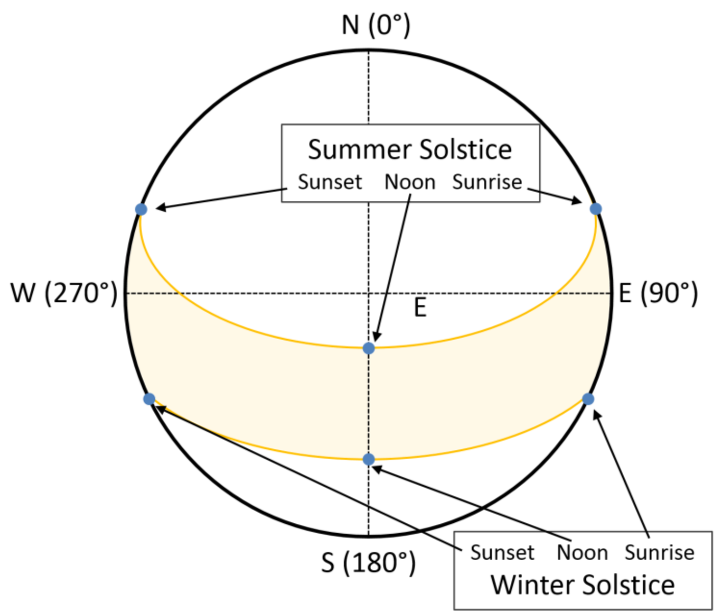


Figure 1.2: The solar path for a typical northern latitude.

A detailed understanding of the orbital geometry of the Earth/Sun is not required to design solar concentrators. It is sufficient to understand the boundary conditions for a given site.

## 1.2 Direct vs Diffuse Radiation

Direct sunlight, or Direct Normal Insolation (DNI), is light reaching the Earth's surface from a direction that can be traced back to the apparent position of the solar disk. In reality, direct sunlight does not take a straight path as it refracts through various layers of the atmosphere. Diffuse sunlight reaches the ground from an angle outside the solar disk. On a cloud-free day, the largest source of diffuse sunlight is the blue sky, caused by Rayleigh scattering. On hazy or cloudy days, the diffuse sunlight component is less blue. Figure 1.3 compares the annually averaged solar resource (black dashed line) and the fractional diffuse contribution (blue line) for a variety of observation sites in the US (ARPA-E, 2014). Note the general trend that lower-resource areas, such as Seattle, receive a greater fraction of sunlight that is diffuse. However, even in famously sunny sites like Tucson and Las Vegas, diffuse sunlight accounts for >20% of the total solar resource, averaged over the year. The implication of this significant diffuse fraction for concentrating systems will be discussed in greater detail in Chapter 5.

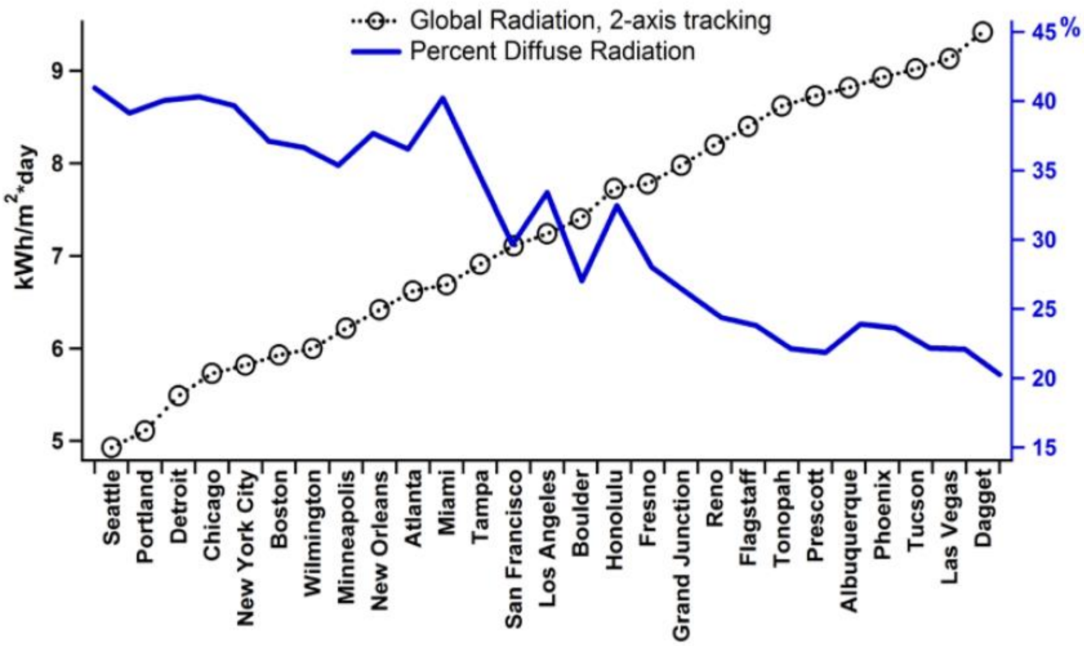


Figure 1.3: Solar resource and percentage diffuse contribution (ARPA-E, 2014).

### 1.3 TRACKING, CONCENTRATION, AND ACCEPTANCE ANGLE

Mechanical tracking increases the total solar resource collected on a given aperture. Non-tracking collectors, such as most roof-mounted PV systems, are usually south facing (if in the northern hemisphere) and tilted according to latitude. Where adjustments are practical, the tilt angle is optimized to maximize the solar resource while accounting for seasonal energy needs, local climate, soiling, and potential snow loading. The azimuthal angle of fixed-tilt modules may also be adjusted to boost morning output (eastern bias) or afternoon output (western bias). Without tracking, only very modest concentration is possible. An absolutely fixed concentrator which operates eight hours per day may only achieve ~4X concentration of direct sunshine while losing most diffuse radiation (Winston & Zhang, 2010). Since only modest concentration gains are possible without tracking, non-tracking modules usually do not incorporate concentrator optics.

Adding a single axis of tracking increases the maximum 2D concentration to

$$C_{max,2D} = \frac{n}{\sin(\theta_a)} \;, \tag{1.2}$$

where the receiver is immersed in a media of index *n* and the concentrator has half-acceptance angle $\theta_a$ (Winston, Minano, & Benitez, 2005).

*Optical acceptance angle* is usually defined as the angular range over which a concentrator maintains 90% optical power throughput. However, Equation 1.2 assumes 100% throughput. To reach this theoretical maximum, the receiver must be illuminated from a full hemispherical dome. In practice, target illumination at glancing incidence is avoided due to poor anti-reflection coating performance off-axis.

Concentrators with generous acceptance angles have the benefit of allowing coarser (and cheaper) mechanical tracking. While Equation 1.2 is the theoretical maximum 2D concentration possible, practical optical systems are not aplanatic, have inherent optical losses, and usually do not illuminate targets at high incidence angles.

Single-axis module tracking can take on multiple configurations, the most common being rotation about a polar-aligned axis (tilted by latitude) or about a horizontal axis with north-south orientation. Tracking about a horizontal axis with east-west orientation is also common, although this configuration is not considered here because the annual collection efficiency is comparatively low (NREL, Solar Radiation Data Manual for Flat-Plate and Concentrating Collectors 1961-1990 Average, 1990).

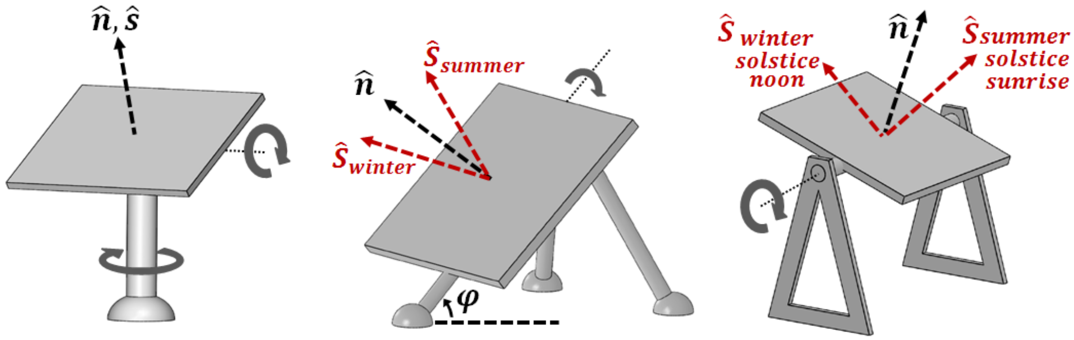


Figure 1.4: Three common tracking schemes: dual axis, polar aligned single axis, and horizontal north-south aligned single axis (Wheelwright B. , Angel, Coughenour, Hammer, Geary, & Stalcup, 2014).

Figure 1.4 illustrates the ability of three different trackers to maintain a module in alignment with the sun. The misalignment of the module vector, n̂, and sun vector, $\hat{s}$, for three different tracking schemes is depicted for the seasonal and diurnal extremes. Dual-axis tracking (left) maintains alignment to the sun all day, year-round. Single-axis tracking about a polar-aligned axis (middle) maintains nearly perfect alignment on the equinoxes, but the incidence angle grows to +/-23.5° on the solstices. Single-axis tracking about a horizontal axis oriented north-south (right) results in a much larger range of incidence angles, depending strongly on latitude. On the equator, polar-axis tracking and horizontal north-south aligned axis tracking are identical. Horizontal N-S tracking gives an incidence angle range bounded by the summer solstice sunrise/sunset,

$$\vartheta_{min} = -sin^{-1}(\sin \varepsilon \sec \varphi), \tag{1.3}$$

and noon on the winter solstice,

$$\vartheta_{max} = |\varphi| + \varepsilon, \tag{1.4}$$

where $\varepsilon = 23.5°$, the declination of Earth (Cooper, Ambrosetti, Pedretti, & Steinfeld, 2013). At Tucson, AZ latitude ($\varphi = 32.2°$) this gives in $\vartheta_{max} = 55.7°$ at noon on the winter solstice. Due to the very large winter solstice noon incidence angle, an aperture tracked on a horizontal N-S axis at $\varphi = 32.2°$ will receive only 56% of direct sunlight compared to the same aperture tracked on two axes. The annually integrated solar resource for each tracking embodiment in Tucson, AZ is shown in Table 1.1. Although losses are severe on the winter solstice, the annually averaged collection efficiency of horizontal N-S tracking is quite good, ~90% of full dual-axis tracking.

Table 1.1: Solar Resource by tracking type in Tucson AZ (NREL, Solar Radiation Data Manual for Flat-Plate and Concentrating Collectors 1961-1990 Average, 1990).

| Tracking Scheme | Average Daily Resource ($kWh/m^2/day$) | % of Dual-Axis Resource |
|---:|:---:|:---:|
| Fixed Horizontal (0°) | 5.7 | 64% |
| Fixed Tilt (Latitude) | 6.5 | 73% |
| Single Axis (Horizontal N-S) | 8.0 | 90% |
| Single Axis (Equatorial) | 8.6 | 97% |
| Dual Axis | 8.9 | 100% |

Remarkably, dual-axis tracking provides only a modest increase in sunlight collection over single-axis tracking arrangements. However, dual-axis tracking allows full 3D concentration, limited by (Winston, Minano, & Benitez, 2005),

$$C_{max,3D} = \frac{n^2}{\sin^2(\theta_a)}\,. \tag{1.5}$$

It is clear that high concentration solar modules resort to dual-axis tracking to increase concentration, not to collect more light. The modest additional insolation is a fringe benefit that is more than nullified by the inevitable loss of diffuse light.

### 1.4 Concentrator Photovoltaics (CPV)

Conventional PV panels, such as Silicon or CdTe, have a single bandgap. Any photon absorbed above the bandgap will generate the same current (a single electron-hole pair) regardless of the photon's energy. Thus, a near–bandgap photon may be converted with very high efficiency (>50%), while higher-energy photons far from the bandgap will be converted at low efficiency, with the remaining energy absorbed in the cell as heat. Sub-bandgap photons do not produce current and are either absorbed as heat or are reflected back out the cell.

Concentrator Photovoltaic (CPV) modules attain high solar conversion efficiency through the use of multi-junction PV cells and concentrating optics. Multi-junction (MJ) cells divide the solar spectrum so that more photons are near-bandgap. By vertically stacking the junctions with highest bandgap on top, the layers effectively split sunlight into discrete spectrums. Figure 1.5, from (Fraunhofer ISE, 2015) depicts the propagation of the solar spectrum through a single-junction and three-junction cell. Note that in a Si cell, most photon energy is lost to thermalization in the visible spectrum (380-780nm) because these photons have energies much higher than the bandgap. Multi-junction cells reduce thermalization losses by converting visible light at nearby bandgaps.

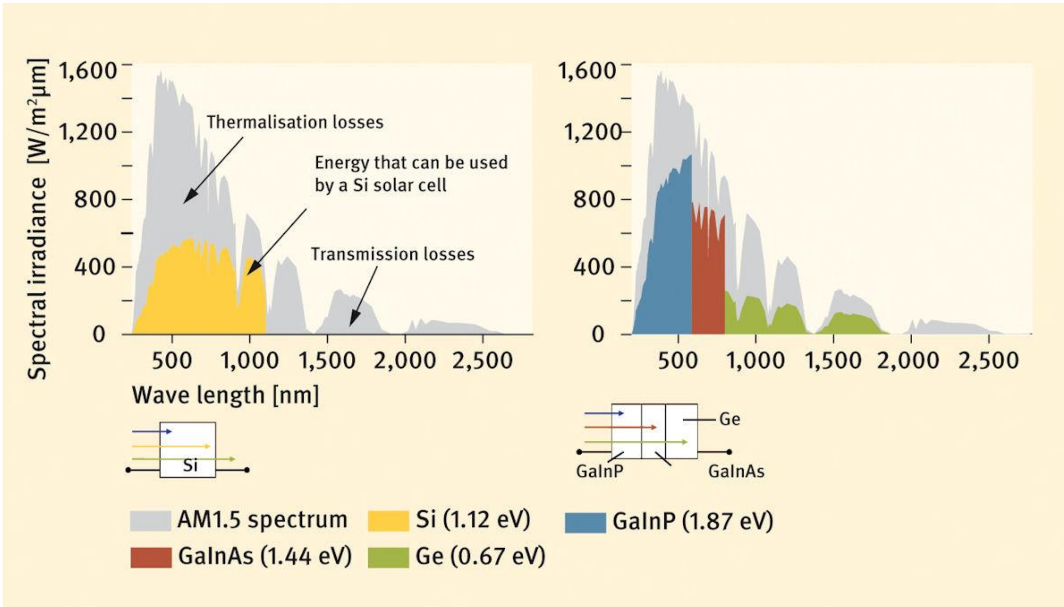


Figure 1.5: Single- vs. Multi-Junction PV cells (Fraunhofer ISE, 2015).

Multi-junction PV cells are currently very expensive per unit area. With dual-axis tracking and large-area optics, high concentration (>1000X) is possible, reducing the $/Watt cost contribution from the cells. The historical progress of research cell record efficiencies in Figures 1.6 and 1.7 suggests that efficiency gains in MJ cells will continue. Figure 1.7 shows the expected increase in CPV cell, module, and system efficiency. System efficiency includes on-Sun losses such as parasitic loads (tracking, cooling, etc.).

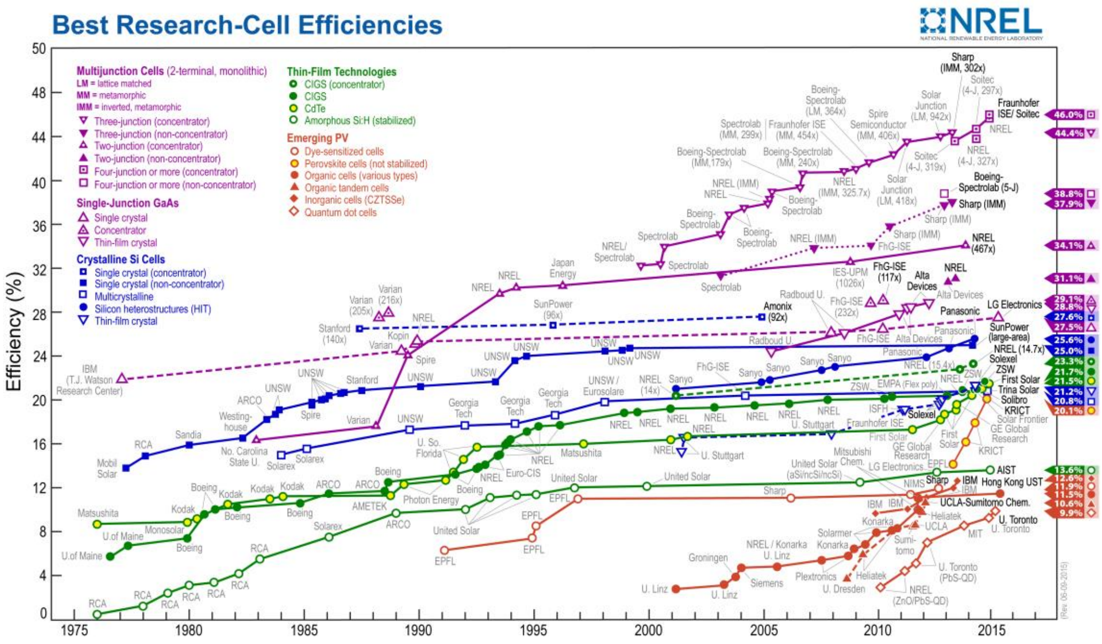


Figure 1.6: Progress in research cell efficiencies by technology (NREL, Best Research Cell Efficiencies, 2015).

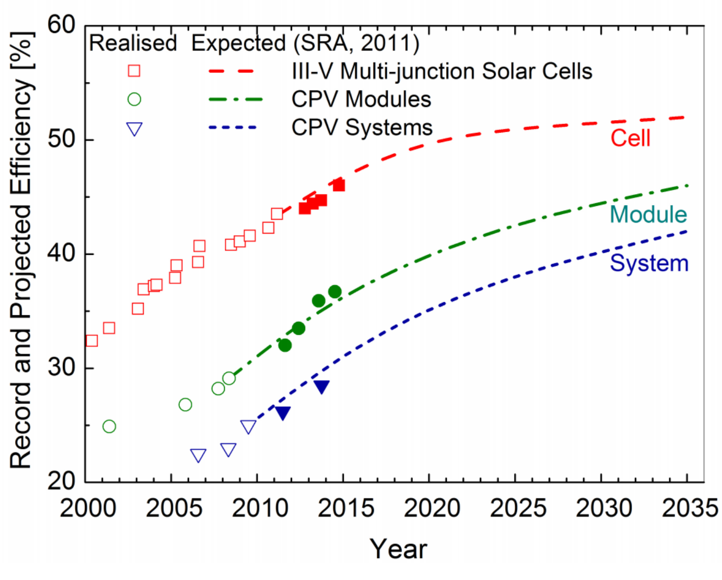


Figure 1.7: Realized and projected CPV cell, module, and system efficiencies (Philipps, Bett, Horowitz, & Kurtz, 2015). System efficiency includes parasitic loads (e.g. tracking).

The CPV industry faces several challenges. First, CPV modules have the added complexity of large-area optics, smaller-area secondary optics, dual-axis tracking, and cell thermal management. Second, concentrating systems do not capture the diffuse solar component. Even in high-DNI locations, this loss is greater than 20%, per Figure 1.3. To 'break-even' against a high-end Silicon module with 21.5% efficiency, a CPV module would have to convert direct sunlight with 27.9% efficiency in Tucson, or 35.8% efficiency in Miami. This assumes that both the Si module and CPV module are on the same dual-axis tracker. Of course traditional PV modules have the added flexibility of requiring no tracking.

However, CPV also has several redeeming features that may allow it to prevail over other technologies in high-DNI markets. First, concentrating optics have the potential for low areal cost. Second, MJ cell efficiencies continue to rise, making CPV module efficiencies more compelling especially in space-constrained sites.


Figure 1.8: Commercial approaches to CPV by (a) Soitec [soitec.com], (b) Semprius [semprius.com], and (c) REhnu [REhnu.com].

As shown in Figure 1.8, there are various optical approaches to CPV including refraction/diffraction (Fresnel lens array, Figure 1.8a), refraction (lens array, Figure 1.8b), and reflection (Figure 1.8c). Each of the optical systems above includes a full-area primary optical element (POE) that receives unconcentrated sunlight, and a sub-area secondary optical element (SOE) that receives concentrated sunlight from the POE.

## 1.5 CONCENTRATED SOLAR POWER (CSP)

Concentrated Solar Power (CSP) systems concentrate direct sunlight onto absorbing thermal receivers. These receivers then convey a heated fluid to a thermal block, where electricity is generated via a Rankine, Brayton, or Stirling-driven generator. Since CSP plants drive mechanical generators, the output is AC and requires no inversion. Due to the availability and high efficiency of very large steam turbines for conventional coal and natural gas fire plants, CSP plants are usually implemented at large scale (>50MW). The most common CSP architectures, depicted in Figure 1.9, are central receiver, trough, linear Fresnel, and dish Sterling. CSP is of particular interest to power utilities due to the potential for thermal storage. By storing excess daytime heat in tanks of molten salt, a CSP plant can continue operation after sunset.

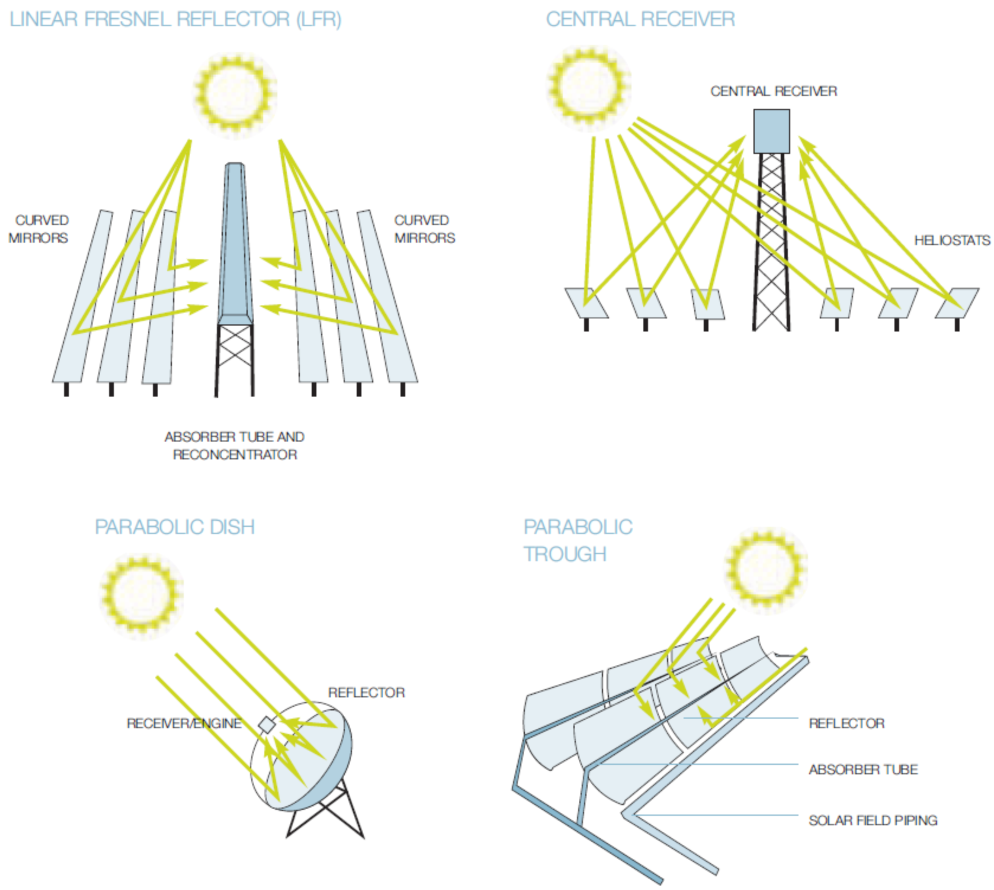


Figure 1.9: CSP architectures (Greenpeace International, 2014).


Figure 1.10: Panoramic view of Solana Generating Station (Gila Bend, AZ).

The 280MW Solana Generating Station in Gila Bend, AZ (Figure 1.10) is an example of state-of-the-art CSP trough technology. The full trough aperture is over 2.2km$^2$, greater than all current worldwide CPV combined. The plant includes six hours of molten salt storage to allow continued operation in high-demand evening hours. The substantial cost incurred by molten salt storage is justified by the increased value of electricity during peak evening hours. Large energy consumers are charged on a 'time of use' price schedule that accounts for varying demand. To the utility, electricity produced during leak loads has more value than during low demand.

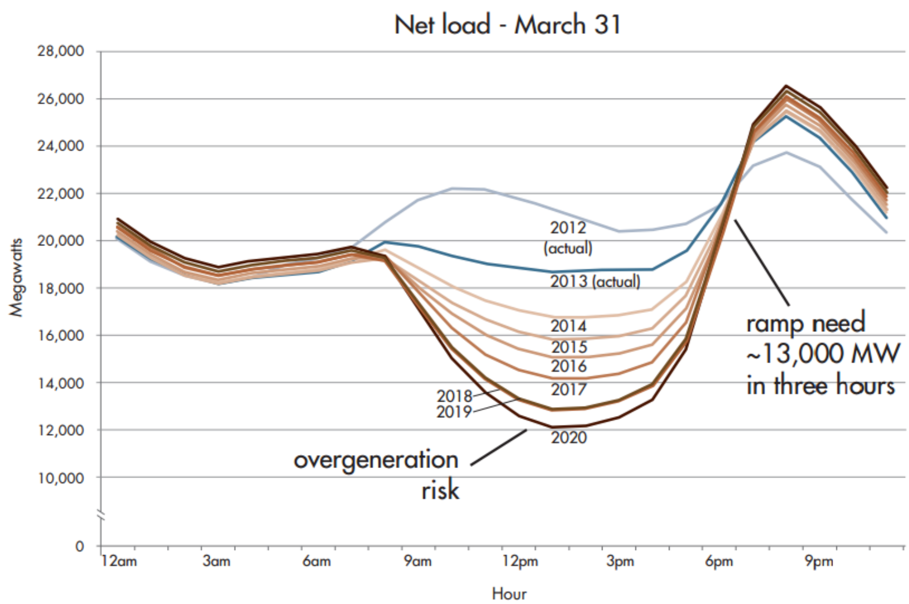


Figure 1.11: "Duck Curve" from California ISO (California ISO, 2013). As daytime PV generation increases, conventional sources must ramp up production more quickly in evening hours.

The famous "Duck Curve" released by California ISO (Figure 1.11) illustrates a grid management challenge inherent with high market penetration of conventional PV. As daytime PV takes on a larger fraction of total generation, the ramp rate required of other sources as the Sun sets becomes steeper. Denholm and Mehos (Denholm & Mehos, 2011) have modeled daily generation dispatch curves in California for increasing PV penetration cases. Summer is a best-case scenario thanks to long days and high demand during daylight hours. Spring loads (Figure 1.12) are not complementary to large daytime generation, leading to high ramp rates and potential overgeneration for PV penetration over 5%.

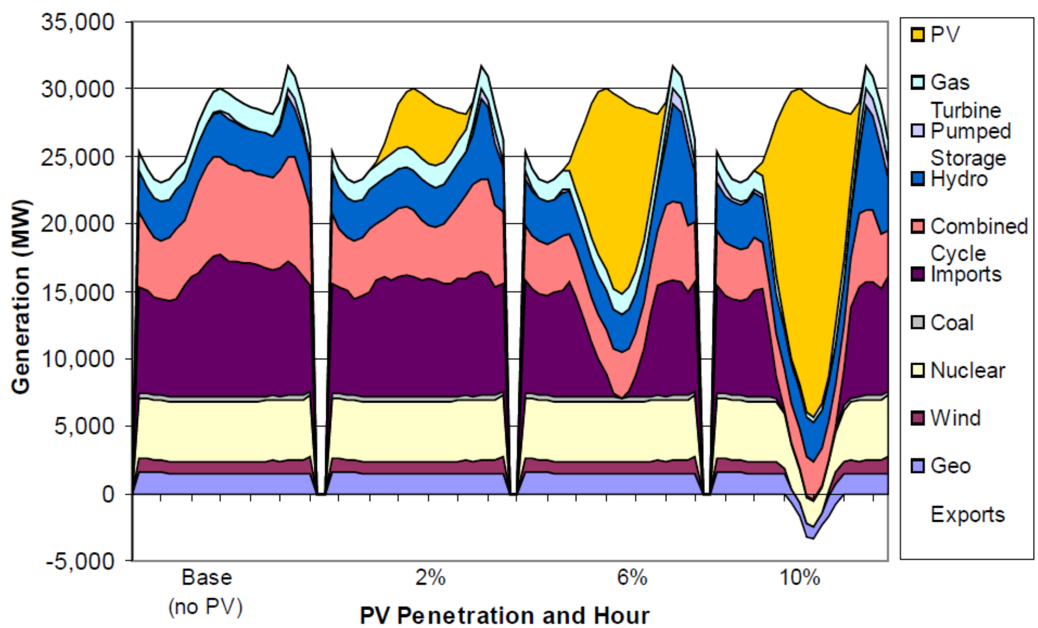


Figure 1.12: Simulated generation on a spring day in California for four PV penetration cases (Denholm & Mehos, 2011).

CSP with storage behaves more like a baseload generator and has the potential to mitigate severe ramp rates, allowing greater PV market penetration (Denholm & Mehos, 2011). Chapter 5 will discuss a hybrid PV/thermal approach that takes advantage of the high efficiency of PV and thermal storage of CSP.

# CHAPTER 2: TROUGH-BASED CPV WITH FREEFORM SECONDARY OPTIC

As discussed in Sections 1.5 and 1.6, CPV and CSP each have individual strengths, but struggle to compete in a market dominated by flat-panel PV. This chapter describes an optical approach that combines the field-proven reliability and low cost of CSP trough mirrors with the high efficiency of MJ cells. CSP trough mirrors, which are 2D concentrators, will be used on *dual-axis trackers*, which are usually reserved for 3D concentrators. By adding novel freeform secondary optics, the final optical system achieves CPV-level concentration. In addition to this work, see (Wheelwright, Angel, & Coughenour, Freeform lens design to schieve 1000X solar concentration with a parabolic trough reflector, 2014) and (Wheelwright B. , Angel, Coughenour, & Hammer, Freeform solar concentrator with a highly asymmetric acceptance cone, 2014).

## 2.1 TROUGHS AS PRIMARY ELEMENTS IN 3D CONCENTRATORS

Parabolic trough mirrors, produced in large volume for CSP plants, are not themselves capable of achieving the high concentration required to economically drive triple-junction PV cells. In typical trough CSP plants, off-axis $2.7m^2$ back-silvered glass segments illuminate vacuum-insulated absorber tubes that convey heated oil to a central thermal power block. Almost all CSP trough systems are tracked about a horizontal north-south oriented axis. As discussed previously, this tracking scheme results in a continuously varying skew incidence, $\vartheta$, which shifts the line focus longitudinally and results in an obliquity factor.

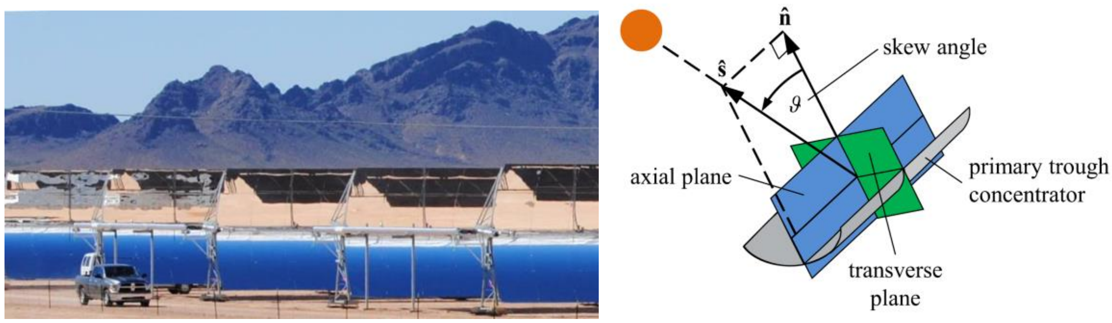


Figure 2.1: Left: View of Solana Generating Station from Interstate 10. Right: trough reference planes from (Cooper, Ambrosetti, Pedretti, & Steinfeld, 2013).

Recall that the skew incidence range on a trough tracked about a horizontal N-S oriented axis is bounded by the summer solstice sunrise/sunset,

$$\vartheta_{min} = -sin^{-1}(\sin\varepsilon \sec\varphi), \tag{2.1}$$

and noon on the winter solstice,

$$\vartheta_{max} = |\varphi| + \varepsilon, \tag{2.2}$$

where $\varepsilon = 23.5°$, the declination of Earth, and $\varphi$ is the site latitude (Cooper, Ambrosetti, Pedretti, & Steinfeld, 2013). At Tucson, AZ latitude ($\varphi = 32.2°$) this results in $\vartheta_{max} = 55.7°$ at noon on the winter solstice. One consequence of skewed illumination of a 2D concentrator is that the apparent source size increases. In this case, the angular width of the sun is dilated, according to (Bendt, 1979),

$$\sin(\theta_{dilated}) = \sin(\theta_{source}) \sec(\vartheta). \tag{2.3}$$

Thus in Tucson AZ on the winter solstice noon, the solar disk ($\theta_{source} = \pm 0.266°$) would subtend $\theta_{dilated} = \pm 0.472°$ when projected onto the plane of 2D concentration (transverse plane). This effect requires trough concentrators to have a larger acceptance angle, which reduces the maximum possible 2D concentration (Equation 1.2).

The acceptance angle of a CSP trough concentrator can be scaled by adjusting the diameter of the thermal receiver, which for full collection must be sized to intercept the skew-dilated solar image convolved with optical and tracking errors. When these errors are combined, typical receivers operate at ~30X concentration, averaged over the circumference of the absorber tube. Three tracking schemes for parabolic troughs are shown in Figure 2.2.

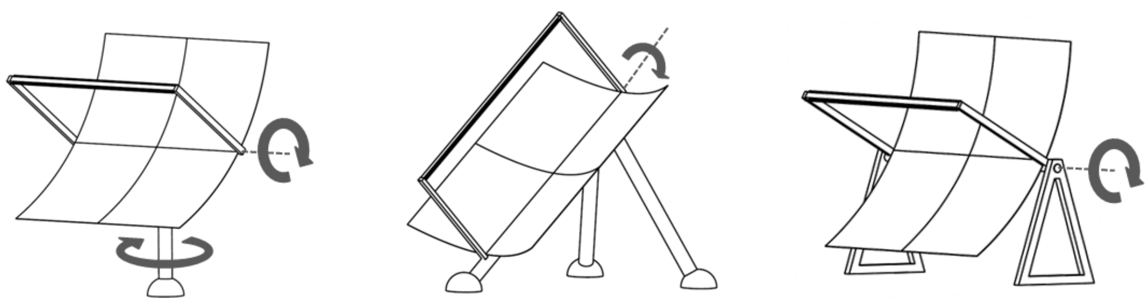

Figure 2.2. Four-segment, F/0.5 parabolic troughs, tracked about two axes (left), a single polar-aligned axis (middle), and a horizontal north-south axis (right).

The maximum skew angle, $\vartheta$, is greatly reduced with equatorial tracking ($-23.5° < \vartheta < 23.5°$). One prior CPV design takes advantage of the limited skew incidence range from polar-axis tracking by introducing CPC reflectors along the line focus (Brunotte, Goetzberger, & Blieske, 1996). This CPC array, with acceptance angles just above 23.5º in the axial plane, divides the medium-concentration line focus into a series of 300X foci.

In other prior work, moving secondary optics have been proposed near the line focus of parabolic troughs tracking about horizontal or polar axis (Di Vinadio & Palazzetti, 2011) (Cooper, Ambrosetti, Pedretti, & Steinfeld, 2013). CPV level concentration (>500X) requires two degrees of tracking freedom which these systems achieve by complementing single-axis trough tracking with laterally translated cylindrical lenses (Figure 2.3a) or actively tilted CPC elements (Figure 2.3b).

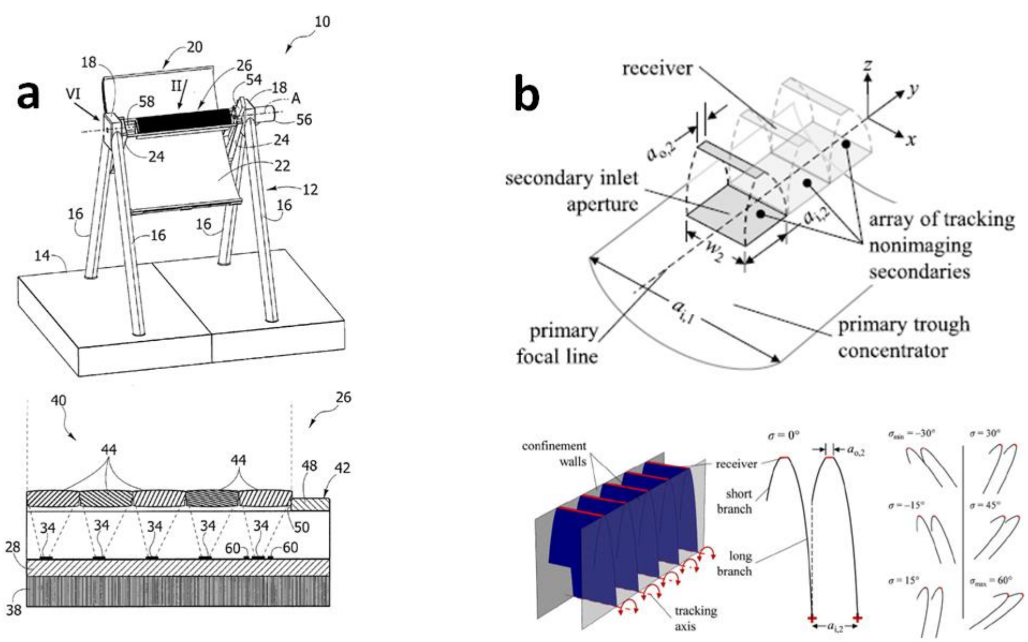


Figure 2.3. Prior art: (a) cylindrical lenses along the linear focus (Di Vinadio & Palazzetti, 2011); (b) rotating asymmetric CPCs along the linear focus (Cooper, Ambrosetti, Pedretti, & Steinfeld, 2013).

The work described in this chapter takes a different approach to trough mirrors. Let us consider using trough mirrors as the primary collectors in CPV modules on *dual-axis* trackers. The natural course would be to use *dish* mirrors with dual-axis trackers to provide ready-to-use high concentration. However, dish mirrors do not yet enjoy the established supply chain of trough mirrors, which are already produced in huge volume commercially for ~\$35/m$^2$. If they can be adapted for high concentration, CSP trough optics could act as a low-cost, high reliability primary optical element.

## 2.2 Two-Stage Orthogonal Concentration: Secondary Optics Design

Trough mirrors only concentrate sunlight in the transverse plane, leaving incident sunlight unconcentrated in the axial plane (see Figure 2.4). By introducing an array of secondary optics near the linear focus, a second stage of concentration is allowed in the axial plane, forming multiple regions of higher concentration. The trough illuminates the secondary optics in the transverse plane over a constant angular range, set by the rim angle.

The system described here is tailored for dual-axis tracking, a condition that nearly eliminates skewed incidence. High concentration is achieved through two successive, orthogonal steps (Figure 2.5, right). First, the trough produces a medium-concentration line focus, coincident with the axial plane of the trough. An array of secondary lenses intercepts this cylindrically converging sunlight below the line focus. These lenses have the two-dimensional cross section of a plano-convex lens, extended into a toroid by rotation about an axis parallel to the line focus. The conventional cylindrical and spherical lenses of previous designs (Di Vinadio & Palazzetti, 2011) limited the maximum rim angle. However, since the toroidal lens array wraps around the line focus, ray bundles from different rim angles see approximately the same optical power along the arc of the toroid. This avoids the severe Petzval curvature inherent in cylindrical or spherical lenses.

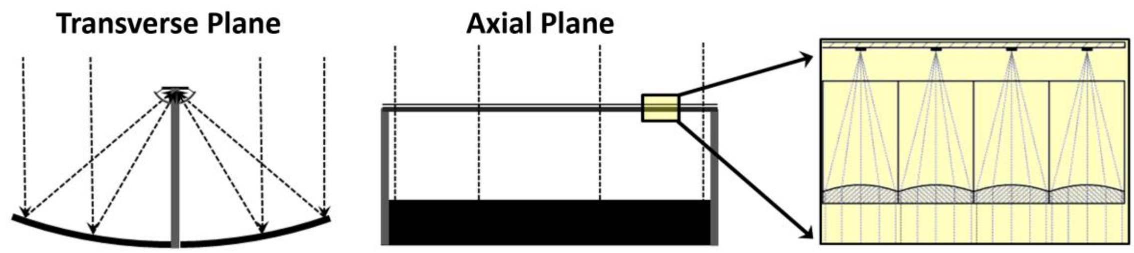


Figure 2.4. Trough cross-section in the transverse plane (left) and axial plane (middle) detail of secondary optics cross-section (right).

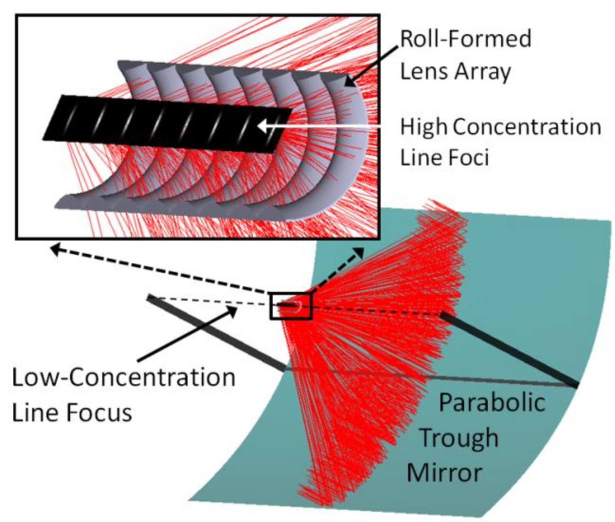


Figure 2.5. Left: An inner-segment parabolic trough mirror on a dual-axis tracking at The University of Arizona. Right: A parabolic trough and freeform secondary lens array.

Figure 2.5, left, shows an F/0.5 parabolic trough on a dual-axis tracker at The University of Arizona Bear Down Solar Test Facility.  These are inner segments from industry-standard solar thermal troughs (1.7m focal length).  CSP troughs are usually four segments wide, with an inner and outer off-axis parabola on either side of the thermal tube.  The two-stage concentration approach is shown with split scale in Figure 2.5, right.  Figure 2.6 is a detail view of a trough line focus without any secondary optics (left) and with a toroidal lens array (right).

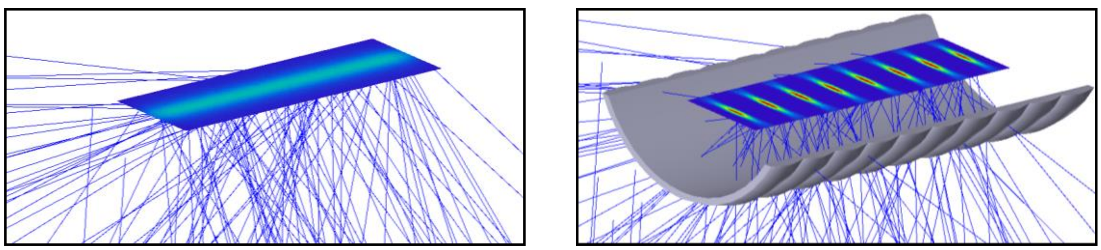

Figure 2.6:  Line focus with and without interception by toroidal arc lens array.

This system requires a dense linear array of MJ cells, arranged in highly elongated strips.  Cells from each strip are not uniformly illuminated, and are thus wired in parallel.  This concentrator cannot be considered nonimaging, since the two orthogonal stages form a highly elongated, and aberrated, solar image. This two-stage concentrator is thus highly anamorphic, with an aspect ratio of ~25:1, the ratio of the trough and toroidal lens focal lengths.

In the design case chosen here, an F/0.5 mirror with 1.7 m focal length is paired with a toroidal arc lens with 25.4 mm lenticulations.  The cell strips are 2.5 mm wide and 34.5 mm or 43.2 mm long, for 1000X and 800X geometric concentration embodiments, respectively. Each cell strip is composed of many smaller cells, arranged in a row and wired in parallel.

Since the cell plane of Figure 2.6, right, is illuminated by a series of elongated solar images, the system is sensitive to off-axis pointing. Any tracking or optical errors displace and aberrate the solar image. Tracking errors may be decomposed into two dimensions: errors in the transverse and axial planes (Figure 2.7).

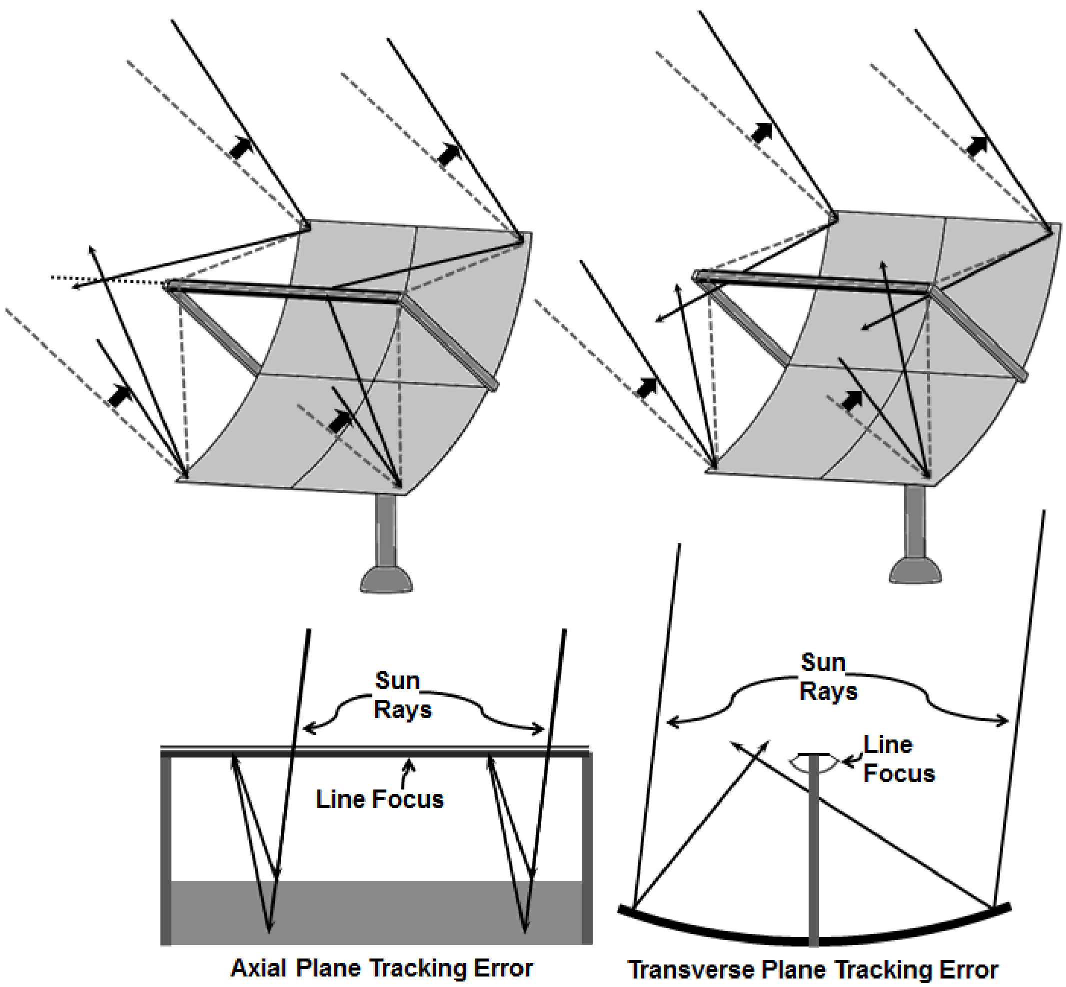


Figure 2.7: Effect of tracking errors in the axial and transverse planes.

In the axial plane, tracking errors result in a longitudinal shift in the trough line focus. Toroidal arc elements intercepting this shifted focus thus produce laterally shifted solar foci, as shown in Figure 2.8.

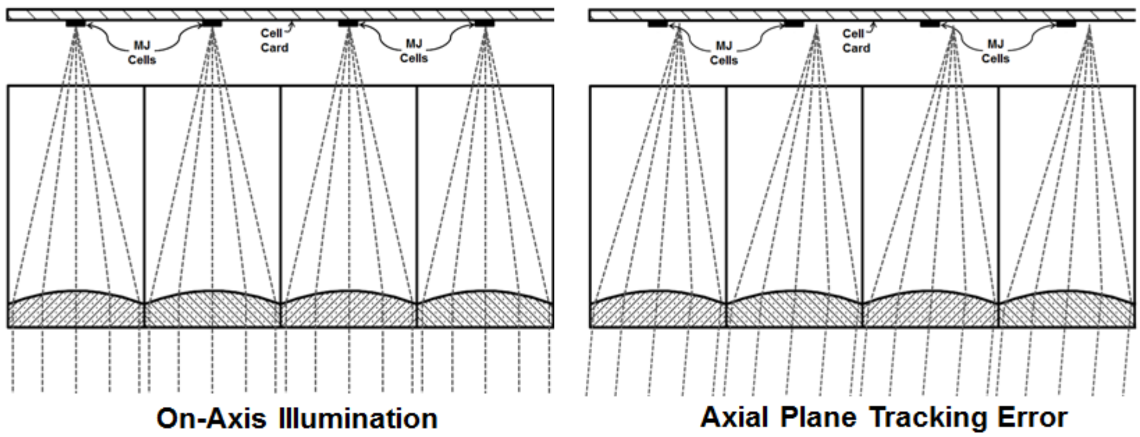


Figure 2.8: Displacement of line foci caused by tracking error in the axial plane.

In this dimension, Köhler stabilization is readily achieved with a series of rod lenses (Figure 2.9). Tapered glass funnels bonded to directly to the cells could also be used to catch off-axis light, but rod lenses have manufacturability advantages. They can be drawn without grinding/polishing and are not directly attached to the cells, so thermal mismatch is not an issue. The elongated solar images produced by the trough and toroidal lens array are centered within the rod lenses, which stabilize a rectangular illumination pattern on the cell strips. This 2D, line-focus Köhler illumination scheme is related to the 3D schemes that have been implemented in point-focus systems (Coughenour, Stalcup, Wheelwright, Geary, Hammer, & Angel, 2014). In 2D, the rod lenses image the edges of the toroidal arc lenticulations to the long cell strip edges. As the illumination angle in the axial plane varies due to tracker error, the solar focus formed by each toroidal lens lenticulation shifts laterally within the diameter of the rod lens, which stabilizes a solar *non-image* on the cell strip.

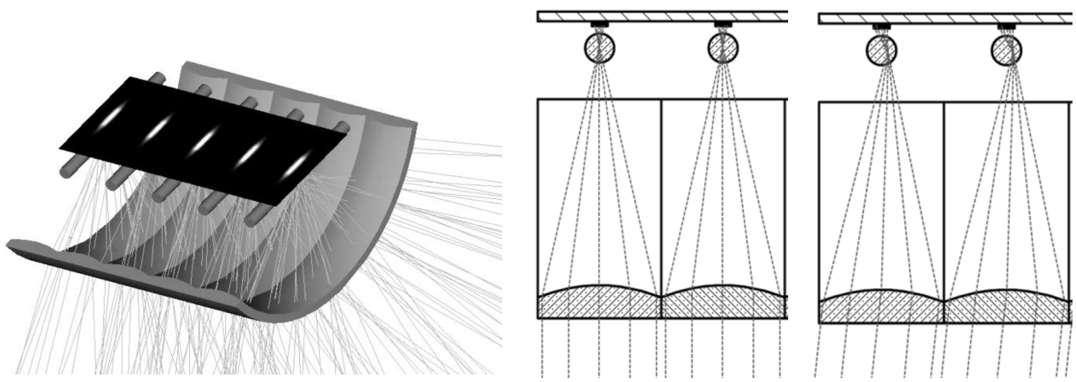

Figure 2.9: Left: Rays from an F/0.5 trough propagating through a toroidal lens array with rod lens tertiaries. Right: Cross-sectional views of a toroidal lens array with rod lens tertiaries for on-axis and off-axis illumination.

With the rod lenses included, the azimuthal acceptance angle increases dramatically, giving the highly asymmetric performance shown in Figure 2.10. This figure plots one quadrant of the acceptance angle space, with the >90% optical efficiency region shaded green. This optical efficiency already includes 2 mrad RMS slope error from the trough mirror, but not the solar radius. This representation allows direct comparison to the solar disk, overlayed in yellow. Rod lens Köhler stabilization only operates in the azimuthal (axial plane) direction, causing a highly asymmetric acceptance angle. Thus, at 1000X average geometric concentration, this system barely accommodates the sun in the elevation direction.

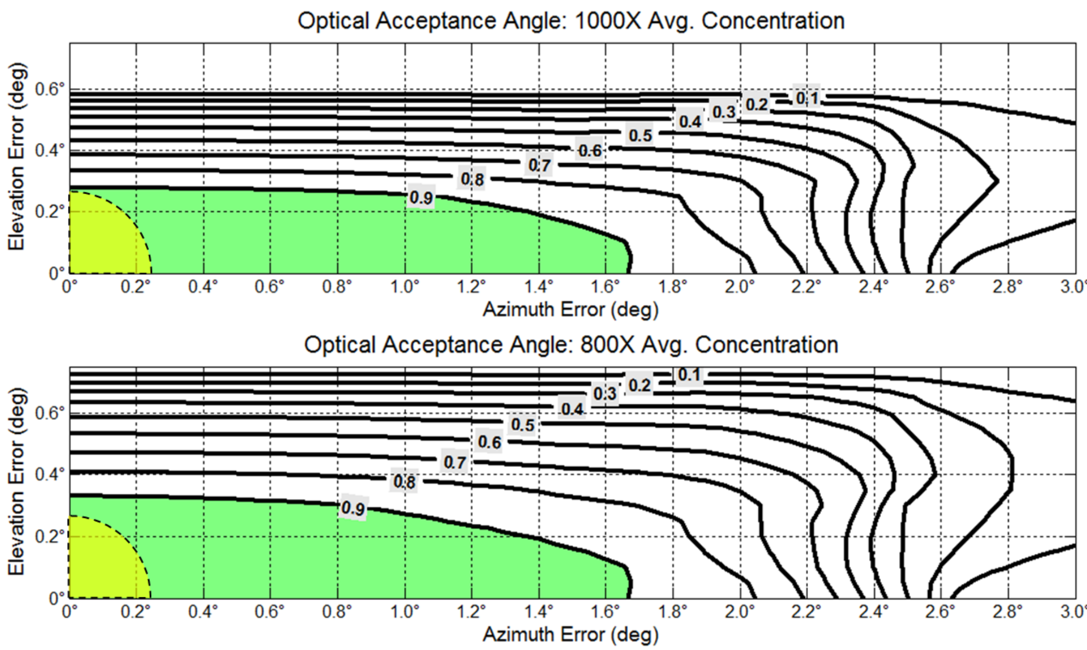


Figure 2.10. One quadrant of the acceptance angle space is plotted for cell strips sized for 1000X and 800X average geometric concentration (Wheelwright B. , Angel, Coughenour, & Hammer, Freeform solar concentrator with a highly asymmetric acceptance cone, 2014).

The optical acceptance angle data shown in Figure 2.10 was generated with ZPL macro-driven, non-sequential raytracing in ZEMAX. When the cell strips are sized for 1000X average geometric concentration, the acceptance angle in the azimuth direction is ±1.49°, sufficient to allow for the solar disk, optical errors, and tracking errors. In the elevation direction, which does not benefit from Köhler illumination, the acceptance angle is only ±0.29°, barely enough to accommodate the solar disk. A reduction in geometric concentration is needed to allow additional tolerance in elevation. Reduction to 800X average geometric concentration (a longer cell strip) increases the elevation acceptance to ±0.33°.

In the transverse plane, where this concentrator does not benefit from nonimaging Köhler illumination, tracking errors translate the high concentration foci longitudinally along the length of the cell strips, as shown in Figure 2.11. This rapid translation explains the poor acceptance angle in the axial plane (or elevation tracking direction).

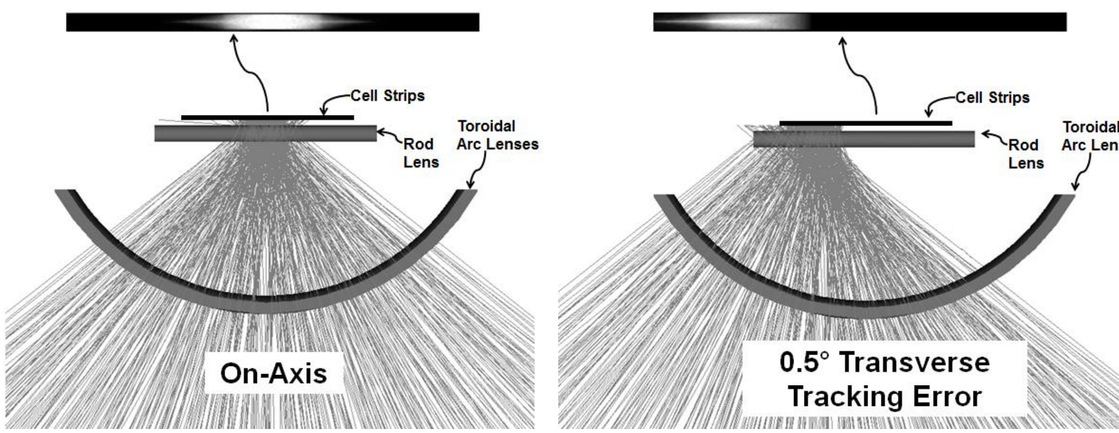


Figure 2.11. Tracking errors in the transverse plane.

## 2.3 Toroidal Arc Lens Array Fabrication

Although toroidal lens arrays are promising candidates for a trough CPV system, they are not readily produced with conventional grinding/polishing. A prototype roll-forming machine was built to prove a path to high volume production. Two rollers, one flat and another containing grooves which have the inverse profile of the desired lens array, are rotated while a heated glass or plastic plate is passed between them. As the plate passes between the rollers, it deforms to take the shape of the grooves. The secondary curvature is accomplished by rotating the rollers with a differential radial velocity, which induces a shear in the material. Apart from the differential shear, the process is very similar to that used to produce fluted glass windows. For the first prototypes, B270 glass lenses were produced by slump molding over the ribbed cylinder. Subsequent cylindrical grinding/polishing gave the outer smooth finish. The surface quality of the roll-formed and slumped lenses has been limited by the grain size of the boron nitride and graphite mold release (see Appendix B). Subsequent polishing removes residual haze. However, this step should be avoided in a cost-conscious system. The lenticulations are inward-facing so that the environmentally exposed outer surface is easier to clean and less lively to collect dust.

Figure 2.12. Left: custom roll-forming machine built by The University of Arizona to form toroidal arc lens arrays. Right: Slump-molded B270 toroidal lens array, with inward-facing 1” lenticulations.

The surfaces resulting from the slump and roll-formed process above are not imaging quality. However, they are sufficient for non-imaging concentrators due to the tolerance provided by the Köhler optics. The inset photo in Figure 2.13 is a long exposure of a B270 toroidal arc lens array illuminated by two laser fans separated by 90° while white paper is translated through focus. The two ray fans simulate illumination from the trough rim. The additional concentration provided in the axial plane by the toroidal lens is apparent.

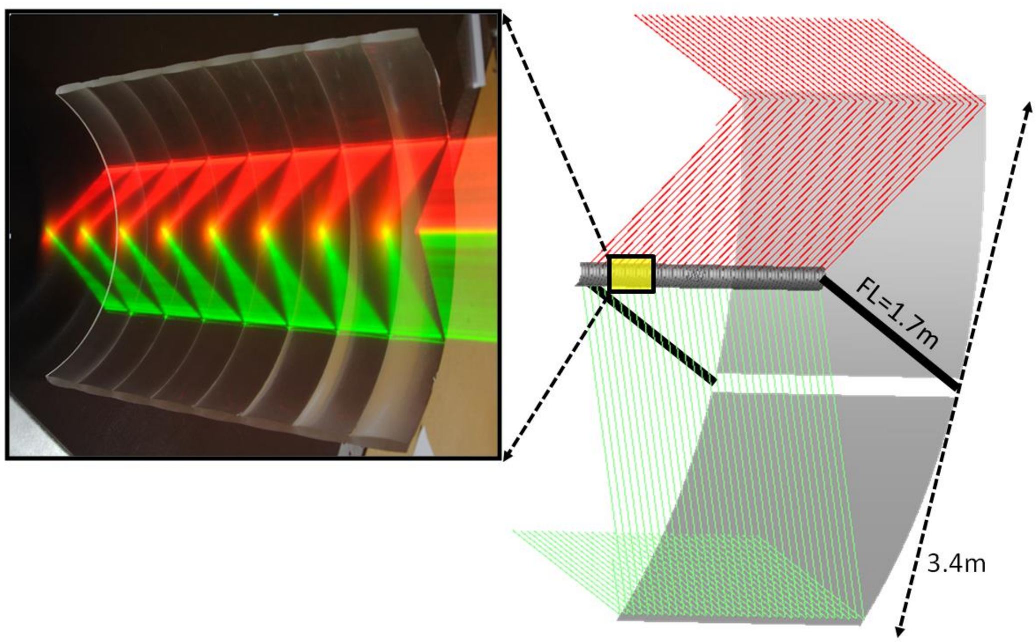


Figure 2.13. Illustration of an F/0.5 parabolic trough and long-exposure photograph of a B270 toroidal arc lens array illuminated by two laser fans, red and green, separated by 90° to simulate illumination from opposite sides of the trough

## 2.4 Limitations of Current Parabolic Troughs

The ray tracing analysis of Section 2.2 accounts for 2 mrad RMS slope error, a target readily achieved in commercial troughs. However, this error was modeled with a Gaussian spread centered on the specular beam. In reality, fabrication artifacts in commercial trough mirrors lead to highly anisotropic optical errors. Figure 2.14 shows the slope errors of an inner-segment trough mirror as measured by the manufacturer RioGlass with a contracted metrology system (QDEC) and independently measured by The University of Arizona with a metrology system developed by the author (Wheelwright B. , Angel, Weiser, Stalcup, & Coughenour, 2013) (see also Appendix C).

Note that the X-slope errors (the focusing direction) are significantly lower than errors in the non-focusing (Y) direction. This trough segment, of representative commercial quality, has 1.6 mrad RMS slope error in the focusing direction and 3.05 mrad RMS slope error in the non-focusing direction. In CSP plants, good optical performance is essential in the focusing X direction. In the non-focusing Y direction, optical errors merely impact the longitudinal distribution of light along the tubular receiver. Since the absorbing pipes are largely agnostic to the irradiance distribution, significant errors in the non-focusing Y direction are tolerated.

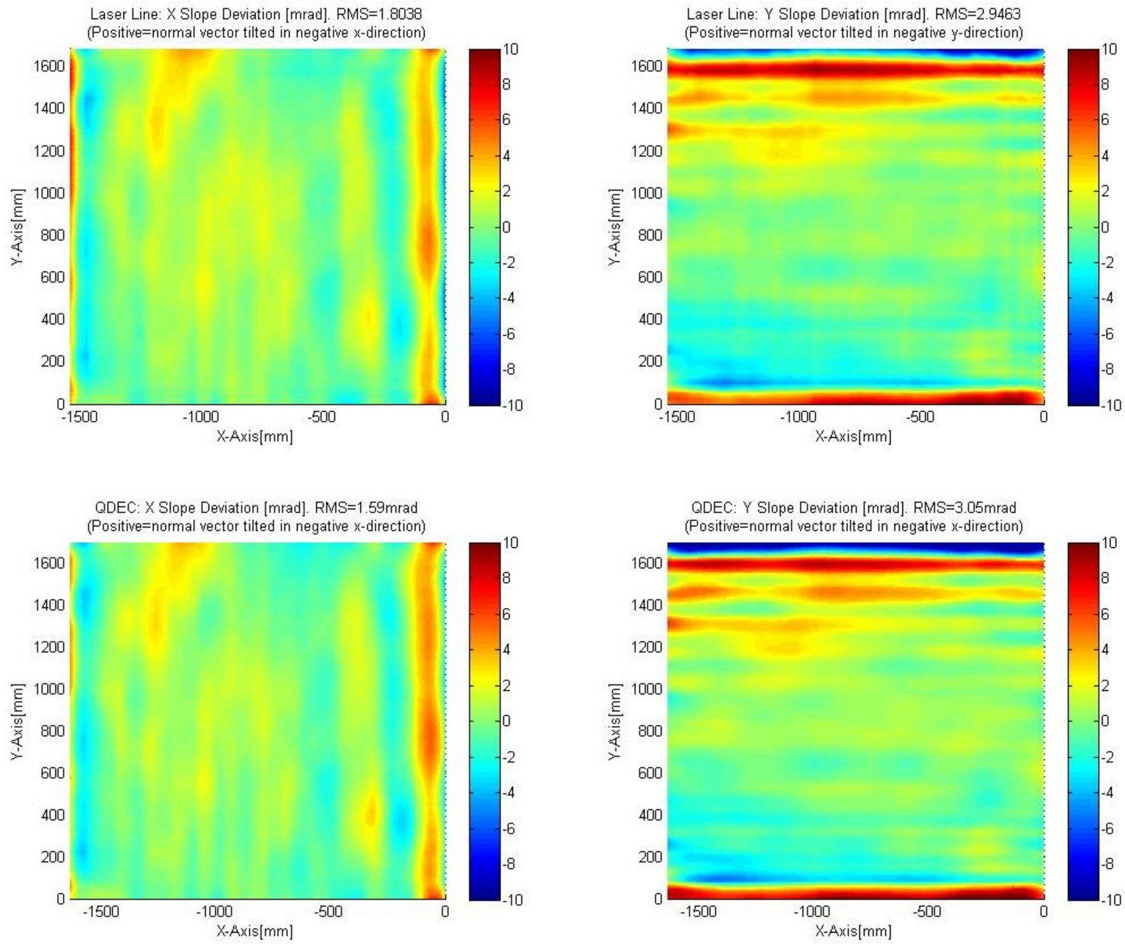


Figure 2.14. Errors in X-slope (left) and Y-slope (right) for a typical inner-segment trough mirror produced by RioGlass. Top measurement set is by The University of Arizona (see Appendix C) and bottom set is by RioGlass with a contracted metrology system (QDEC).

Although the anisotropic slope errors shown in Figure 2.14 are acceptable for solar thermal applications, they will prove problematic in photovoltaic systems. Figures 2.15 and 2.16 show raytracing simulations from an F/0.5 trough using the measured errors shown in Figure 2.14. Figure 2.15 is the line-spread function produced by the trough from an infinite, zero-étendue source. Even after convolving these errors with the solar disk (Figure 2.16), bright caustics are still prominent. These caustics are a consequence of the periodic ripple artifacts in the non-focusing direction.

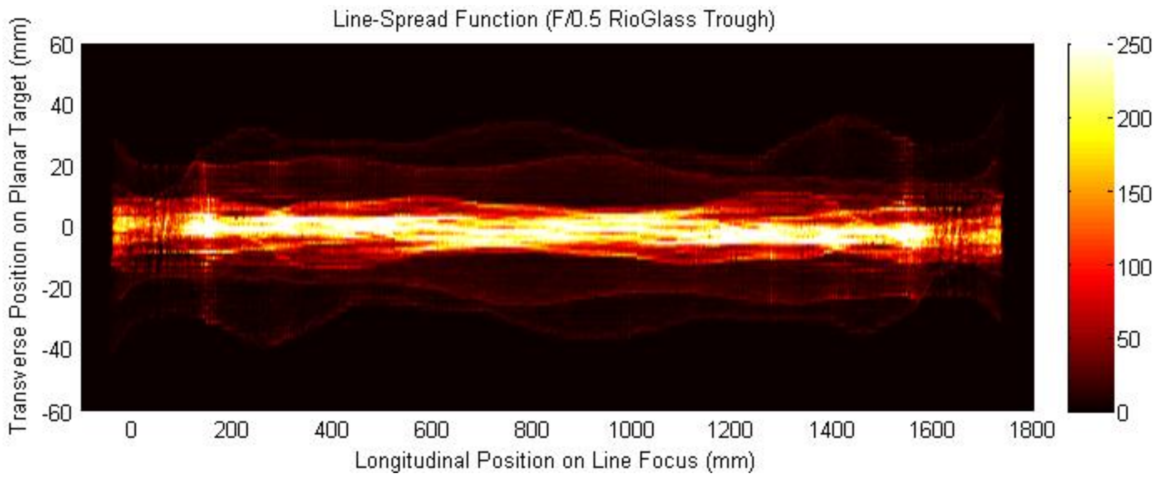


Figure 2.15: Line spread function from a simulated F/0.5 trough composed of RioGlass segments.

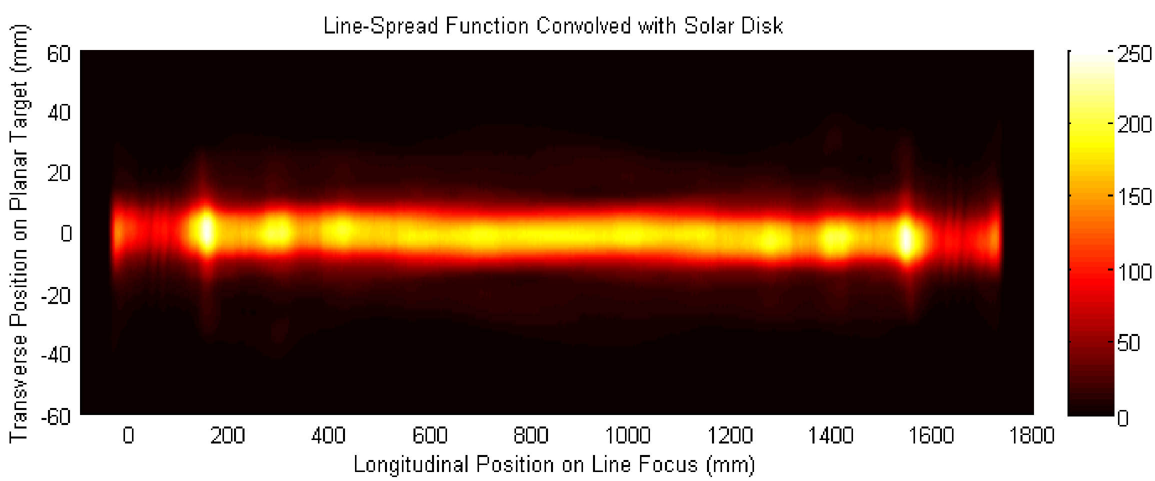


Figure 2.16: Line focus (including solar disk) from a simulated F/0.5 trough composed of RioGlass segments. Units are geometric concentration (see discussion below).

The color scale of Figure 2.16 shows simulated geometric concentration on a flat target. Note that trough receiver tubes are 70mm diameter, so the average geometric concentration over the circumference of the tube is much lower. For example, a six meter wide trough of 1.7 m focal length would illuminate the tube with an average $6000/(2\pi*35)=27X$ concentration.

The simulations above are for zero-skew illumination, which turns out to be the worst case for the caustics. In high skew illumination, the fan of rays reaching one point on the line focus cut across multiple ripple artifacts on the trough aperture. This tends to average out the caustic behavior. However, the optical design of Section 2.2 maintains nearly zero skew with dual-axis tracking.

The toroidal arc lens array intercepts the trough line focus, effectively binning the solar flux into separate linear cell groups. Ideally, each cell group would receive equal illumination and produce the same current. This would allow efficient series-connection of the cell groups. Any current mismatch between series-connected cell groups constitutes a direct loss to the system. Either the weakly illuminated cell group will current-limit the whole series chain, or bypass diodes are required to completely cut out the limiting group.

Using the simulated line focus of Figure 2.16, we can divide the irradiance into longitudinal bins to determine the irradiance variation between cell groups. Using 25.4 mm bins, corresponding to the toroidal arc lenticulations previously shown, the flux variation between cell groups is plotted in Figure 2.17. Flux variation is low near the center of the line focus because the most of the ripple artifacts are near the edges. However, even after cropping the line focus 200mm from each end to remove the most severe artifacts, the hot caustic regions still result in >25% flux variation between bins.

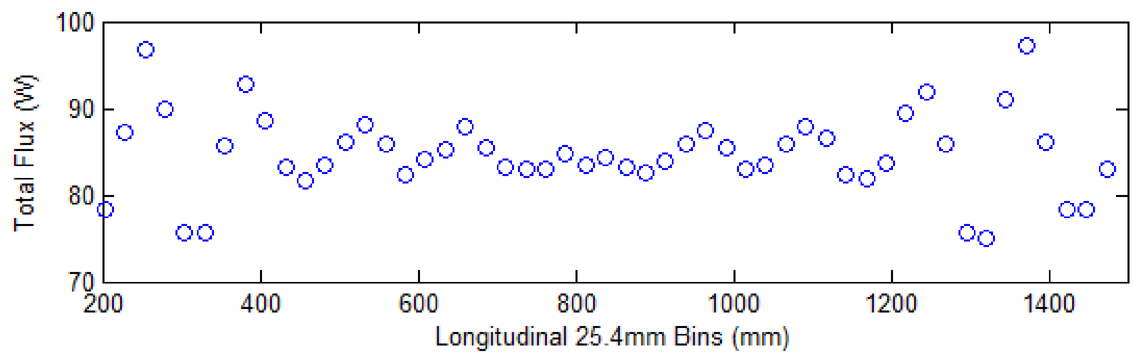


Figure 2.17: Linear focus of a commercial-quality trough, binned into 1” groups.

The irradiance mismatch shown in Figure 2.17 may be mitigated in various ways: (1) improve trough mirror slope accuracy in the non-focusing direction, (2) widen the lenticulations of the toroidal arc lens array, or (3) wire adjacent cell groups in parallel. The latter two strategies both have the effect of increasing the effective bin size. Unfortunately, the current and resistive losses would increase concomitantly.

The 25.4 mm lenticulations modeled previously are already pushing the boundary of acceptable current. On average, the cell group under each lenticulation receives power $P_{lent}$ according to:

$$P_{lent} = W_{lent} W_{trough} \eta_{opt} E_{DNI} \tag{2.4}$$

where $W_{lent}$ is the lenticulation width, $W_{trough}$ is the aperture with of the trough, $\eta_{opt}$ is the total system optical efficiency, and $E_{DNI}$ is the direct normal insolation. Let $W_{lent} =$

$25.4mm$, $W_{trough} = 3.4m$, $\eta_{opt} = 85\%$, and $E_{DNI} = 1000\frac{W}{m^2}$. Then $P_{lent} = 73W$. To first order, we can approximate the total current produced by this cell group, $I_{group}$, with

$$I_{group} = [P_{lent}\eta_{cell}]/V_{cell} \tag{2.5}$$

where $\eta_{cell}$ is the MJ cell efficiency and $V_{cell}$ is cell voltage at the maximum power point. Using data from Spectrolab's C4MJ (Spectrolab, 2011), let $\eta_{cell} = 40\%$ and $V_{cell} = 2.76V$. This gives $I_{group} = 10.6A$, which is already high. Any further parallelization would lead to prohibitively large busbars and leads. We are thus left to consider mitigation strategy (1), improving trough mirror accuracy in the non-focusing direction.

The major ripple artifacts in commercial troughs today result from a rolling process and subsequent tempering. The University of Arizona and REhnu Inc, supported by a SunShot CSP grant ("Advanced Manufacture of Collectors" #DE-EE0005796) has developed a slump-molding process which achieves <1.0mrad slope errors in the focusing *and* non-focusing direction. If implemented at scale to reduce costs, such troughs would be well-suited to drive CPV modules along the line focus.

The team built a prototype rapid-slump furnace (Figure 2.18). The furnace rapidly heats flat glass, which softens and slumps over a stainless steel mold of arbitrary shape. The process has been proven for both 2D troughs and 3D dishes (Angel, Stalcup, Wheelwright, Warner, Hammer, & Frenkel, 2014).

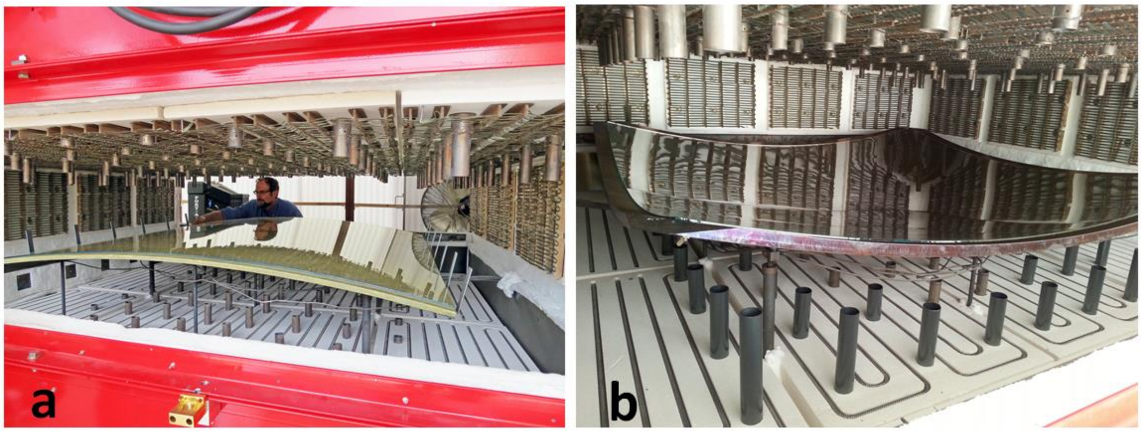


Figure 2.18: Rapid-slump prototype furnace at The University of Arizona Steward Observatory Mirror Lab with a trough mold (a) and a dish mold (b).

The rapid slump furnace has been tested with a trough mold (Figure 2.18a) and a concave dish mold (Figure 2.18b). Due to a procedural error during the machining of the trough mold, glass replicas produced using this mold had figure errors >1 mrad. However, the repeatability and replication accuracy of the slump-molding process were <1.0 mrad RMS. The second mold tested with the furnace was a correctly machined 1.5 m focal length concave dish. Glass replicas produced with this mold had excellent (<0.7 mrad RMS) slope errors in both dimensions (Figure 2.19). We expect that with a correctly machined mold, trough mirrors would achieve equivalent accuracy.

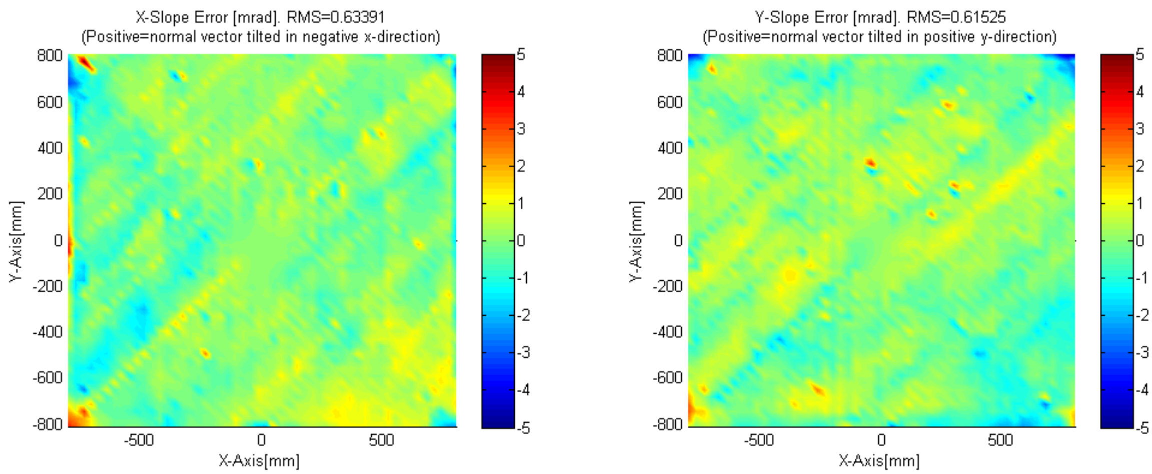


Figure 2.19: X and Y-slope errors for a slumped 1.6 m square dish (1.5 m focal length).

Using the slope error map of Figure 2.19, a line-spread (Figure 2.20) was produced *as if the mirror were a trough*, rather than a dish. Convolving with the solar disk (Figure 2.21), and dividing the flux into 25.4 mm bins (Figure 2.22) reveals an expected current variation of only 6%. This is a marked improvement over commercial-quality troughs, which would give at least 25% flux variation.

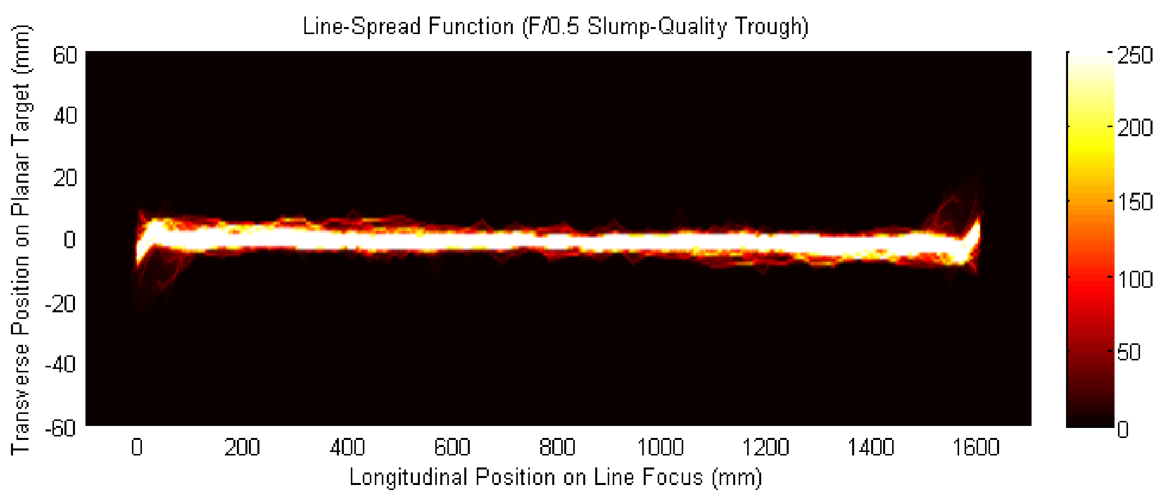


Figure 2.20: Line spread of an F/0.5 slump-quality trough.

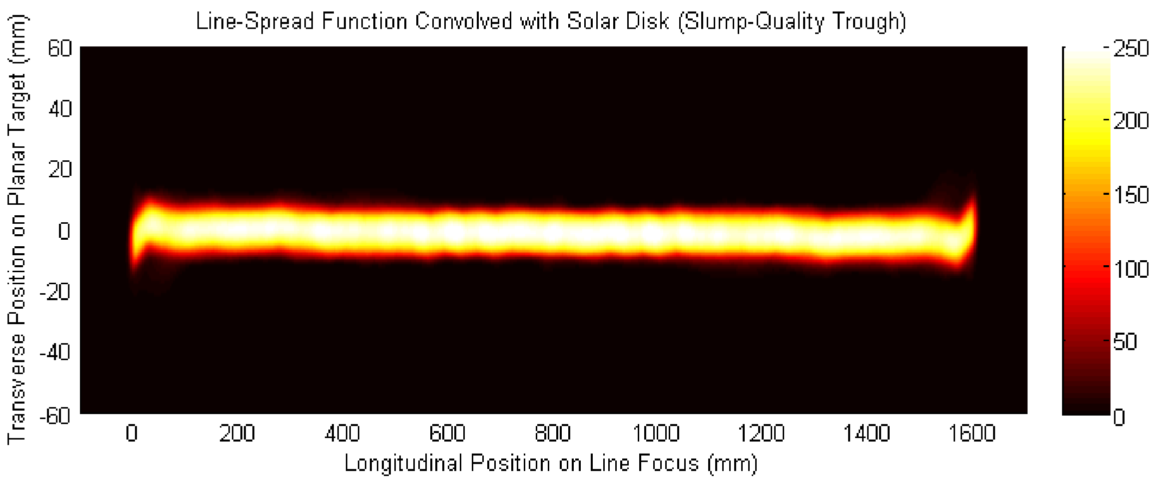


Figure 2.21: Line spread of an F/0.5 slump-quality trough convolved with the solar disk. Units are geometric concentration.

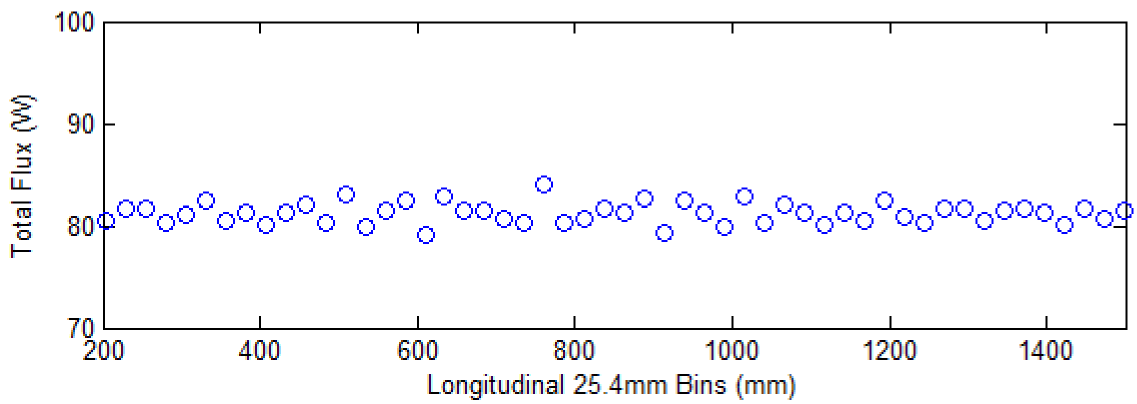


Figure 2.22: Linear focus of a slump-quality trough binned into 25.4mm groups.

In conclusion, the concentration approach of Section 2.2 holds promise for CPV as long as trough mirrors can improve in slope quality by at least a factor of three in the non-focusing direction. This improvement has been demonstrated at prototyping volume with a slump-molding process in a radiative furnace.

## 2.5 Toroidal Arc Lens with Tracking Integration

Two degrees of tracking freedom are required to reach high concentration. The optical system of Section 2.2 assumes conventional altitude/azimuth tracking. However, tracking may be decomposed into motions other than the conventional altitude-azimuth axes. Tracking-integration maintains the étendue-prescribed dual degrees of freedom needed to achieve high concentration, while shifting the mechanical burden from bulk module tracking to small-motion linear actuation, rotation, or passively induced material changes. Novel tracking-integrated schemes may lead to lower-cost CPV/CSP optical systems. Various passive and active tracking-integration approaches are reviewed by (Wheelwright, Angel, & Coughenour, Tracking-integrated optics: applications in solar concentration, 2014).

The solar resource available to a tracking-integrated optical system depends on the primary, external mode of tracking. The range of incidence angles on the external aperture likewise depends on the tracking mode. Figure 2.23 plots the total solar resource for two single-axis tracking modes and the distribution of this resource over the full incidence angle range. See (Wheelwright B. , Angel, Coughenour, Hammer, Geary, & Stalcup, 2014) for a full discussion of the computational methods and validation of this distribution. This plot is unique to 32.2° latitude and Figure 2.23 is a single frame from a full video showing the latitude dependence (https://youtu.be/PN1pf5c5rvk).

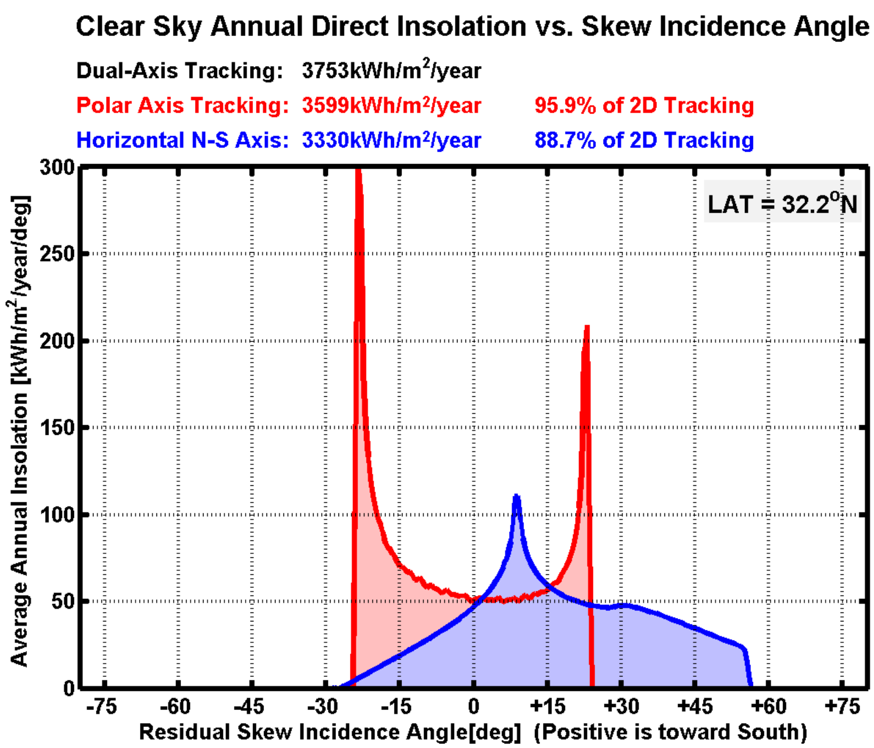


Figure 2.23: Integrated annual flux as a function of skew incidence on an aperture tracked at 32.2° N latitude about polar-aligned (red) and horizontal north-south aligned (blue) axes. See (https://youtu.be/PN1pf5c5rvk) for latitude dependence.

The two external single-axis tracking modes shown in Figure 2.23 give very different incidence angle ranges, summarized in Table 2.1.

Table 2.1: Tracking-integration motion to complement external module tracking.

| Primary (External Tracking) | Incidence Angle Range (for ϕ=32.2°) | Tracking-Integrated Motion |
|---|---|---|
| Dual-axis | ϑ=0° (nominal) | None |
| Single-axis (Polar-aligned) | -23.5°<ϑ<23.5° | Linear translation between cells and toroidal lens |
| Single-axis (Horizontal north-south aligned) | -28.1°<ϑ<55.7° | Curved motion between cells and toroidal lens |

By limiting the incidence angle to only -23.5°<ϑ<23.5°, polar axis tracking can be complemented with very simple, linear relative motion between the toroidal lens lenticulations and the cells (Figure 2.24).

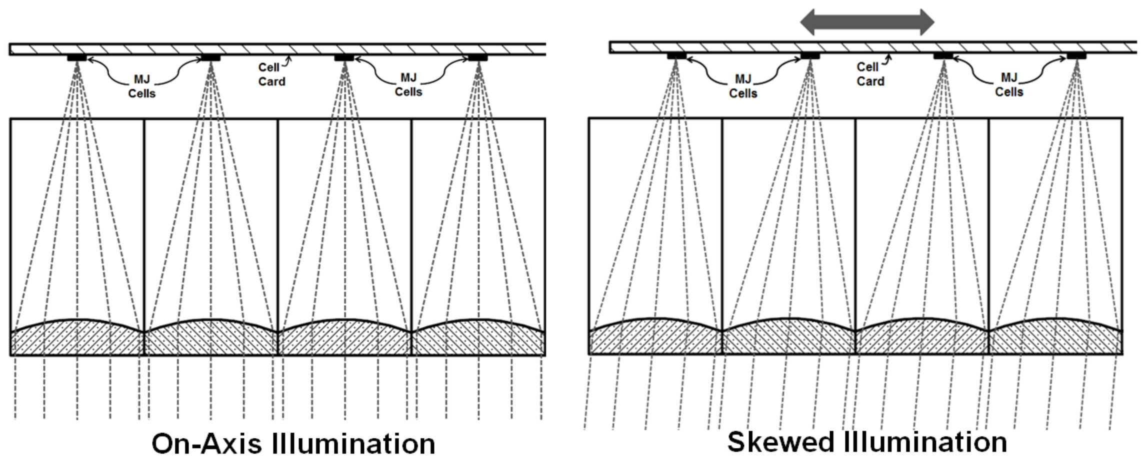


Figure 2.24: Lateral motion between cell strips and toroidal lens array allows tracking over -23.5°<ϑ<23.5°, the residue from polar-aligned single-axis tracking.

For larger incidence angle ranges, Petzval curvature becomes significant. Splitting power between the inner and outer toroidal surfaces helps, but -28.1°<ϑ<55.7° is too great a range to maintain performance with only linear motion. Figure 2.25 shows rays traced through a single outward-facing toroidal lenticulation from two extremes. The foci are nowhere near the same plane. Tilting the toroidal elements biases performance to the winter solstice noon case. Figure 2.26 shows a tilted element illuminated over a range of incidence angles from -26º to +55º and the arc of best focus (dashed line). This is the relative motion required between the toroidal lens and cell plane.

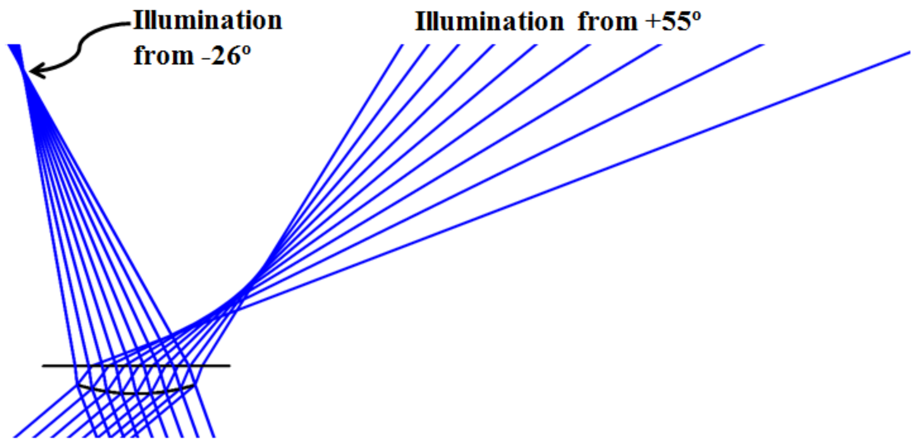


Figure 2.25: Lateral motion between cell strips and toroidal lens array allows tracking over -23.5°<ϑ<23.5°, the residue from polar-aligned single-axis tracking.

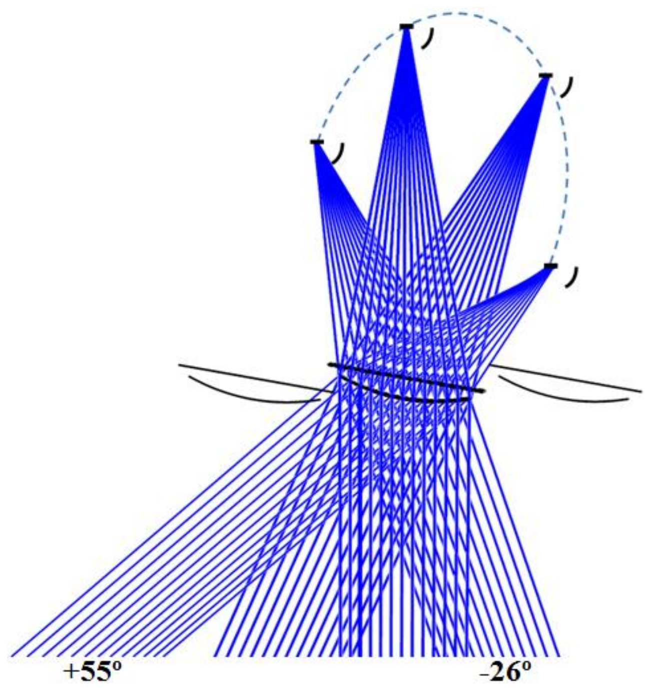


Figure 2.26: Arc motion required to compensate for -26°<ϑ<55°, the residue from horizontal NS-aligned single-axis tracking.

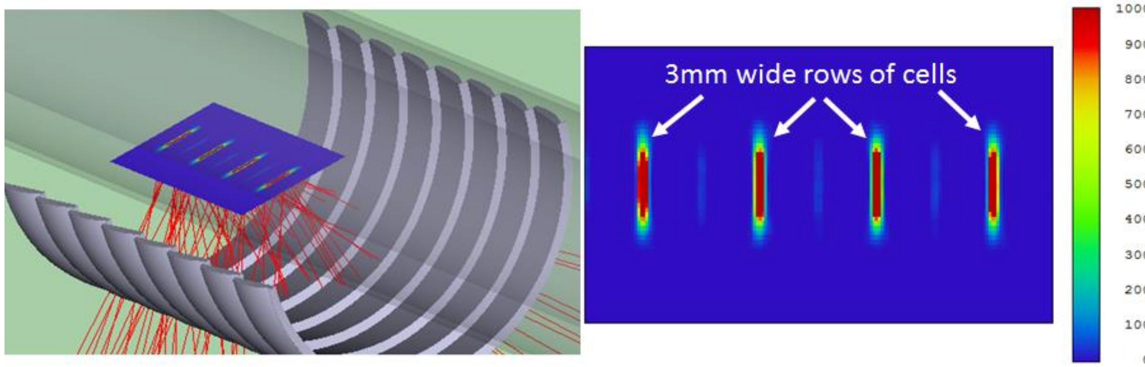


Figure 2.27: Tilted toroidal arc elements illuminating 3 mm-wide cell strips. Scattered light between cell strips is from inactive transition regions between the lenticulations.

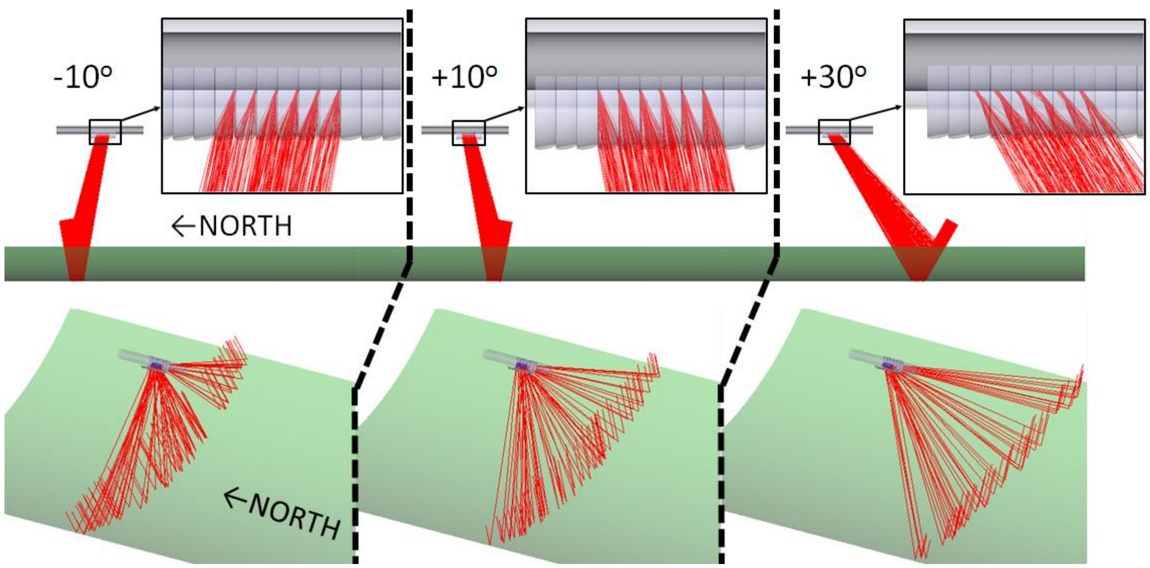


Figure 2.28: The tilted toroidal lens array sweeps out an arc motion to compensate for varying skew incidence.

While optically feasible, this tracking-integrated system is likely too complex for low-cost implementation. Although horizontal N-S module tracking is appealing, the resulting secondary optics have external step discontinuities that will make fabrication and cleaning more difficult. Combining the added mechanical complexity of arched motion (two degrees of freedom), the overall system now employs three degrees of mechanical tracking.

Overall, tracking integration to complement polar-axis tracking (Figure 2.24) is more attractive, since only linear relative motion is required between the lens array and cell plane.

# CHAPTER 3: DISH CPV WITH FREEFORM LENSLET ARRAY

The premise of the concentrating solution presented in Chapter 2 rests on the availability of high-accuracy parabolic trough mirrors. The process shown so far to achieve this quality, slump molding, could instead be used to make arbitrary 3D shapes, such as dishes (Angel, Stalcup, Wheelwright, Warner, Hammer, & Frenkel, 2014). Prior work (Coughenour, Stalcup, Wheelwright, Geary, Hammer, & Angel, 2014) has investigated the use of large on-axis paraboloidal mirrors to drive compact CPV modules (Figure 3.1).

Figure 3.1: REhnu CPV system. A 1.65m square dish mirror drives MJ cells in a compact Köhler optics package.

A very different approach by Semprius (Figure 3.2) utilizes a sheet of glass or silicone-on-glass (SOG) lenslets to illuminate small secondary optics and sub-millimeter cells. Reducing the optical unit size has several scaling benefits, including improved thermal management and the availability of innovative wiring (Nielson, et al., 2012).

However, the Semprius approach still requires large-area, high-transmission lenslet arrays.


Figure 3.2: Semprius module (Semprius, 2012). A square lens array illuminates an array of small ball lenses, each conjugate to a sub-mm MJ cell (Wang, 2012).

Combining these approaches, this chapter will use a 1.6 m square dish reflector to illuminate a freeform lenslet array at 50X concentration. The lenslet array, with ball lenses over each cell, works like a high-density Semprius module. This approach retains many of the scaling benefits discussed in (Nielson, et al., 2012) while performing the large area collection with a fundamentally low-cost mirror (Angel, Stalcup, Wheelwright, Warner, Hammer, & Frenkel, 2014).

### 3.1 Primary Mirror Design

For simplicity, we will design for an on-axis collector to take advantage of quadrant symmetry. The approach can readily be generalized for a freeform off-axis dish, but the number of unique lenslet prescriptions increases by a factor of four. The system geometry and coordinate system are shown in Figure 3.3. Using a 1.5 m focal length parabola as a starting point, a receiving surface is displaced 200mm from the focus. This brings the average concentration in this plane to ~50X.

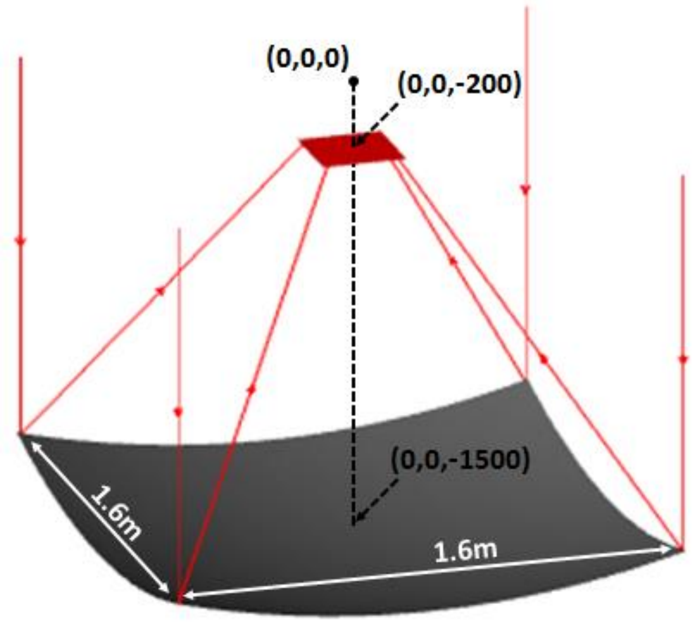


Figure 3.3: On-axis dish geometry and coordinate system.

An on-axis, square aperture dish is readily tailored to produce a flat, square, uniform illumination pattern utilizing only two degrees of freedom (radius and conic). A simple merit function is used to specify the desired square footprint on this target surface. Figure 3.4 shows the irradiance distribution, in units of geometric concentration, on the receiving surface given by a parabolic dish and an optimized conic.

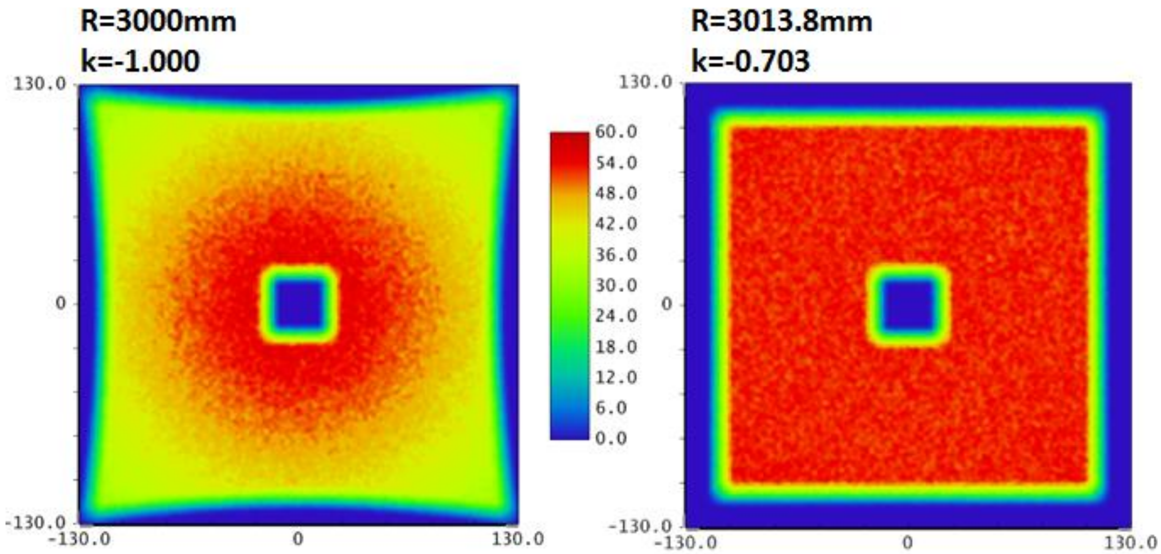


Figure 3.4: Irradiance distribution for parabolic dish (left) and prolate ellipsoid (right).

Besides the central obscuration and the rounding of the edges caused by convolution with the solar disk, the irradiance pattern given by the ellipsoidal mirror is substantially uniform. This surface acts as the entrance face of the freeform lenslet array to be designed in Section 3.2.

### 3.2 Freeform Lenslet Array Design

In the Semprius approach, each primary lens element is illuminated on-axis. In our case, the lenslet array is illuminated at ~50X concentration, with the center and edge lens elements receiving light from different regions of the primary. Thus, the ideal prescription changes as a function of lens element position. To prevent soiling and allow for cleaning, the first (or outer) lenslet surface must be a continuous flat face. All prescriptive power must be on the 2$^{nd}$, inner face. The result of this section is a freeform lenslet array for which each element is uniquely optimized according to its location. Due to symmetry, we are only required to design for one quadrant of the system.

Table 3.1: Design parameters for on-axis freeform lenslet array.

| | |
|---|---|
| Primary Dish Dimensions | 1.6 m X 1.6 m |
| Primary Dish Prescription | R=3013.8 mm k=-0.703 |
| Lenslet Location | 1300 mm from dish vertex |
| Lenslet Aperture | 16X16 array; 15 mmX 15mm each |
| Lenslet Element Center Thickness | 7 mm max |
| MJ Cell Location | 30 mm from vertex of freeform surface |
| MJ Cell Dimensions | 4 mm X 4 mm |
| Geometric Concentration | 700X |

Parts of the lenslet element design can be approached analytically. Near the vertex, the optimal lenslet prescriptions will resemble tilted Cartesian ovals. However, the optimal prescriptions of the edge lenslet elements depart substantially from conventional rotationally symmetric descriptions. Furthermore, it is difficult to anticipate the intersections of adjacent elements required to balance flux between cells. The design was approached numerically with an iterative optimization process implemented in Zemax Programming Language (ZPL). This process, summarized in Figure 3.5, utilizes native surface descriptions in both sequential and nonsequential modes of ZEMAX. Individual, over-sized lenslet elements are designed in sequential mode for rapid pupil sampling, ray aiming, and aberration analysis. First, the macro runs optimizations on all 64 lenslet elements (one quadrant). Sufficient imaging performance is achieved by varying radius, conic, and Zernike terms Z5-Z16 (from astigmatism up to secondary spherical). These 64 initial prescriptions and image positions are passed to a non-sequential model, which assembles the system, traces $10^7$ rays (for an average $39(10^3)$ rays per cell), and analyzes the flux variation between cells. If a cell receives less flux than its neighbor, the piston term (Z1) of its corresponding lenslet is scaled up so that the lenslet receives more light. This "bubbling up" process is iterated until the flux is uniform across all cells.

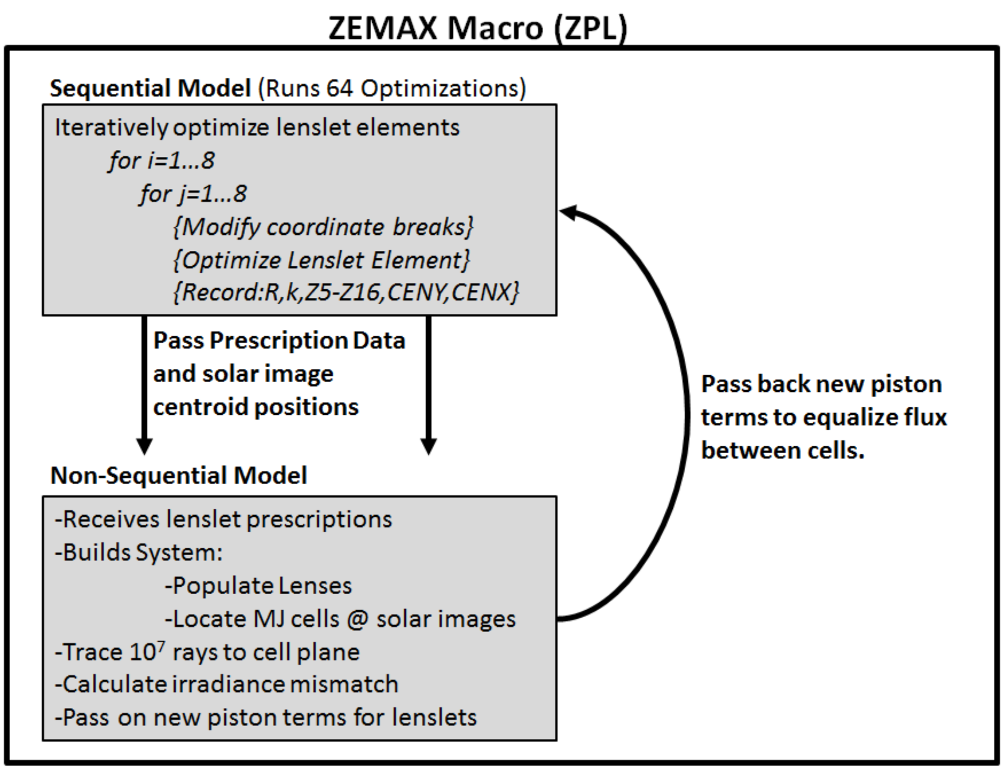


Figure 3.5: Freeform lenslet design process, implemented in ZPL.

Figure 3.6 compares a single quadrant of a regular lenslet array, with square tessellation, and the freeform lenslet array resulting from ZPL optimization. Note that the lenslet tessellation becomes irregular away from the center elements. This tessellation emerges naturally from the bubbling-up design process.

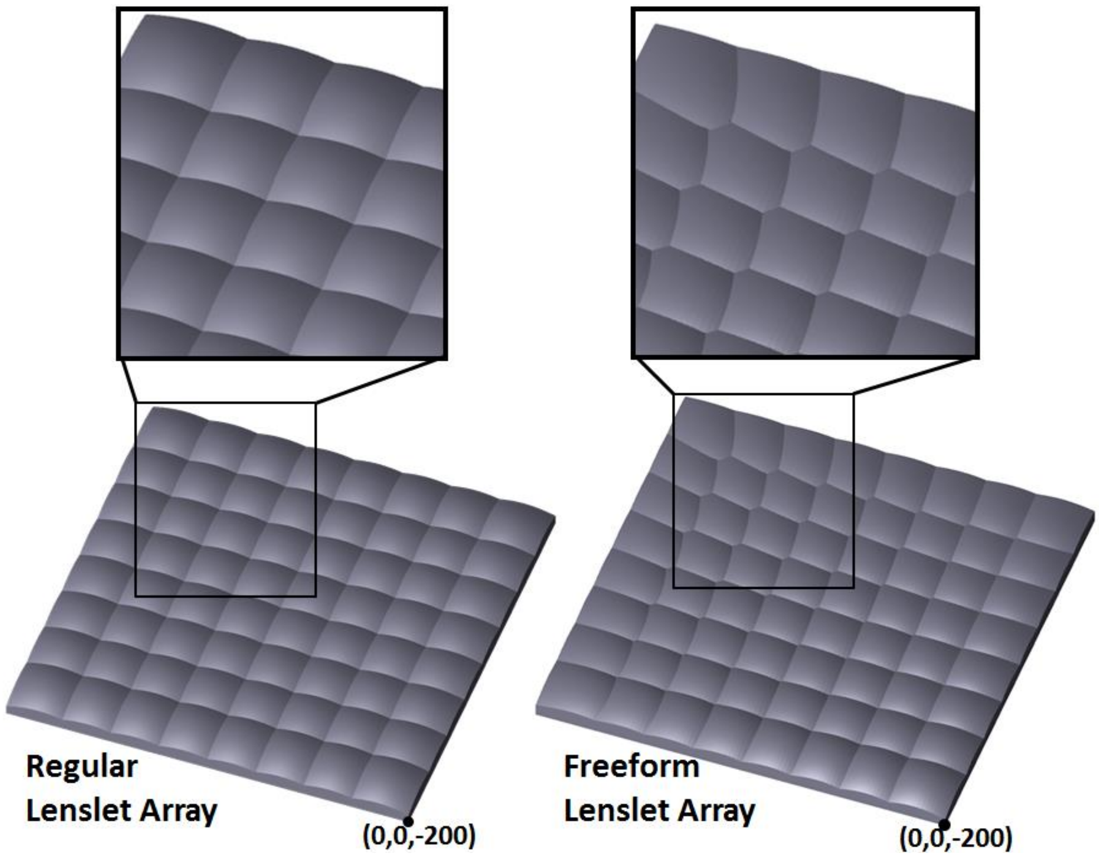


Figure 3.6: Regular lenslet array and freeform lenslet array (one quadrant only).

Since each lenslet element is specifically tailored to image the tilted bundle of light it receives, it forms tight solar foci. Figure 3.7 compares the imaging performance of one quadrant of a regular lenslet array and the freeform array.

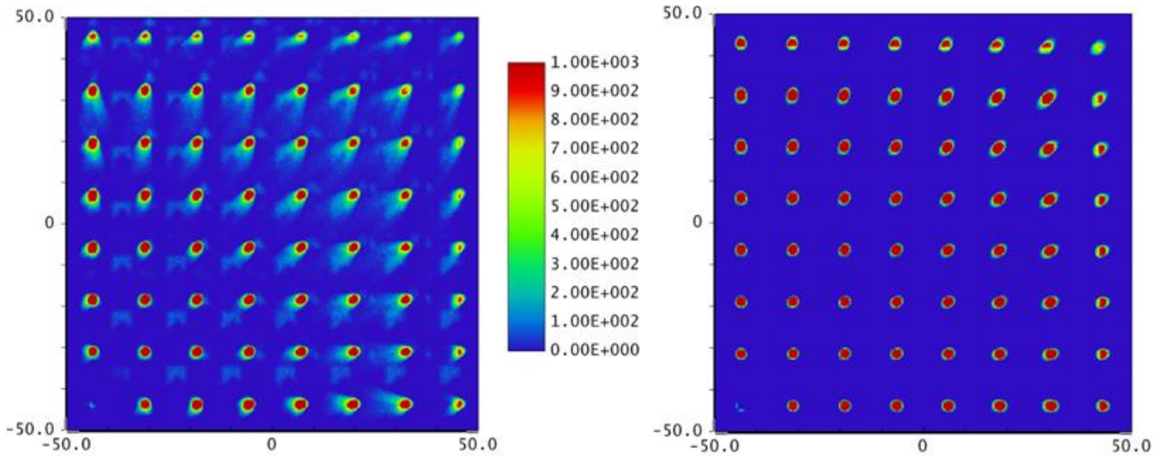


Figure 3.7: Imaging performance of regular lenslet (left) and freeform lenslet (right) arrays.

As built, this system places a solar focus on each 4 mmX4 mm cell. With perfect tracking, the solar foci are centered on the cells. With tracking errors, the solar foci are laterally translated off the cell, as shown in Figure 3.8.

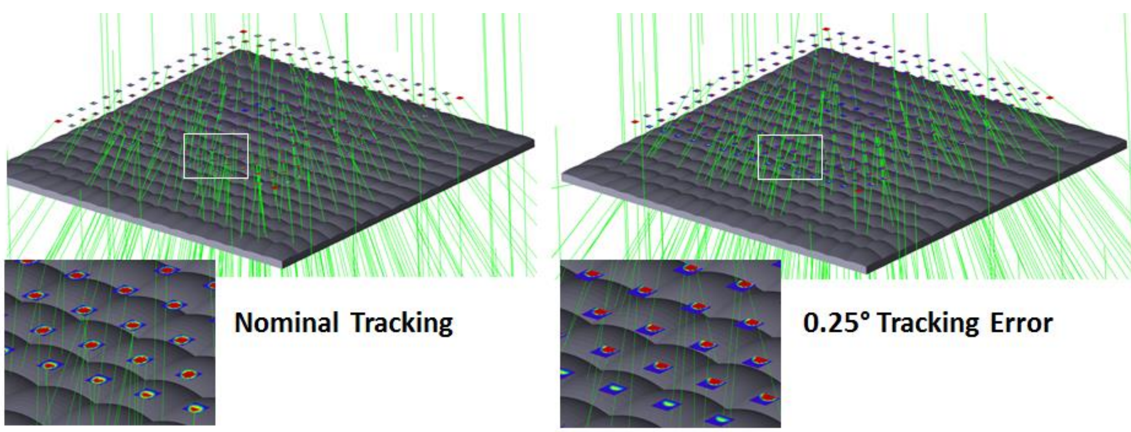


Figure 3.8: Solar foci displacement with tracking errors.

The problem shown in Figure 3.8 can be addressed with Köhler stabilization (Koshel, 2013). Semprius uses small ball lenses to improve their acceptance angle. The lenslets image the Sun into the center of each ball lens. Each ball lens images the outline of the lenslet onto the cell. Thus, as long as the solar image remains within the working pupil of the ball lens, the cell remains illuminated. Another CPV system using a spherical secondary optic for Köhler stabilization is described by (Coughenour, Stalcup, Wheelwright, Geary, Hammer, & Angel, 2014) and is commercialized by REhnu, Inc.

To include Köhler stabilization in this system, we need only replace the MJ cells with ball lenses (6 mm diameter) and place MJ cells farther back, as shown in Figure 3.9. The irradiance pattern is not circular because the solar disk is no longer being imaged onto the cells. The pattern is roughly rectangular, corresponding to the ball-formed image of each lenslet element border.

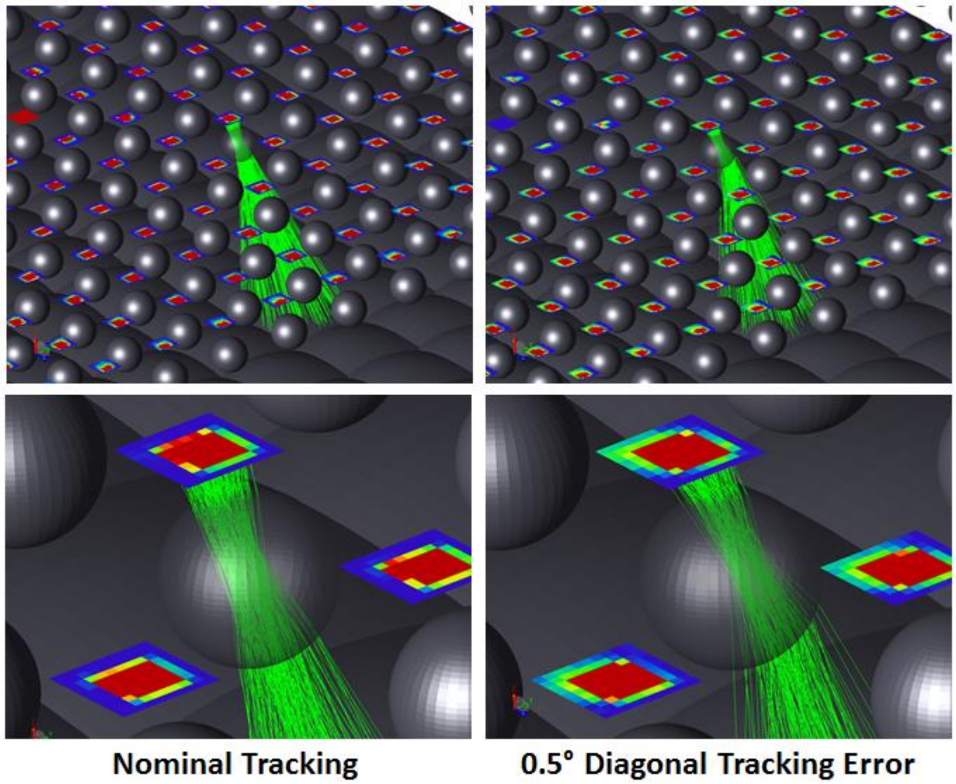


Figure 3.9: Irradiance on MJ cell stabilized by ball lenses.

### 3.3 Tracking Performance and Electrical Compensation

An ideal module would provide equal flux to each cell to allow series connection of the whole chain. This minimizes currents, reducing resistive losses. The Semprius approach has the advantage of providing equal flux to each cell unless part of the module is shaded, soiled, or otherwise damaged. Current-limiting cells are preferably cut out of the chain with bypass diodes. In the approach described in Section 3.2, the dish provides a uniform square illumination pattern, but this pattern has a central obscuration and the edges fall off in irradiance according to the width of the solar disk (Figure 3.4). After passing through the lenslet array and ball lenses, the resulting geometric concentration on each cell has significant variation (Figure 3.10). Of the 256 cells in the system, those along the outer edge and edge of the obscuration receive about half power compared to the cells in the uniform region.

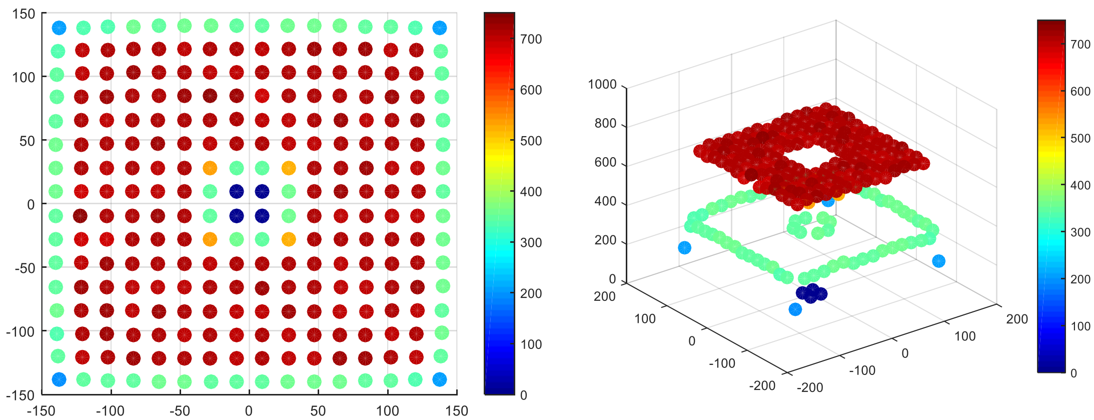


Figure 3.10: Flux distribution on cells (geometric concentration in z-axis and colorbar). X and Y axis are position of the cell in mm.

Arranging the cell power from highest to lowest in a histogram gives a cell power distribution curve for the system (Figure 3.11). This curve is analogous to a system IV curve. Just as an IV curve indicates the optimal operating voltage for a PV cell, the power distribution curve of Figure 3.11 indicates how many cells in the chain should be bypassed to reach maximum system power. Although this curve will look similar to the final system IV curve, it does not take into account the electrical characteristics of each cell. In this case, bypassing the inner and outer edge cells attains maximum system power. The power generated by bypassed cells is a direct loss to system efficiency.

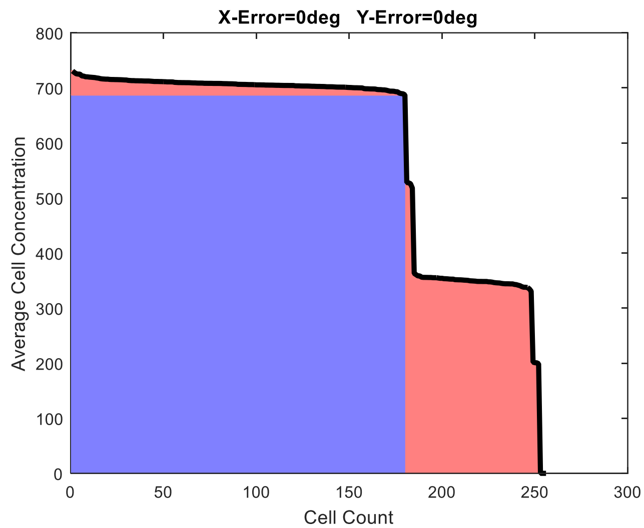


Figure 3.11: Cell power distribution curve with nominal tracking. Max power condition shaded blue.

To mitigate the edge drop-off we can implement another degree of freedom: wiring. By wiring opposite cells (by 180° rotation) in parallel, we can vastly improve the pseudo-IV curve. The required wiring for a 16X16 cell array is too complex to draw. However, a partial, unwrapped wiring diagram is shown in Figure 3.12.

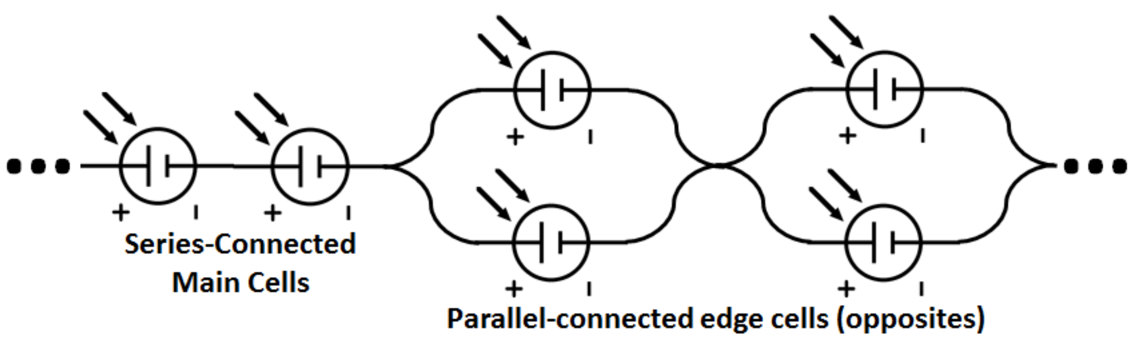


Figure 3.12: Main cell and edge cell wiring.

To simulate this new wiring scheme, we simply add the flux of opposite cells to a new, virtual cell. For the purpose of visualization, we will cut out half of the edge cells and add their power to opposite cell. Two edges now have boosted power and two edges are dropped to zero, as shown in Figure 3.13.

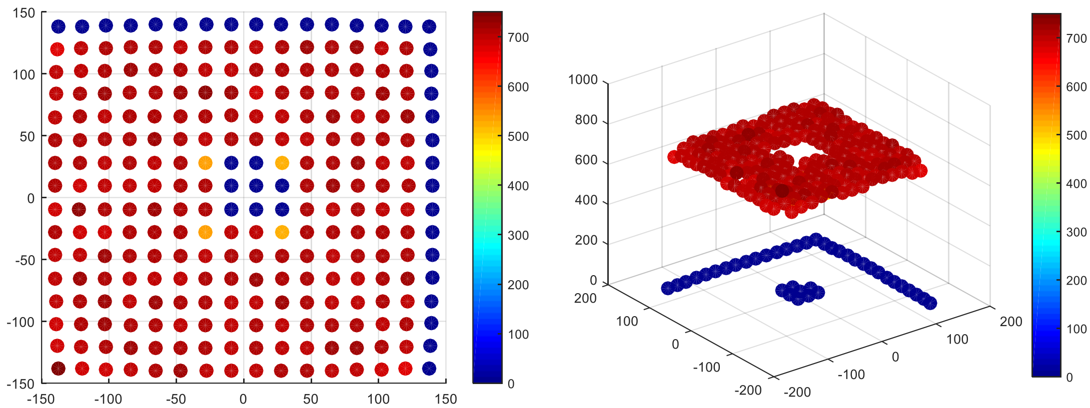


Figure 3.13: Flux distribution on cells (geometric concentration) with parallel wiring of outer and inner edge.

The new pseudo-IV curve is shown in Figure 3.14. By wiring the edge cells in parallel pairs, the new virtual cells now provide current compatible with the main body of cells.

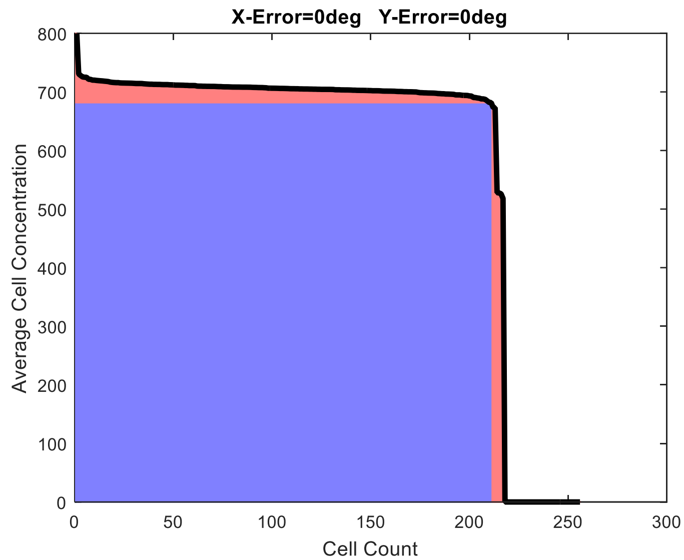


Figure 3.14: Cell power distribution with nominal tracking and parallel wiring of edge cells. Maximum power condition is shaded in blue.

The total area under the black curve of Figure 3.14 is proportional to the total optical power received by the cells, $P_{total(on\text{-}axis)}$. The area inside the blue box is proportional to the power available for extraction based on the wiring scheme, $P_{chain}$. When tracking errors are introduced, this ratio changes due to drop-off in optical throughput *and* current flux mismatch between cells. Figure 3.15 shows the off-axis performance of a system wiring strictly in series (left) and wired with edge cells in parallel (right).

The off-axis performance of this optical system was analyzed with a ZPL macro in which $2.5*10^7$ rays (nearly $10^5$ rays per cell) are traced for each off-axis tracking case. Tracking errors were sampled over a regular grid up to 0.5° in the X and Y directions.

Due to symmetry, negative tracking errors are equivalent, so only one tracking quadrant is shown. For the all-series case (left) on-axis $P_{chain}/ P_{total(on\text{-}axis)}$ is only ~83%, which corresponds to the ratio of areas in Figure 3.11. The on-axis $P_{chain}/ P_{total(on\text{-}axis)}$ ratio for the parallel wiring case is nearly unity, corresponding to the ratio of areas in Figure 3.14.

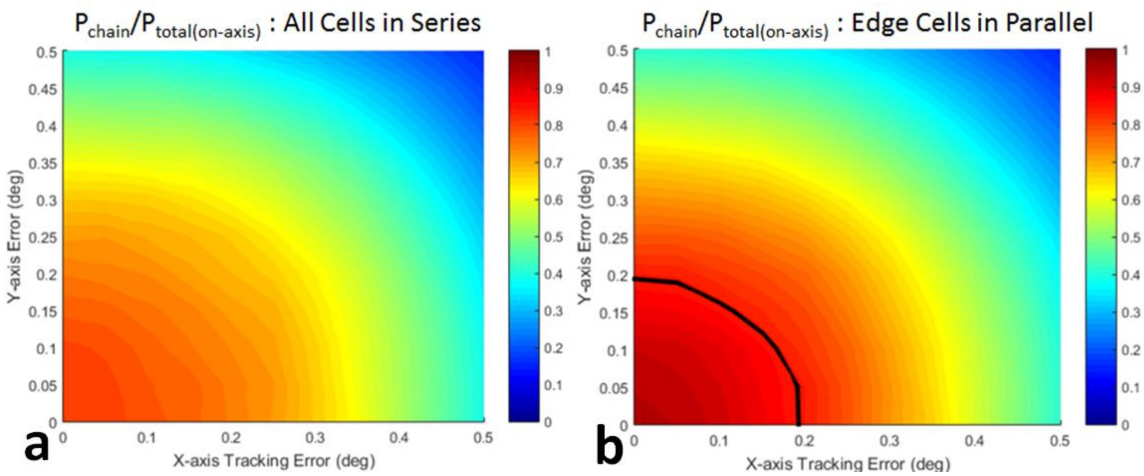


Figure 3.15: $P_{chain}/ P_{total(on\text{-}axis)}$ for all cells in series (a) and edge cells in parallel pairs (b). Black line is the 90% contour (compared to on-axis).

Wiring the edge cells in parallel pairs vastly improved the on- and off-axis performances, but the 90% case is still reached with only 0.20° tracking error. The drop-off is due to two effects: flux mismatch between cells and the breakdown of Köhler stabilization at the edges.

### 3.4 Sensitivity to Figure Errors

Section 3.3 considered the optical and electrical sensitivity to tracking errors. This section models scatter and figure errors in the primary mirror. Figure 3.16 shows the cell power distribution for a perfect mirror (top) and a mirror with 4mrad Gaussian scatter, approximating slope errors with very high spatial frequency. This additional error hardly changes the cell-to-cell flux variation, indicating robustness to high frequency scatter.

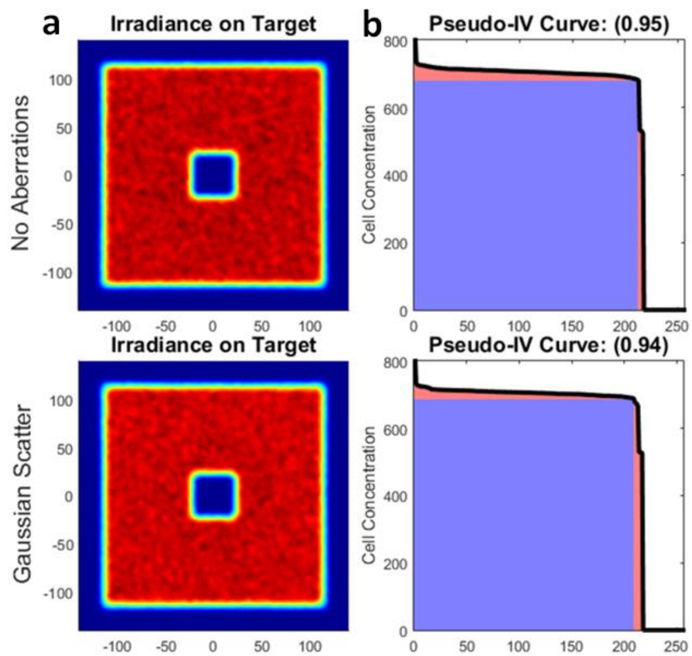


Figure 3.16: Comparison between an error-free mirror (top) and a mirror with 4mrad rms Gaussian scatter (bottom). (a) is the irradiance map on the receiving surface (same scale as Figure 3.4). (b) is the Pseudo-IV curve indicating geometric concentration over all 256 cells.

Figure errors directly impact the irradiance distribution in the lenslet plane, and thus are more likely to affect cell-to-cell flux variation than high-frequency scatter. Figure 3.17 shows the effect of three aberrations: tilt (top), astigmatism (middle) and vertical quadrafoil (Z14, bottom), all scaled to give 2 mrad RMS slope error, or 4 mrad RMS ray error.

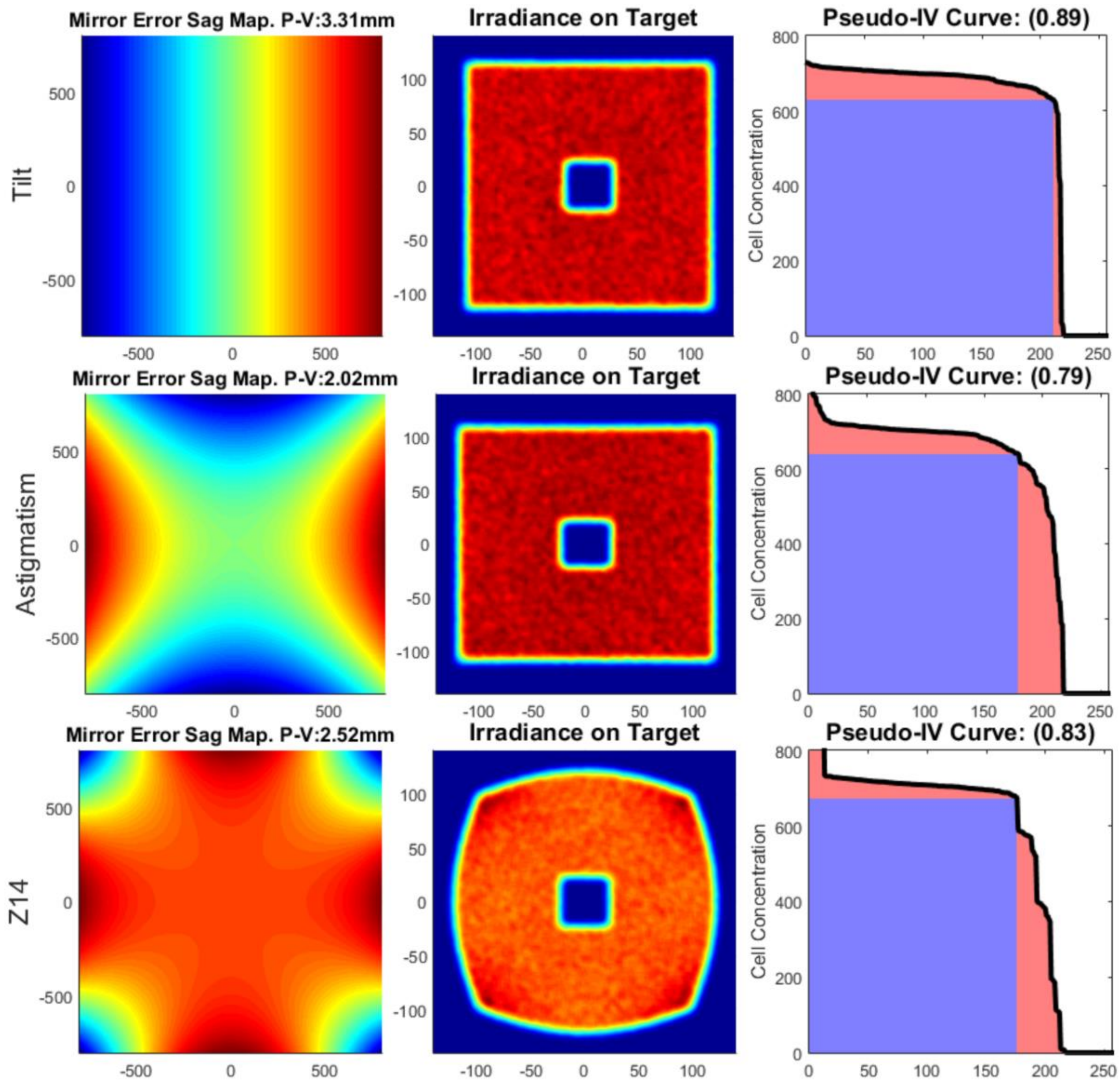


Figure 3.17: The effect of tilt (top), astigmatism (middle), and quadrafoil (bottom), each scaled to give 2mrad rms slope error. Sag maps (left column) are in mm with each color map scaled to the P-V range. Irradiance maps (middle column) have the same scale as Figure 3.4. Pseudo-IV curves (right column) with absolute $P_{chain}/ P_{total(no\ errors)}$.

Note that tilt errors are equivalent to tracking error and are well corrected up to 0.20° due to the parallel wiring scheme of Section 3.3.

## 3.5 On-Axis Paraboloidal Dish and "Inverted Fly's Eye" Array

Suppose one ignores the flux variation between cells and only considers *optical* throughput. With enough low-current cells, perhaps innovative wiring could compensate for flux variations between cells (Lentine, Nielson, Okandan, Cruz-Campa, & Tauke-Pedretti, 2014). Invoking this argument, we then seek to maximize the optical throughput without much concern for flux variation. The freeform lenslet array designed in Section 3.2 is limited by the off-axis performance of the edge elements. Near the center of the lenslet array the ball lenses satisfy the Scheimpflug condition; see (Greivenkamp, 2004). This condition is not met near the edge of the lenslet array, so the ball lenses form a stabilized irradiance pattern that is tilted with respect to the cells. This can be corrected by allowing a non-planar cell card. By tessellating the cells, ball lenses, and lenslet elements over a spherical surface, this Köhler stabilization approach will perform more effectively out to the edges of the array. Although this curved lenslet array appears more complex than a flat array, the design and modeling of such a lens is actually much easier, since each lenslet prescription is a simple conic.

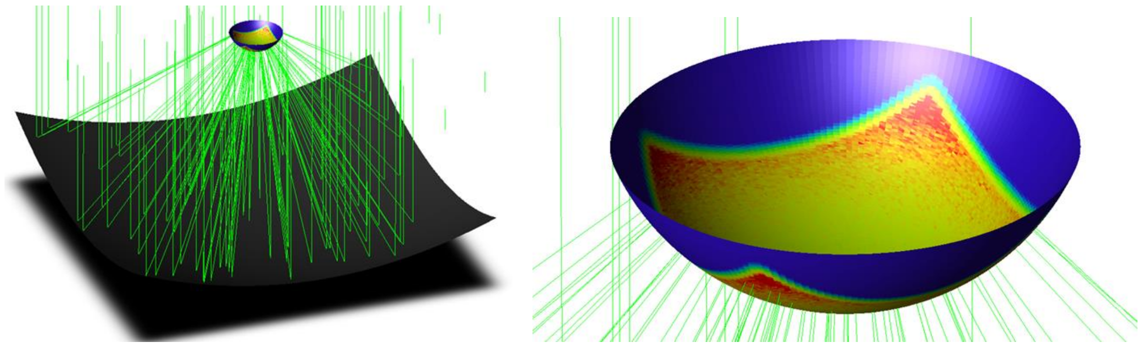

Figure 3.18: 1m EFL dish (1.65 m x 1.65 m) and a spherical detector of radius 126mm.

The irradiance on this spherical surface varies according to:

$$C = \frac{A_1}{A_2} = \left(\frac{f}{b}\right)^2 \left(1 + 2tan^2\left(\frac{\theta}{2}\right) + tan^4\left(\frac{\theta}{2}\right)\right), \tag{3.1}$$

where *f*, *b*, and $\theta$ are defined in Figure 3.19. This formulation originally appears in (Angel R. , 2009) and a derivation is given by (Coughenour, Stalcup, Wheelwright, Geary, Hammer, & Angel, 2014).

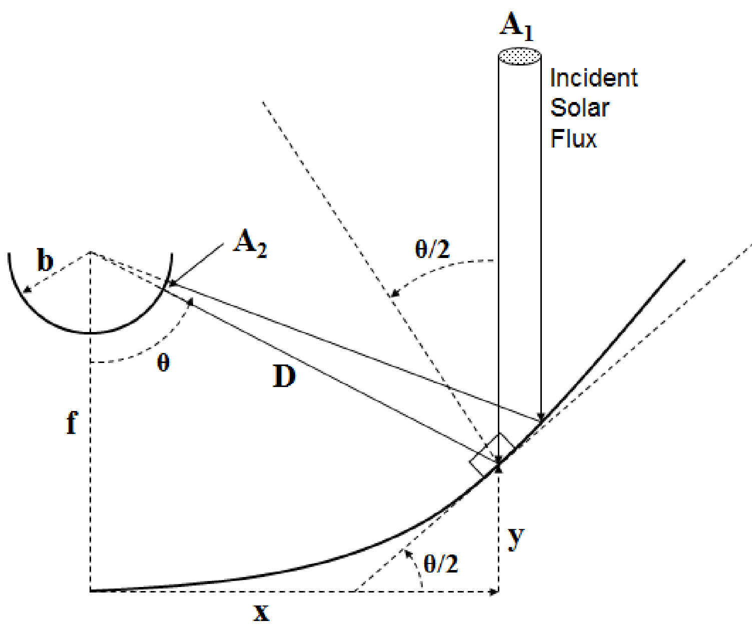


Figure 3.19: Geometry for a curved receiving surface.

With the curved receiving surface ($b$=126 mm), we can operate with the very fast 1 m EFL dish shown in Figure 3.18, giving a maximum $\theta$=60.5º. Geometric concentration at the receiving surface will thus vary from C=63X at the vertex to C=113X at the corner.

To separate the sunlight for distribution onto individual cells, the receiving surface is tessellated with a 20x20 grid of B270 lenses, forming a continuous smooth outer spherical surface ($R$=126 mm) and an 'inverted fly's eye' on the interior surface. The lenslet interior surfaces are conics optimized to focus to a point 14.5 mm from the lenslet vertex. The position of each lenslet is determined by (1) dividing the dish aperture into an equal-area 20x20 grid, (2) calculating the vector from the prime focus to the centroid of each dish region, and (3) projecting this vector onto the desired receiving surface ($R$=126 mm). As over-sized lenslets populate the receiving surface, their intersections naturally generate smaller areas near the corners, completely compensating for the irradiance variation of Equation 3.1.

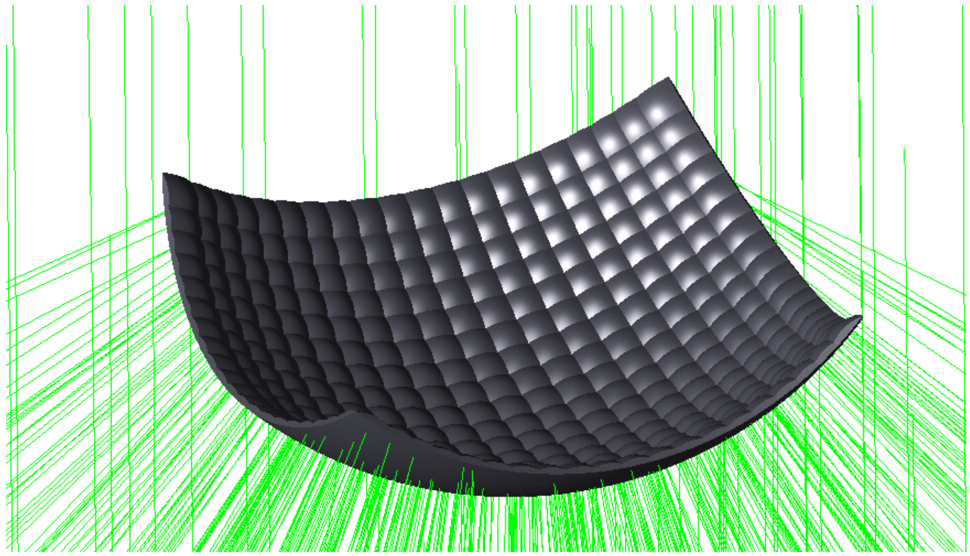

Figure 3.20: Curved lenslet array ("inverted fly's eye") with smooth outer surface.

Each lens element forms an intense focus that will drift laterally from tracking errors. Placing 4 mm diameter spherical ball lenses at the foci establishes square, Köhler-stabilized concentration areas (the ball-formed image of the lenslet). 2 mm square MJ cells are positioned behind each ball lens (Figure 3.21). The edge lens elements (78 total) are slightly over-sized, so 3 mm cells are needed.

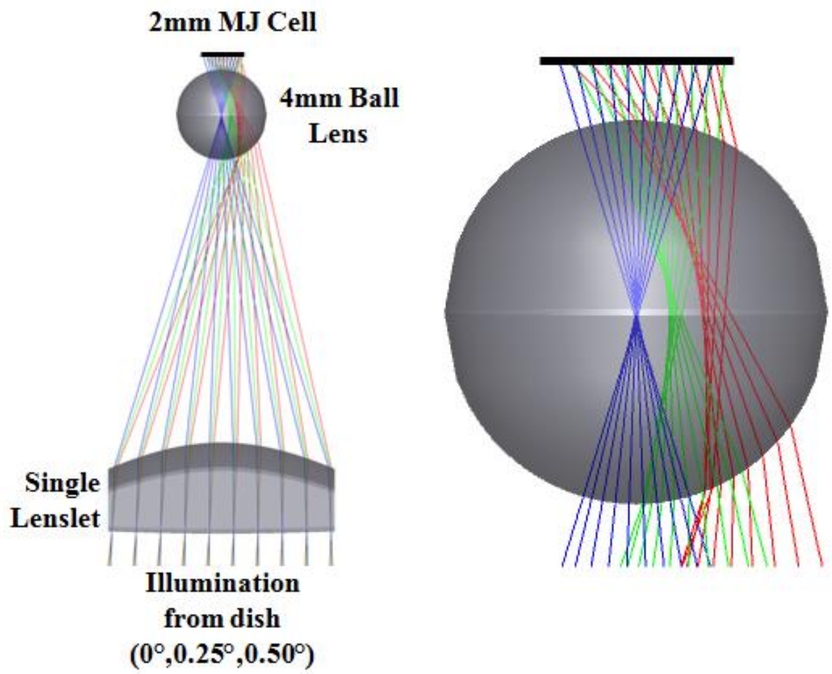


Figure 3.21: Curved lenslet with corresponding ball lenses and cells.

For ideal optical performance, each cell lies on a unique, tilted plane (Figure 3.22). However, with a small sacrifice in optical performance, subgroups of cells could lie on flat cell cards for manufacturing convenience. A CPV system with cells on a concave surface (behind the prime focus) has successfully implemented this tradeoff. An early prototype by The University of Arizona and REhnu (Stalcup, et al., 2012) had cells mounted on 36 individually machined planes in a copper bowl. The latest prototype (Coughenour, Stalcup, Wheelwright, Geary, Hammer, & Angel, 2014) utilizes a slower dish and a four-quadrant cell card to approximate the ideal concave surface.

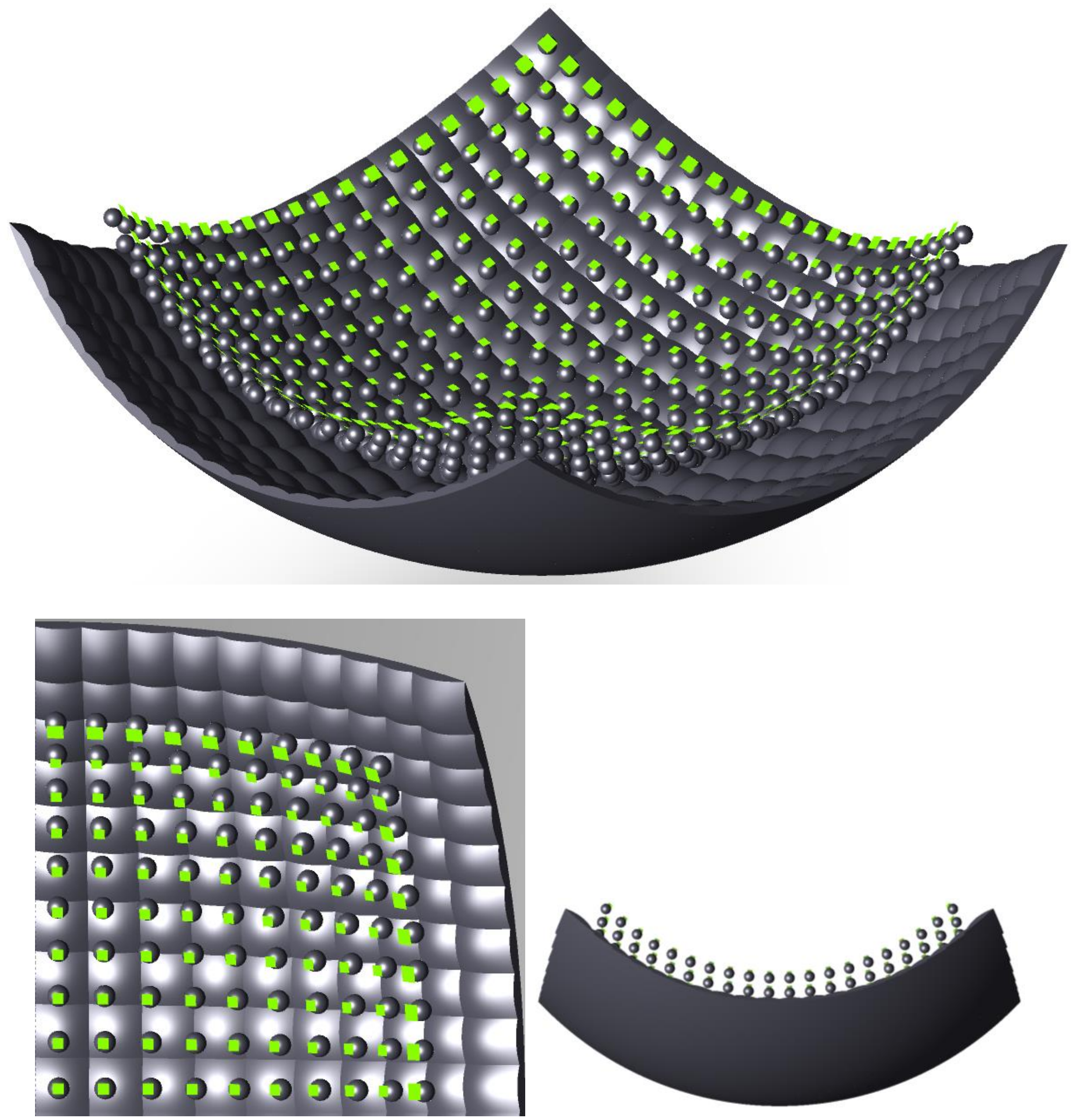

Figure 3.22: Top: Curved lenslet array with corresponding ball lenses and cells. Bottom, left: Single lenslet quadrant. Bottom, right: side view.

.

Figure 3.23 shows the geometric concentration on all 400 cells for on and off-axis illumination. On-axis, the cells all receive nearly equal illumination except the center 4 cells, which are weaker due to the central obscuration. When tracked off-axis, one edge (20 cells) gains power while the opposite edge drops off. Above 0.5°, all cells begin to drop off as Köhler stabilization breaks down. On-axis geometric concentration averages 1600X on the central 322 cells and 700X on the edge cells.

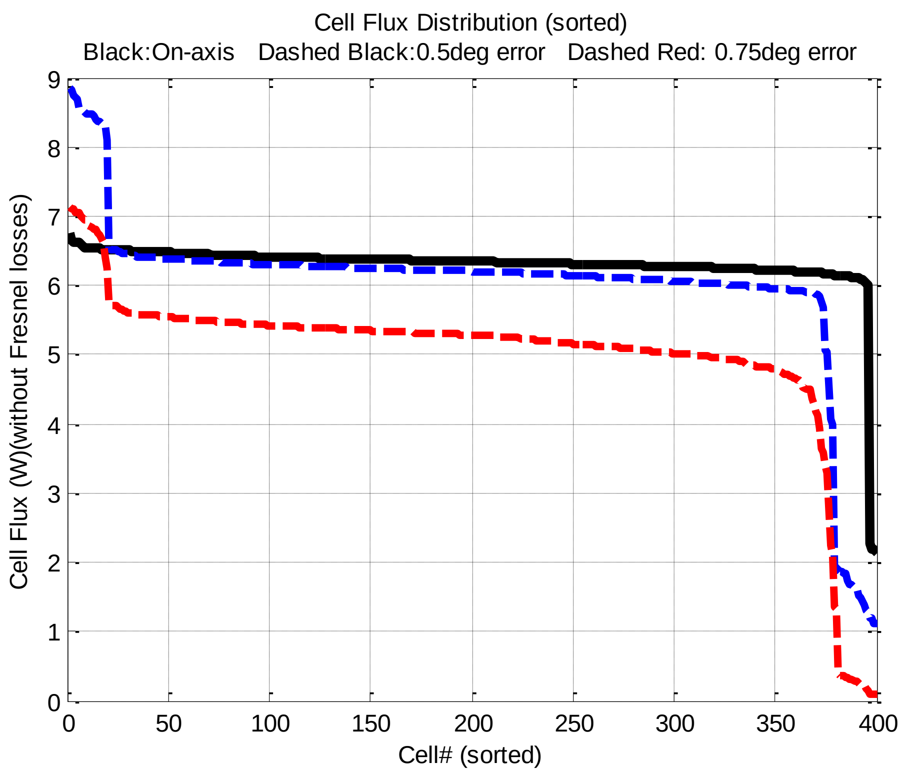


Figure 3.23: Sorted flux distribution (W) on all 400 cells for on-axis illumination (black line), 0.5° tracking error (dashed blue line), and 0.75° tracking error (dashed red line).

Raytracing analysis shows that the total optical throughput drops to 90% at +/- 0.53° tracking error (Figure 3.24).

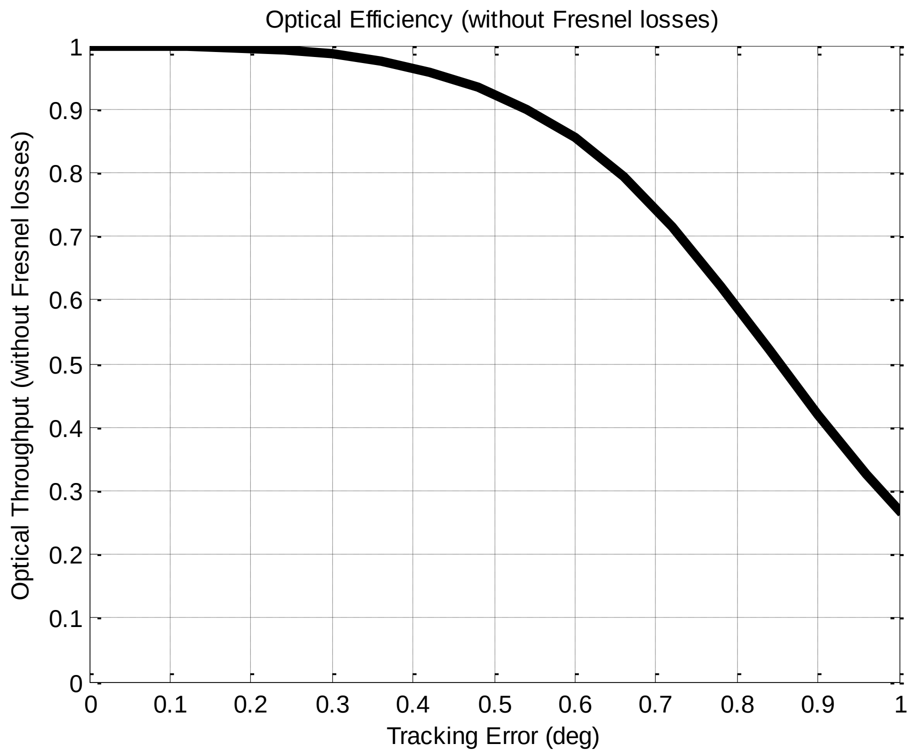


Figure 3.24: Optical throughput (without Fresnel losses) vs tracking error.

### 3.6 Off-Axis Paraboloidal Dish and "Inverted Fly's Eye" Array

One disadvantage of the on-axis dish system in Section 3.5 is the central obscuration, which blocks ~2.5% of incoming light. Using the same lenslet design method, we can build an off-axis system without obscuration, such as that shown in Figure 3.25. Figure 3.26 shows the irradiance variation on a receiving surface of 126mm radius (left) and a freeform lenslet tailored to distribute equal flux to cells (right). The lenslet size rapidly decreases off-axis. As before, edge elements are oversized.

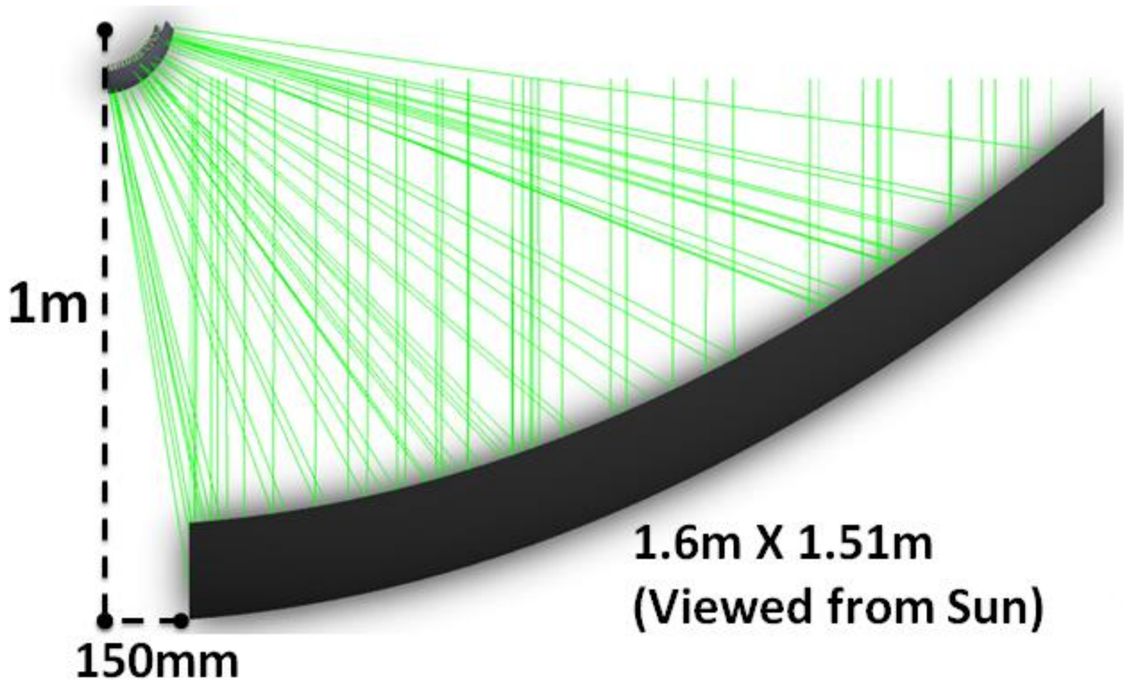


Figure 3.25: Off-axis 1m EFL dish and freeform receiver on 126 mm receiving surface.

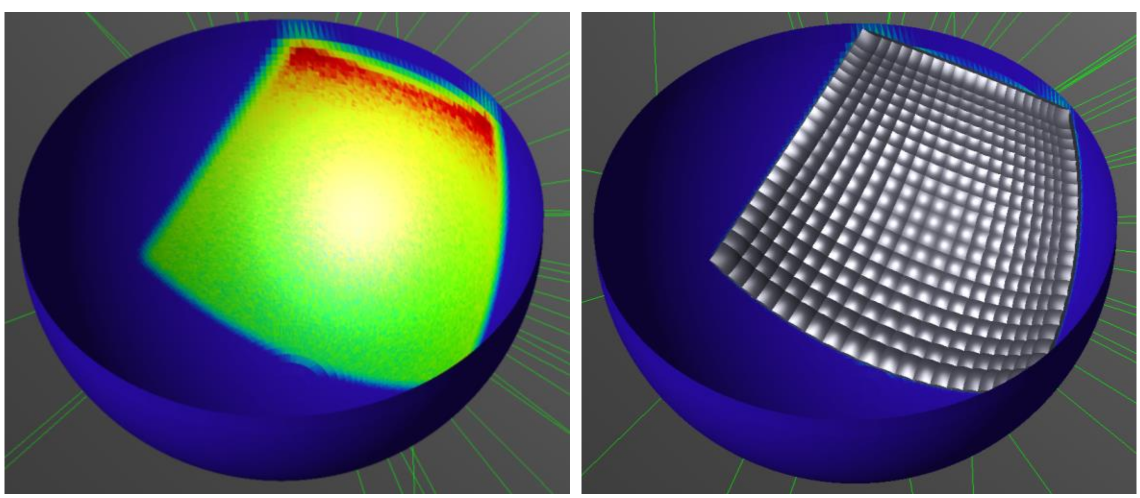

Figure 3.26: Irradiance distribution on R=126 mm surface (left) and freeform lenslet for equal flux distribution (right).

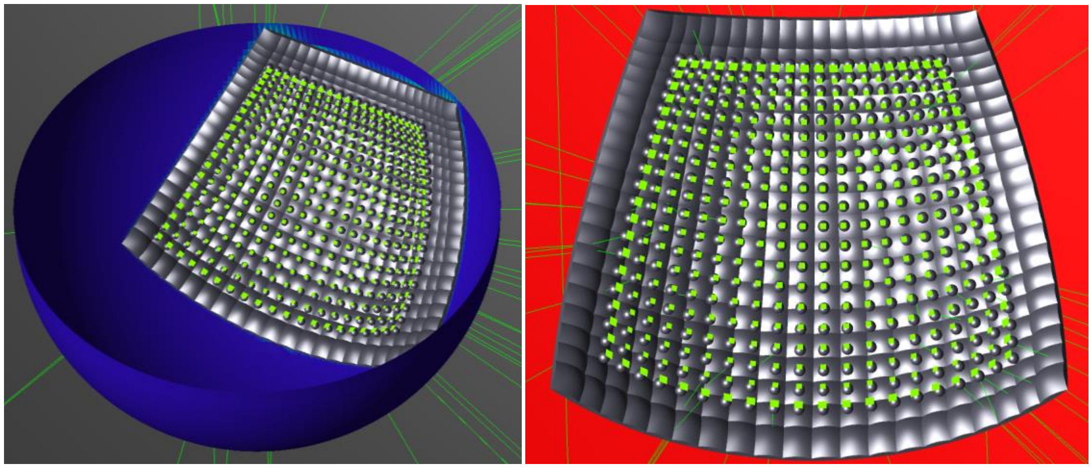

Figure 3.27: Two views of the freeform lenslet array, ball lenses and cells.

In this model, central cells are 2 mm square and edge cells are 3mm square. A fully optimized system would allow more cell sizes, each tailored to the stabilized irradiance pattern produced by each lenslet/ball lens pair. As before, the lenslet tesselation emerges naturally from the process described in Section 3.5. The resulting flux distribution, assuming no tracking errors, is nearly perfect (Figure 3.28, black line). The distribution is similar to Figure 3.23 except there are no cells weakened by the central obscuration. The average cell concentration is slightly lower because the effective aperture of the mirror is smaller (only 1.6 m X 1.51 m) due to the cosine projection.

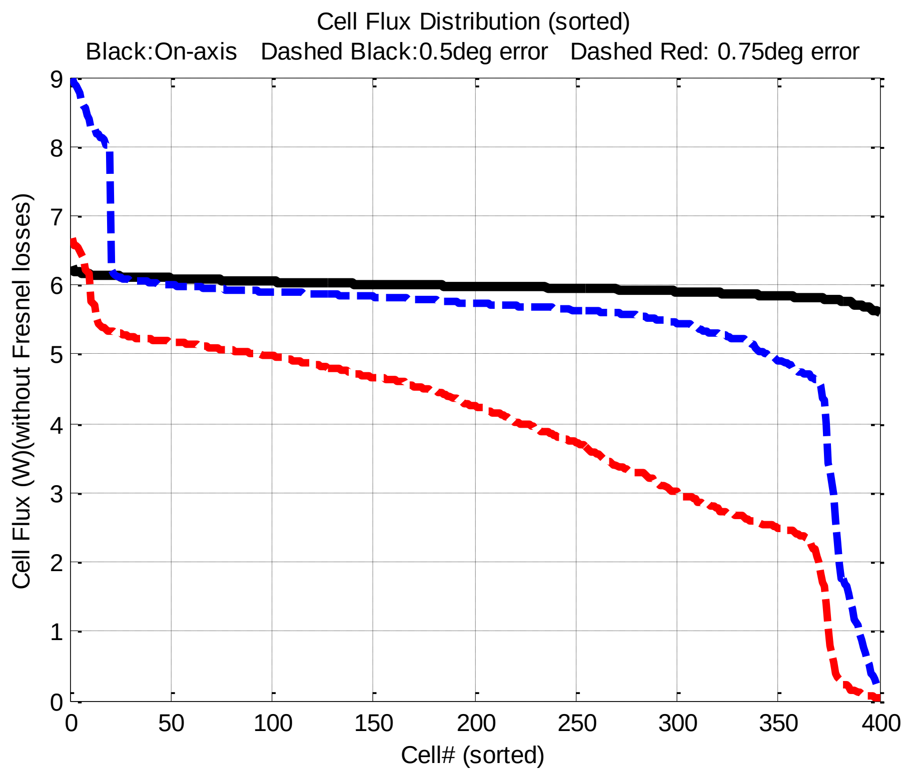


Figure 3.28: Sorted flux distribution (W) on all 400 cells for on-axis illumination (black line), 0.5° tracking error (dashed blue line), and 0.75° tracking error (dashed red line).

With tracking error, the off-axis concentrator shows more sensitivity than the on-axis system. Since the outermost edge of the primary is much farther away, it is not surprising that the irradiance pattern translates off the receiver at a faster pace. However, the overall optical acceptance angle is still +/-0.45° (Figure 3.29). The 322 inner cells (2mm square) are illuminated at 1500X geometric concentration (not including Fresnel or reflection losses). The 78 border cells receive 670X geometric concentration. In all, the average concentration is 1215X.

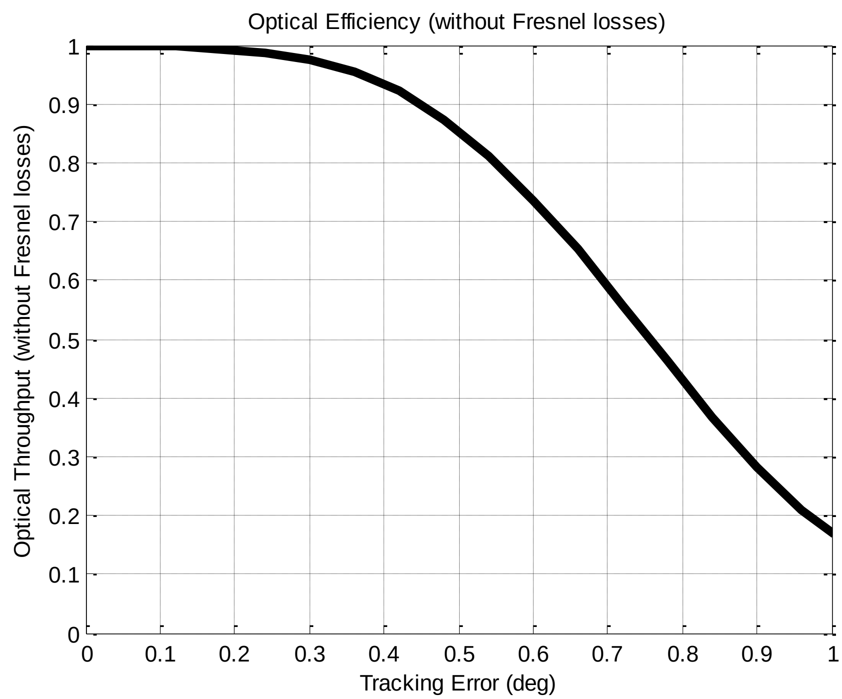


Figure 3.29: Optical throughput (without Fresnel losses) vs tracking error.

In summary, this 'inverted fly's eye' approach allowed a doubling of geometric concentration compared to the flat lenslet in Section 3.2 while also increasing the acceptance angle. This increase is due to the optimized orientation of each lenslet and ball lens so that Köhler stabilization remains effective off-axis. An off-axis layout also avoids the central obscuration. Future work that needs to be done: (1) find suitable groupings of cells which can be combined into planar cell cards; (2) analyze electrical compensation techniques to mitigate flux mismatch; (3) analyze thermal management. The possibility of fan-based thermal management without liquid cooling is especially enticing and is one of the most important scaling benefits described in (Nielson, et al., 2012).

# CHAPTER 4: CSP FIELD COLLECTOR WITH FREEFORM TRACKING

By Department of Energy estimates, central receiver plants currently have the lowest levelized cost of electricity (LCOE) in the CSP market (ARPA-E, 2014). Figure 4.1 shows the cost contributions from each plant component and indirect cost for trough and central receiver systems. The solar field accounts for at least 25% of the plant cost. Figure 4.2 shows the central receiver component cost reductions required to achieve the 6¢/kWh$_e$ SunShot CSP Goal. Note that the solar field requires at least 50% cost reduction to meet the goal. LCOE reductions can result from lower cost per unit area (\$/m$^2$) or higher performance per unit area (kWh/m$^2$).

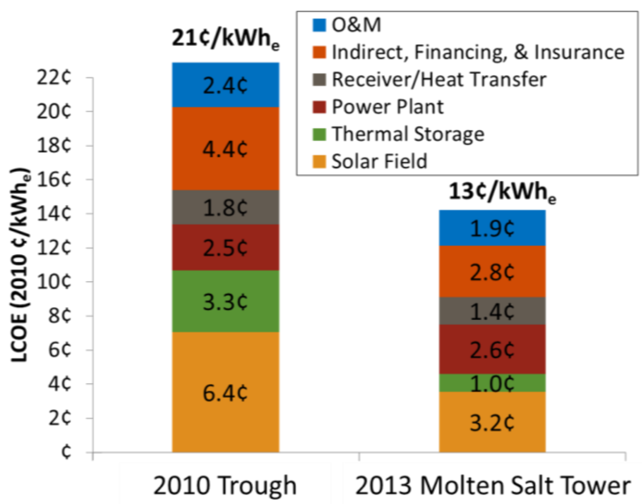


Figure 4.1: LCOE breakdown of CSP trough and central receiver plants (ARPA-E, 2014).

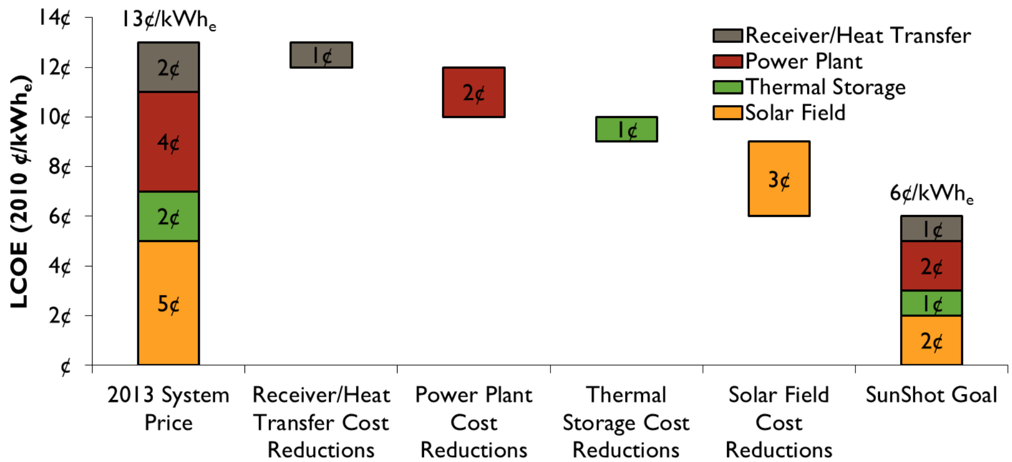


Figure 4.2: Component cost reduction roadmap for CSP central receivers (ARPA-E, 2014). Note that this component breakdown distributes O&M and indirect costs to each plant component (Figure 4.1 does not).

Section 4.1 will review the limitations of current solar field architectures and Section 4.2 will discuss a new approach that achieves very high collection efficiency and concentration.

### 4.1 Field Efficiency Limitations of Central Receiver CSP Plants

Large central receiver plants such as Ivanpah and Tonohpah feature central towers with >100MW receivers and commensurately sized heliostat fields. The annually averaged collection efficiency of CSP central receivers, as measured by $kW_{thermal}/m^2$, is low compared to CSP Trough due to very high obliquity loss. Obliquity is the cosine of the incidence angle of solar rays on the heliostat, or equivalently, the ratio of the projected area of the heliostat to its full aperture. Like soiling and mirror reflectivity, the obliquity factor of a heliostat directly impacts the optical power it can deliver to the receiver. Heliostats surrounding the tower must continuously adjust their pointing to maintain illumination on the tower, so obliquity losses are changing continuously. The obliquity factor is unity in the ideal case, where a heliostat is positioned near the shadow of the receiver. Figures 4.3 and 4.4 illustrate that heliostats near the receiver shadow are ideally positioned to reflect sunlight with low obliquity loss (high obliquity factor) while heliostats between the Sun and tower experience very high obliquity loss (obliquity factor <<1).

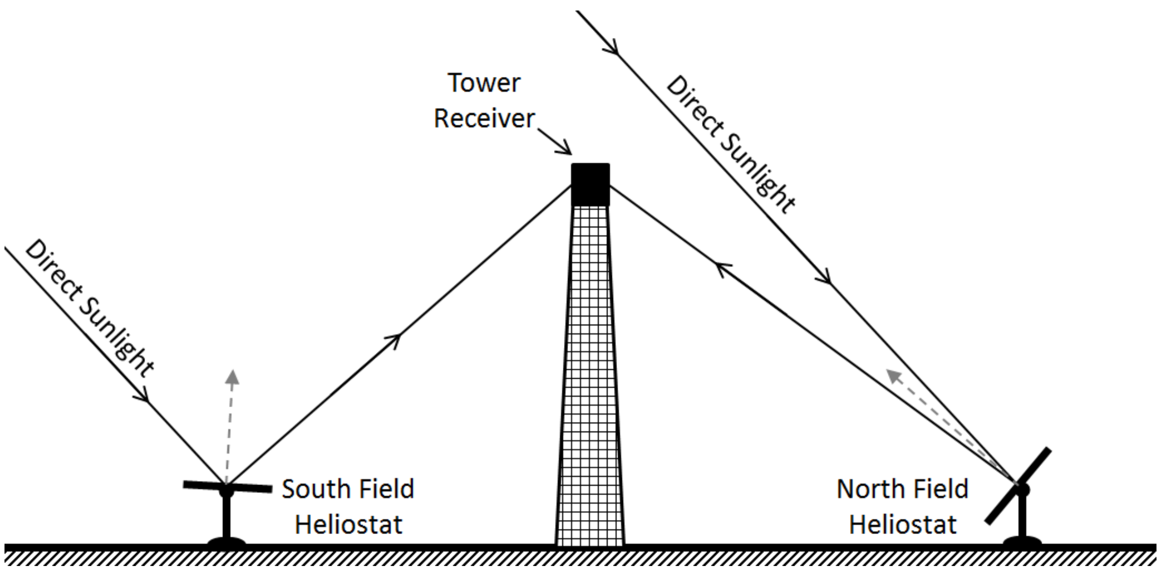


Figure 4.3: North and south field obliquity loss comparison.

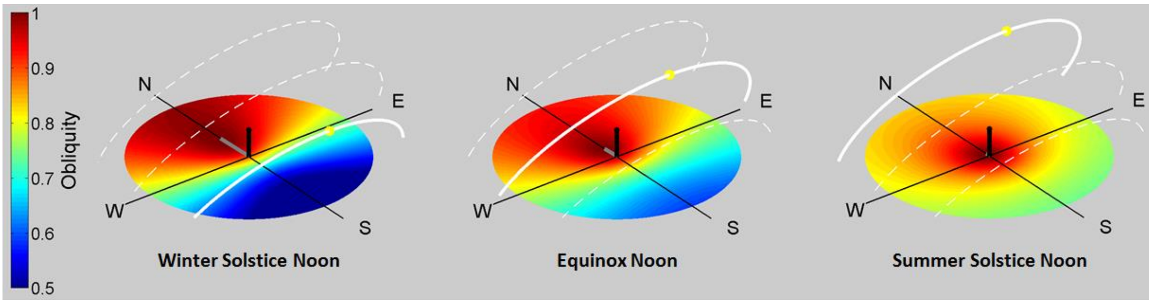


Figure 4.4: Obliquity factors for a circular field at noon on the winter solstice, equinox, and summer solstice. Red (unity) is loss-free.

The obliquity factor is depicted quantitatively for an 800 m diameter field and 100 m tall tower in Figure 4.4. The three illumination conditions are the best case (noon) for the winter solstice, equinox, and summer solstice.

Tower height, solar field layout, heliostat packing density, receiver concentration, and field efficiency are all interrelated. In general, measures to increase concentration, such as adding rows of heliostats at the edge of the field, tend to decrease field efficiency. In the northern hemisphere, heliostats far to the south of the tower are never operating efficiently. In the absolutely ideal case, each heliostat mirror is a segment of an off-axis parabola and forms a solar image on the receiver. The size of the solar image is a function of the distance from heliostat to tower. In practice, heliostat reflectors are slightly concave or are composed of many smaller, nearly flat reflectors, which are individually ‘canted’ to approximate the ideal shape. The initial canting is often set for a median case, such as the equinox noon.

The size of the receiver is driven by the distance and optical quality of the farthest heliostat. Figure 4.5 shows that outer heliostats form a larger solar image than inner-field heliostats. Light reflected by heliostats that does not reach the receiver is considered spillage (Figure 4.6) and should be minimized. Irradiance on the receiver varies throughout the day and over the year. Advanced wrap-around receivers take advantage of, and design for, illumination non-uniformities by channeling the heat transfer fluid (HTF) through pre-heating and super-heating segments.

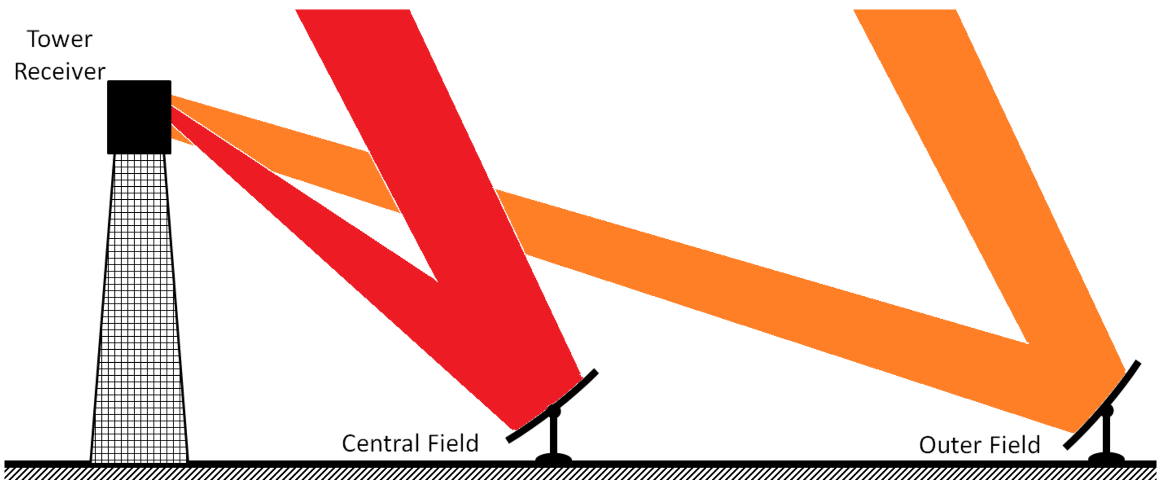


Figure 4.5: Inner and outer field solar image comparison.

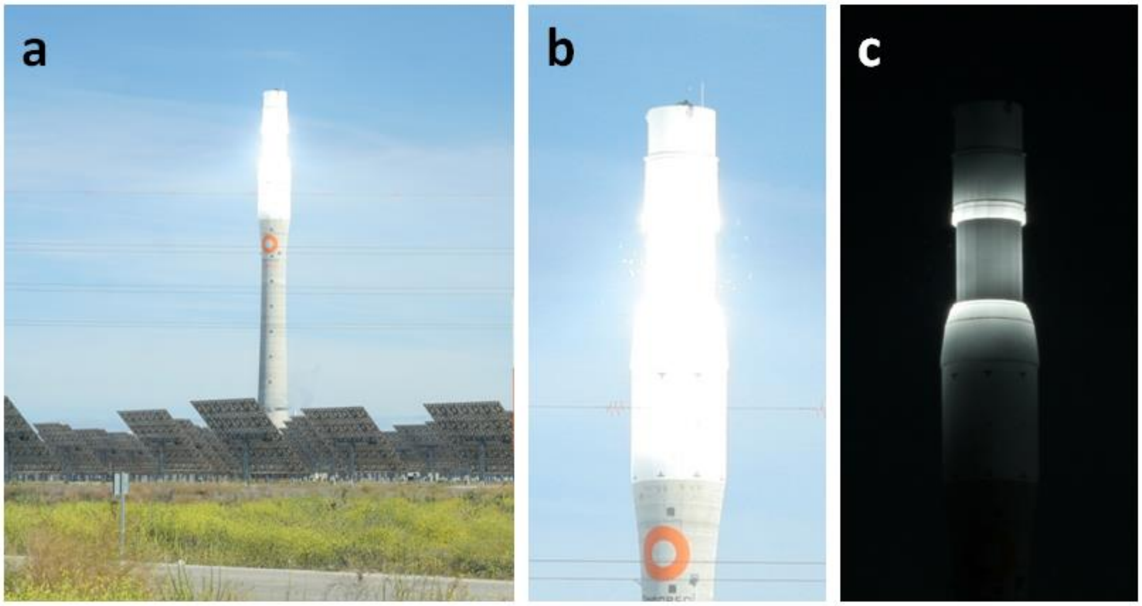


Figure 4.6: a) Gemasolar plant (Sevilla, Spain). b) Illuminated receiver. c) Stopped-down photo of receiver showing spillage. Photos courtesy of Blake Coughenour.

A major disadvantage of very large solar fields is the low heliostat packing density near the edges of the field, as seen in aerial photographs in Figure 4.7. Low areal density is required to avoid blocking losses. Increasing the areal density of the field causes the receiver to see a better-filled solid angle, increasing concentration, but this high density increases shadowing losses on the heliostats.

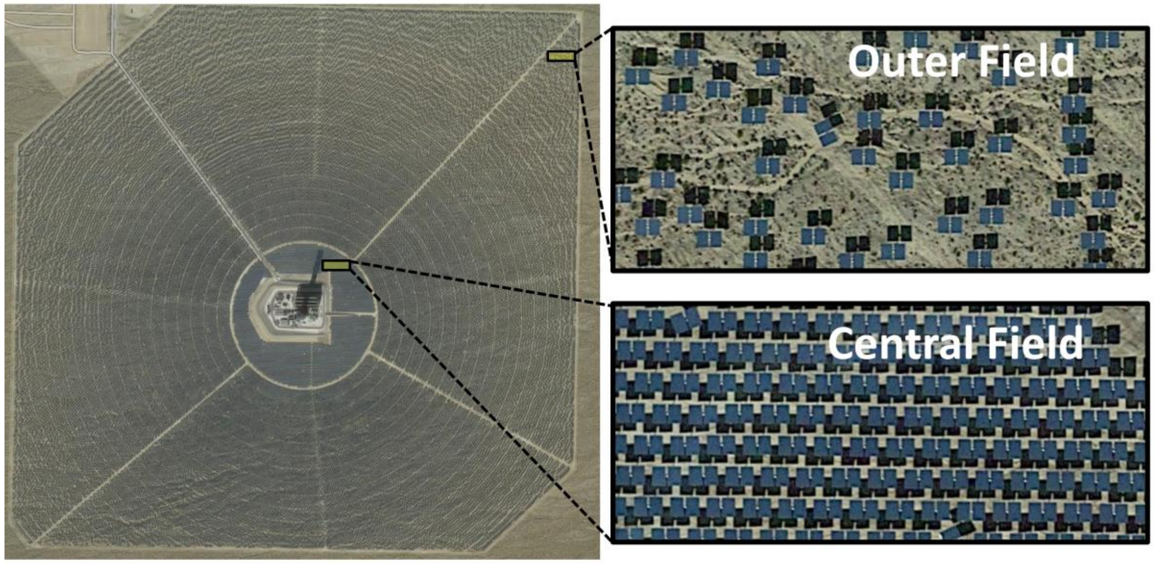


Figure 4.7: Heliostat packing density in central and outer field sites of Ivanpah Generating Station (Google, 2015).

### 4.2 ROTATING "AMPHITHEATER TRACKER"

This section details a new approach to the solar field for driving high efficiency 1 $MW_{thermal}$-scale cavity receivers. It combines the high collection efficiency of dish systems with the operational advantages of a central receiver. In this approach, a tower-mounted cavity receiver rotates to face an array of mirrors tessellated over an approximately conical surface, Figure 4.8. Solar tracking is accomplished through two motions: 1) azimuthal rotation of the mirror array on a circular track about the central tower and 2) articulation of the individual mirror segments. The opposite (Sun-side) end of the track can incorporate flat panel PV to boost daytime generation.

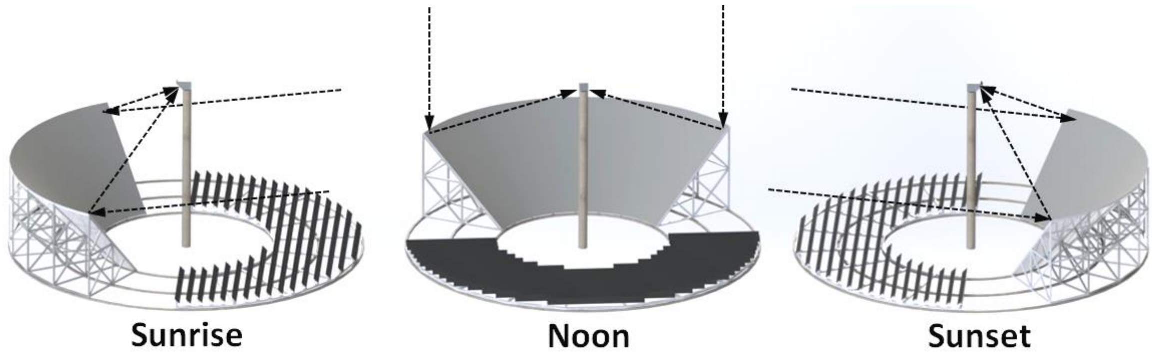


Figure 4.8: Rotation of a mirror array about the central receiver.

The most closely related prior art is CTAER's Variable Geometry Solar Test Facility in Sevilla, Spain (Figure 4.9). By rotating the field and receiver, the system achieves very high collection efficiency (Ruiz Hernandez, 2014). However, each heliostat requires its own bogie, pedestal, and azimuth/elevation drive. Each heliostat thus has three full degrees of tracking freedom: azimuthal rotation about the circular track and two tracking axis at the top of each pedestal.

Figure 4.9: CTAER's Variable Geometry Solar Test Facility (CTAER, 2012).

In our new approach, Figure 4.10, each mirror element is approximately the same distance from the receiver and maintains the same position relative to the receiver aperture. The mirror array and cavity receiver rotate together according to the solar azimuth angle. This leaves the individual mirror trackers to compensate for the solar elevation only. The solar elevation ranges from 0° (sunrise/sunset) to the summer solstice noon where the solar elevation varies by latitude $\varphi$ according to $90°-(\varphi-23.5°)$. In Tucson, AZ the maximum solar elevation is 81.3°. The required segment articulation is very mild, since the mirrors need only split the difference between the solar vector and vector to the tower. This small angular range is readily accomplished with low cost, small-stroke linear actuators.

For convenience of assembly, the amphitheater structure is ideally composed of four large raised panels, each interconnected and suspended by cables from the central tower.

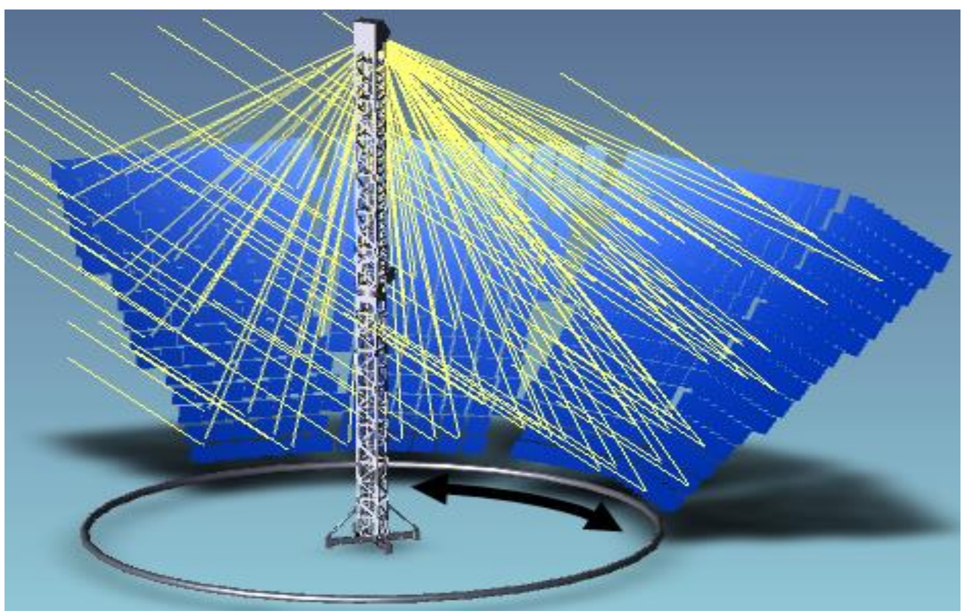

Figure 4.10: 4-Pannel mirror array with 552 individually-articulated mirror elements.

The four-panel collector in this concept has mirror area of $1460m^2$, with 20m high panels subtending 120° about the central receiver. Near the center of the mirror array (in the shadow of the tower), the segment articulation is strictly about a horizontal axis (pure elevation). Segments to either side require a tracking profile accomplished perfectly with one unique axis, but this axis is *not orthogonal to the mirror normal*. This unique axis is found by taking any three normal vectors on the mirror tracking profile and finding the plane defined by their intersections with the unit sphere. The plane's normal is the unique tilted tracking axis. Rotation about this axis causes the normal vector to sweep out a cone during operation. The deviation of this axis from the mirror segment plane is plotted in Figure 4.11, left. 0° means that the segment is tracked about a conventional elevation axis (cone with 180° apex angle). 90° would be the other extreme, where the segment is clocked without changing the normal vector (cone with 0° apex angle). In the upper array corners, this axis is tilted nearly 40° from the mirror face (or over 50° from the normal vector). Figure 4.11, right, shows oversized mirror segments with their required tracking axes (see https://youtu.be/tM3uFVbfksE). This tracking scheme is summarized in Table 4.1, below.

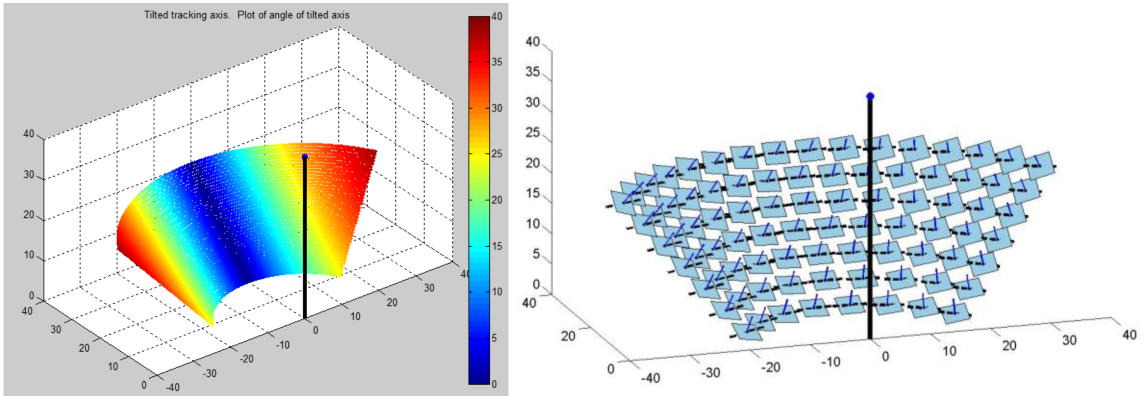


Figure 4.11: Angle between mirror vertex and unique, tilted tracking axis (left). Visualization of over-sized mirror segments with normal vectors and tilted tracking axes. (see https://youtu.be/tM3uFVbfksE).

Table 4.1: Tracking Case 1. Segment tracking about unique, tilted axis.

| | |
|---|---|
| Tower Height | 40 m |
| Inner Support Radius (ground level) | 20 m |
| Outer Support Radius (20m high) | 40 m |
| Angular spread of field | 120º |
| Bulk Array Tracking | Azimuthal rotation of array, centered on tower |
| Mirror Segment Tracking | Single-axis *not* orthogonal to normal vector. Deviation shown in Figure 4.11, left. Tracking range: +/-22.5° maximum. |

One disadvantage of the tracking scheme above is that errors in initial alignment transfer directly into operational misalignment. If the unique tracking axis of a given segment is not correctly aligned during installation, that segment is bound to a permanent offset tracking profile. Compensation with the azimuth drive is impossible, since it would misalign all other segments. This constraint is not the norm in tracking devices. For example, pedestal-mounted altitude/azimuth trackers may be installed with low precision and may settle over time in soft soil as long as the final system is under closed-loop control.

Let us consider an alternative decomposition of the segment tracking. Instead of tracking each segment about its own unique, tilted axis, we will track each segment about a more convenient axis orthogonal to the normal and correct for the residual error with a second tracking axis. The first tracking axis for each segment is found by taking the cross product of the heliostat pointing vectors for the minimum and maximum solar elevation (0° to 82° in Tucson). When tracked about this axis, pointing is error-free at these two extremes. The maximum residual error from this tracking, experienced somewhere mid-stroke, is the required secondary tracking range. In the shadow of the tower, this range is 0, meaning that only elevation tracking is required. To either side, the total residual, or secondary, tracking range increases up to ~4° maximum, or +/-2°, as shown in Figure 4.12. This tracking condition is summarized in Table 4.2.

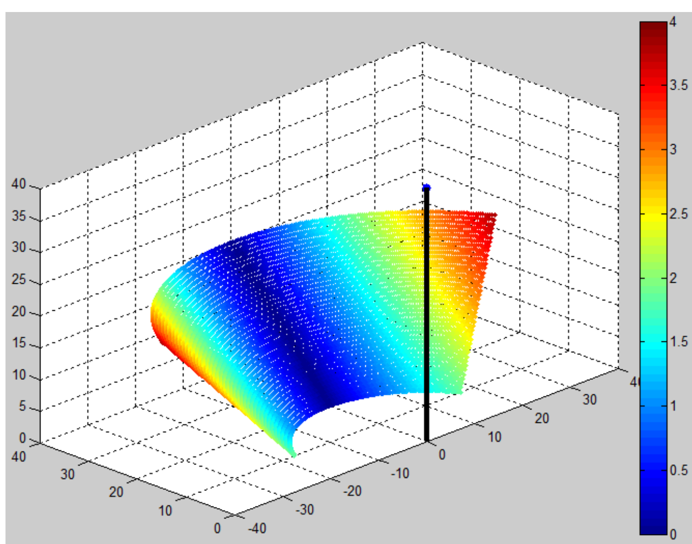


Figure 4.12: Residual tracking error for Tracking Case 2.

Table 4.2: Tracking Case 2. Segment tracking about non-tilted axis.

| | |
|---|---|
| Tower Height | 40 m |
| Inner Support Radius (ground level) | 20 m |
| Outer Support Radius (20m high) | 40 m |
| Angular spread of field | 120º |
| Bulk Array Tracking | Azimuthal rotation of array, centered on tower |
| Mirror Segment Primary Tracking | Single-axis orthogonal to normal vector. Not necessarily horizontal. Range: +/-22.5° max. |
| Mirror Segment Residual Tracking | Single-axis orthogonal to mirror vertex and primary tracking axis. Range: +/-2° max. Residual range is plotted in Figure 4.12. |

Although this tracking case requires a total of three degrees of tracking, it enjoys significant operational advantages. The initial alignment may be very coarse and both segment-tracking axes are very small range. In particular, the secondary (residual) tracking axis requires only +/-2° range in the extreme case. In one implementation, a linear actuator could drive a bracket about the primary axis (+/-22.5° max) while a single, small-stroke actuator performs secondary tracking between the bracket and a four-pad mirror support frame.

One risk associated with a tall (20 m) structure is wind loading. Most of the structural mass in heliostats is owed to wind survival, not gravity deflection. Heliostats must survive (to some actuarial probability) the maximum expected wind condition. In existing heliostat fields, the heliostats are moved to a zenith pointing stow position during high winds. Our four-panel amphitheater concept is also conducive wind stowing, as shown in Figure 4.13. During normal operation, cables from the central tower suspend four interlocking panels. During high wind, the panels unhitch and are lowered to the ground. The lowered state is also well suited for initial assembly, washing, and maintenance. Equipping the heliostat segments with full range of motion would allow continued operation in the lowered state, albeit with much lower optical efficiency. However, the cost to extend the segment range of motion is probably not worth the occasional operational benefit of tracking in the lowered state.

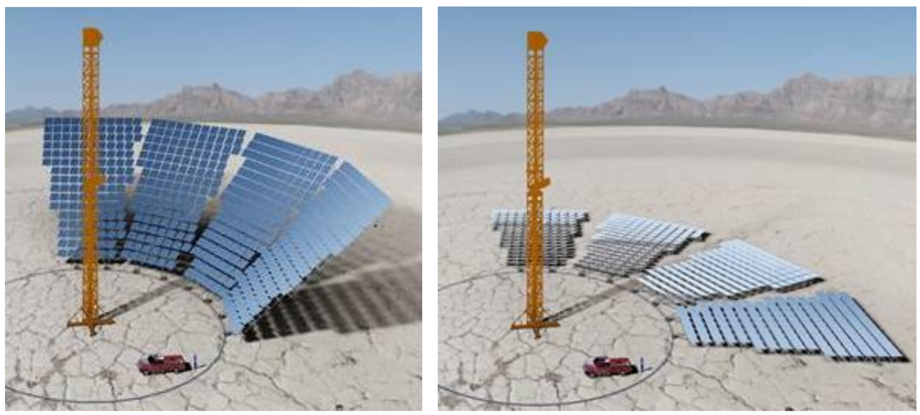

Figure 4.13: Four-pannel mirror array in operation (left) and stowed for high wind, maintenance, cleaning, or installation (right). Rendering courtesy of Justin Hyatt, M3 Engineering.

## 4.3 SIMULATED COLLECTION PERFORMANCE

The collector system described in Section 4.2 was simulated in a full non-sequential model in ZEMAX. All 552 square reflectors (1.65 m x 1.65 m), with 40 m focal length, were individually articulated according to the solar elevation angle with a ZPL macro. The reflectors were modeled with 3mrad RMS optical errors to account for tracking and reflector slope errors. Obliquity losses, astigmatism, and reflector self-shadowing (Venetian blinds effect) all vary according to solar elevation. Figure 4.14 and Table 4.3 show ray-tracing simulations for 30° solar elevation.

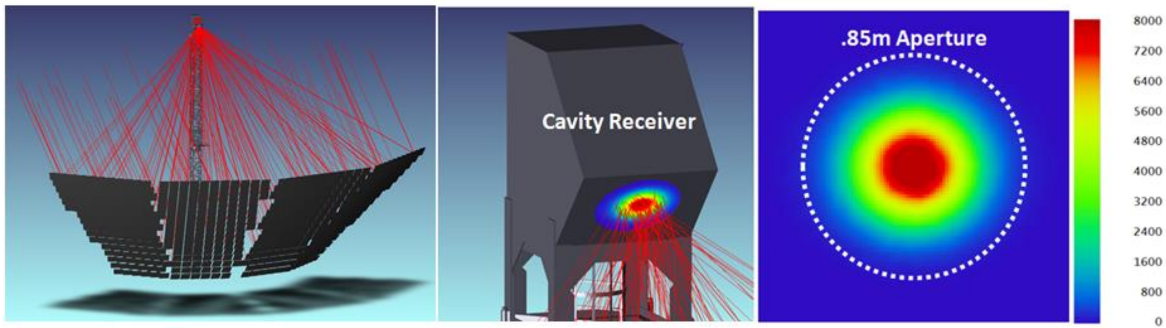


Figure 4.14: Ray tracing results of 552-reflector array illuminated at 30° solar elevation.

Table 4.3: Simulation parameters (italics) and results (bold).

| | |
|---|---|
| *Number of Mirrors* | *552* |
| *Mirror Area* | *1458 $m^2$* |
| *Solar Disk* | *+/-4.6 mrad* |
| *Mirror/Tracking Ray Errors* | *3.0mrad RMS* |
| *Reflectivity and Soiling Factors* | *89.0%* |
| *Cavity Aperture (diameter)* | *850 mm* |
| **Field Optical Efficiency (30° elevation)** | **90.9%** |
| **Spillage** | **1.5%** |
| **Average Aperture Concentration** | **2050X** |

The field optical efficiency is a function of two loss mechanisms: obliquity and self-shadowing. Self-shadowing can be avoided completely with low packing density, but this becomes structurally inefficient. Our 552 mirror segments, totaling 1458 $m^2$, approximately tessellate a cone of area 1777 $m^2$. This 82% packing density is quite high, but still gives very low self-shadowing for this geometry. The most marked gains over a traditional field are in obliquity factor. Previously, Figure 4.4 showed the obliquity problem for traditional fields. Figure 4.15 directly compares our rotating field with a fixed circular field under the same solar illumination.

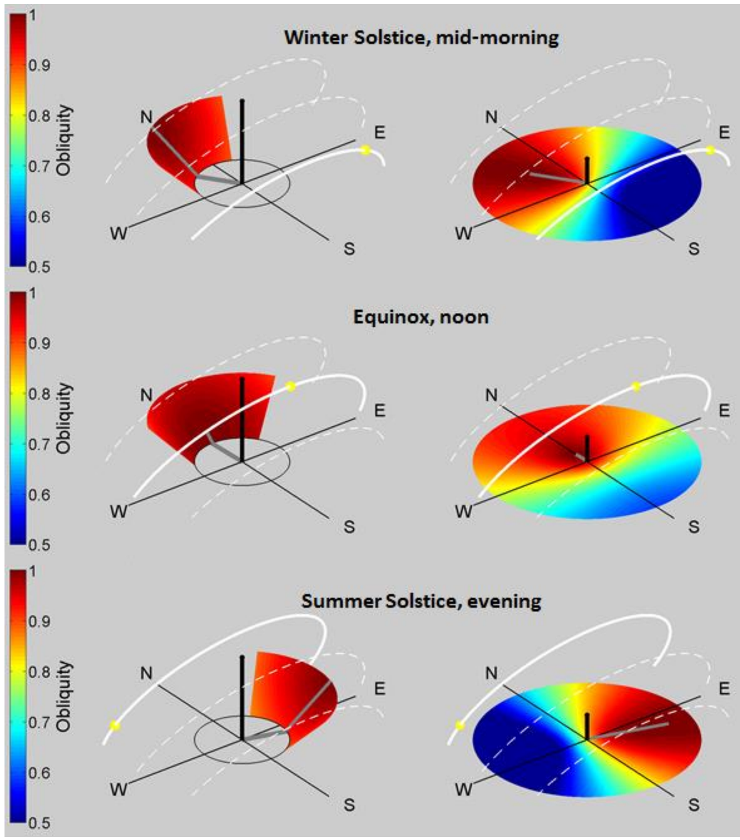


Figure 4.15: Obliquity factor comparison: rotating field (left) vs. fixed field (right).

Figure 4.15 compares the obliquity for three tracking cases: mid-morning on the winter solstice, noon on the equinox, and evening on the summer solstice (all-day tracking shown in https://youtu.be/6R5A85ihAag). The Sun is represented with a yellow sphere located at the projection of the solar vector on a unit sphere centered at the base of the tower.

Since the solar elevation varies continuously, field efficiency performance should be weighted according to the integrated solar flux at each elevation angle. This weighting was calculated using the Simplified Clear Sky Model, which estimates the DNI at any moment based on solar position and atmospheric conditions (Bird, 1981). The field efficiency was then computed as a function of solar elevation by a ray-tracing macro. All self-shadowing, blockage, ray error, and obliquity losses are fully modeled in the simulation. Figure 4.16, below, plots the normalized annually integrated flux collected at each elevation angle (red line) and the field optical efficiency (blue line) both as a function of elevation angle. The prominent peak at 34.3° corresponds to the solar elevation at noon on the winter solstice in Tucson, AZ: 90°-32.2°-23.5°=34.3°. Around this time, the solar elevation changes very slowly mid-day and persists in nearly the same path for several days before and after the solstice. On the summer solstice, the elevation sweeps from 0° (sunrise) to 81.3° (noon) very quickly, so the integrated flux is spread out over a large elevation range.

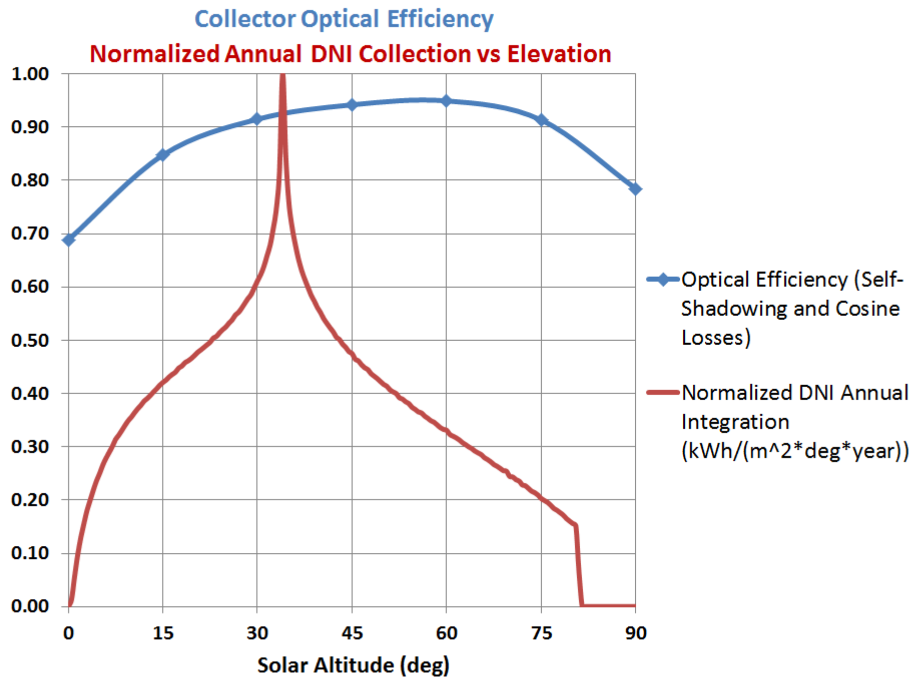


Figure 4.16: Optical efficiency (blue) and annual insolation (red) vs. solar insolation.

After convolving the weighted field optical efficiency (obliquity loss and shadowing), reflectivity/soiling, and spillage, the final annually averaged field collection efficiency is 79%. This is a vast improvement over traditional heliostat fields with ~60% efficiency (Collado, 2008) (Falcone, 1986). Assuming a high receiver efficiency of 90% (possible with cavity receivers only), this gives a final collection efficiency (thermal power collected)/(solar irradiance*total aperture) of 71%.

The >2000X concentration anticipated in this system is achieved with the very high field efficiency discussed above and the large solid angle subtended by the field when viewed from the tower. Figure 4.17, below, includes frames from a full video (https://youtu.be/3wCFJK0FIQk) showing solar tracking from horizon to zenith from multiple perspectives.

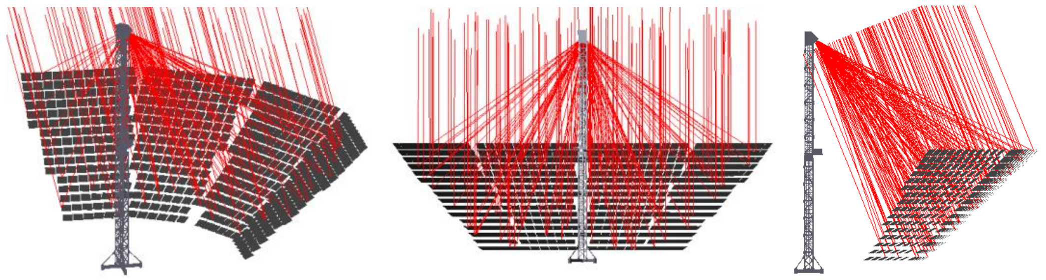

Figure 4.17: Ray tracing simulations from various perspectives.

This approach is predicated on the availability of high-temperature 1 $MW_{thermal}$-scale thermal receivers and power blocks. As a first implementation, this new architecture with could drive conventional steam turbines (250 kW). When combined with thermal storage and daytime PV on the sun-side of the circular track, the system could deliver 250kW 24 hours a day in remote sites (assuming clear skies). Later, units manufactured economically in high volume would be used in very efficient utility-scale plants, where heat from multiple central receiver units would be taken to a large heat storage tank and turbine generator.

The University of Arizona and teaming partners M3 Engineering and Sandia National Labs have proposed construction of a single-panel prototype collector with a photometric screen acting as receiver (Figure 4.18). Future work should investigate low cost closed-loop tracking control systems. Ideally, closed-loop control could be implemented without encoders on each mirror (Hines & Johnson, 2012).

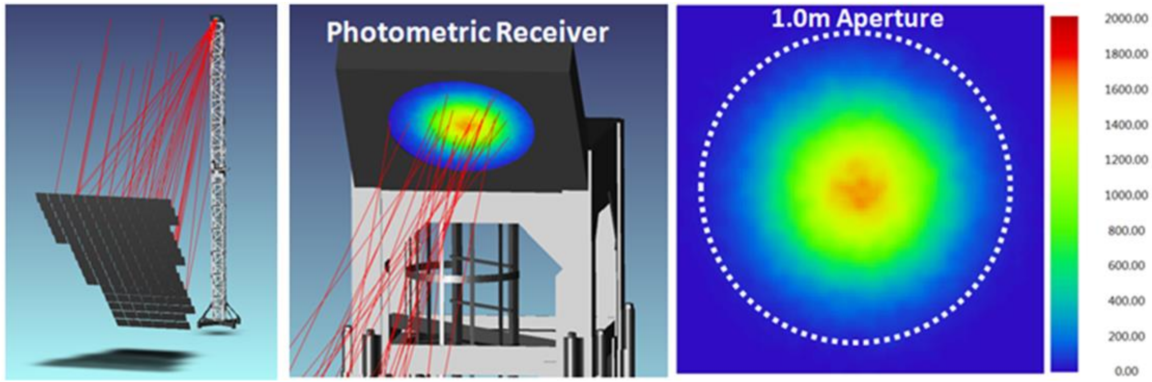


Figure 4.18: Single-panel proof-of-concept with photometric screen receiver.

# CHAPTER 5: HYBRID PHOTOVOLTAIC/THERMAL TROUGH

In this chapter, silicon PV cells are added to a conventional CSP trough reflector with a spectrum-splitting film. This approach is one of several tandem converter embodiments described by (Yu, Fisher, Wheelwright, Angel, & Holman, 2015).

The primary grid-level advantage of CSP with storage is dispatchability (see Section 1.5). A major disadvantage is low efficiency compared to PV and CPV technologies. The very best CSP plants have sunlight-to-electricity conversion efficiency <15% of the total solar resource or <20% of direct sunlight.

CSP trough collectors focus direct sunlight onto vacuum-insulated absorbing pipes, which convey heated oil to a thermal block. Since thermal receivers maintain high absorptivity up to 2 μm, CSP plant efficiency is largely wavelength-agnostic. Some plants run the oil through a heat exchanger with molten salt, a thermal storage medium (see Figure 1.10). The conversion losses for a typical CSP trough plant with storage are shown in Figure 5.1, based on typical losses assumed in (ARPA-E, 2014). Note that out of the 8 kWh/m$^2$/day average annual solar resource for Phoenix, AZ, a quarter is diffuse, which is immediately lost as it is not concentrated onto the thermal pipe. Additional optical and thermal losses in the field and conversion losses in the power block result in an end efficiency of 13%. In this example, the ratio of variable to dispatchable output allows for ten hours of operation after sunset.

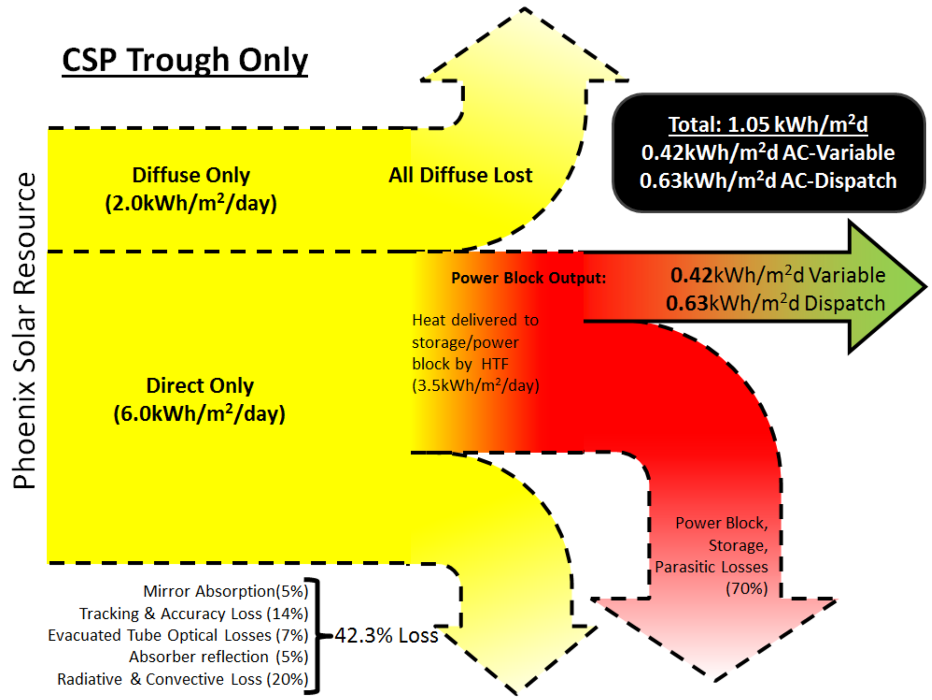


Figure 5.1: CSP trough plant losses.

High quality Si-PV modules convert both direct and diffuse sunlight with >20% efficiency. Figure 5.2 details the conversion losses by wavelength band. Visible (VIS, $\lambda$<700nm), near-infrared (NIR, 700nm<$\lambda$<1000nm), and infrared (IR, $\lambda$>1000nm) photons are converted according to the spectral response of the cells. Note that the majority of generated electricity comes from the NIR band. Since PV panels do not include storage, none of the generation is dispatchable.

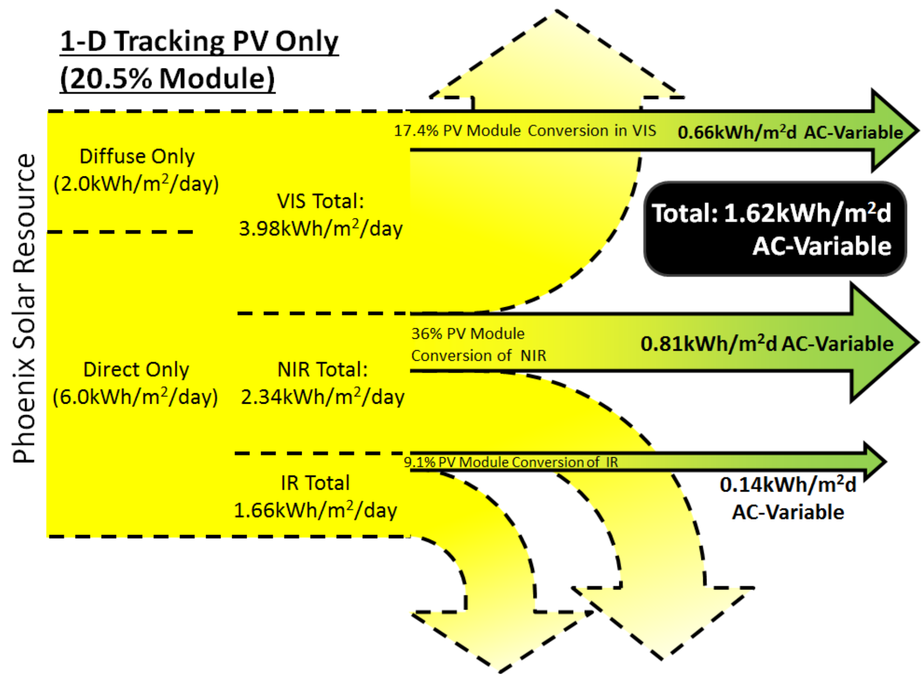


Figure 5.2: Si-PV conversion losses by wavelength band.

### 5.1 Spectrum-Splitting Hybrid PV/Thermal System (PVMirror)

A hybrid Si-PV/thermal system should direct most NIR sunlight to the Si cell and most VIS and IR light to the thermal receiver, per Figure 5.3. To maintain adequate dispatachability, the PV band was truncated to 700 nm<$\lambda_{PV}$<1100 nm, even though Si-PV performs better than CSP trough down to 500 nm.

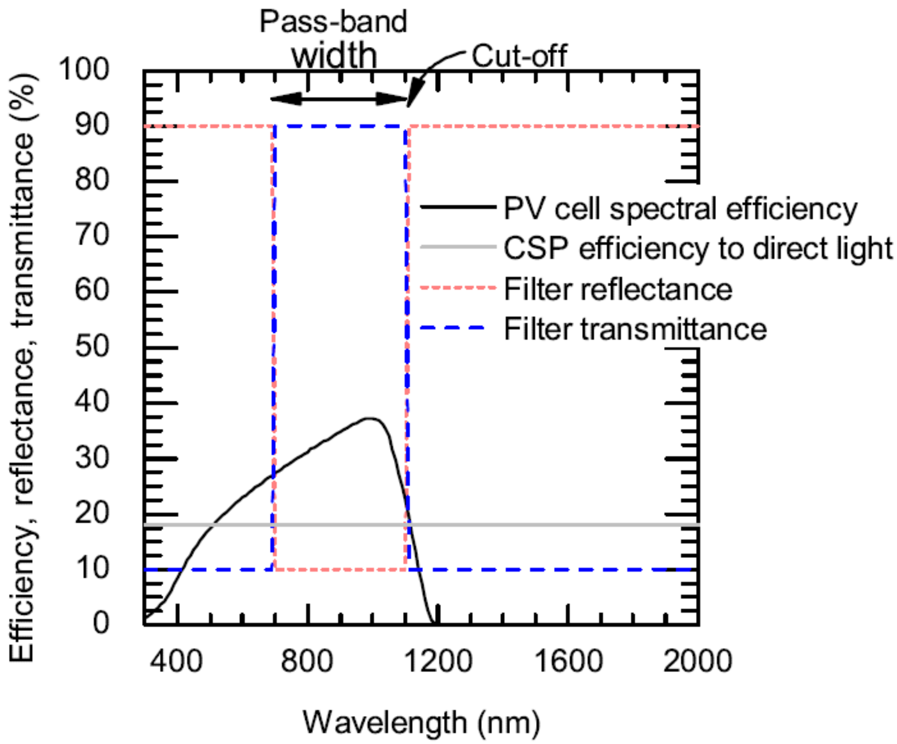


Figure 5.3: Sunlight to AC electricity conversion efficiency by wavelength for Si-PV (black line) and CSP trough (gray line). Dichroic filter band indicated with dashed lines. (Yu, Fisher, Wheelwright, Angel, & Holman, 2015).

In a conventional CSP trough plant, reflector segments are off-axis back-silvered glass mirrors. In our hybrid PV/thermal system, spectrum splitting is achieved by replacing the usual protected silver coating with a dichroic mirror. Behind the dichroic, Si heterojunction cells are conformally laminated to the convex side of the curved trough surface, as shown in Figure 5.4. This combination of dichroic film and PV cells is nicknamed ‘PVMirror.’

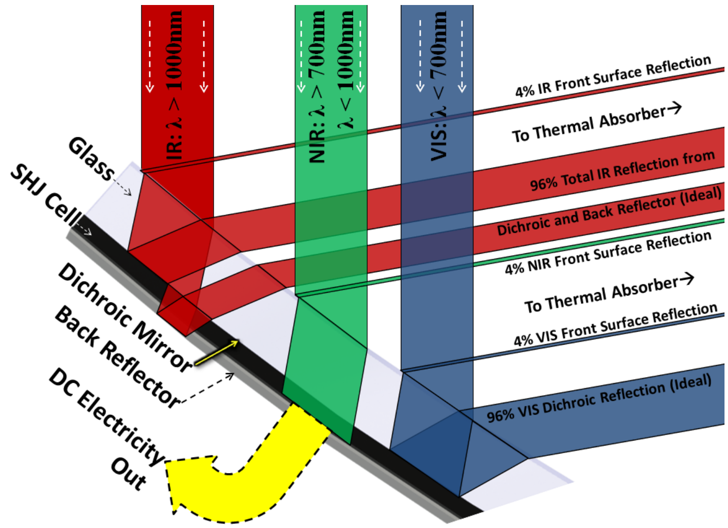


Figure 5.4: Detail view of spectral response of glass trough with conformally laminated dichroic film and Si heterojunction cell.

In the visible spectrum, the PVMirror looks like a normal mirror (Figure 5.5, top), reflecting most direct visible light to the thermal receiver. In the NIR, the PVMirror looks and behaves like a curved PV module. Since the PV cells collect over full area, they can capture NIR diffuse radiation.

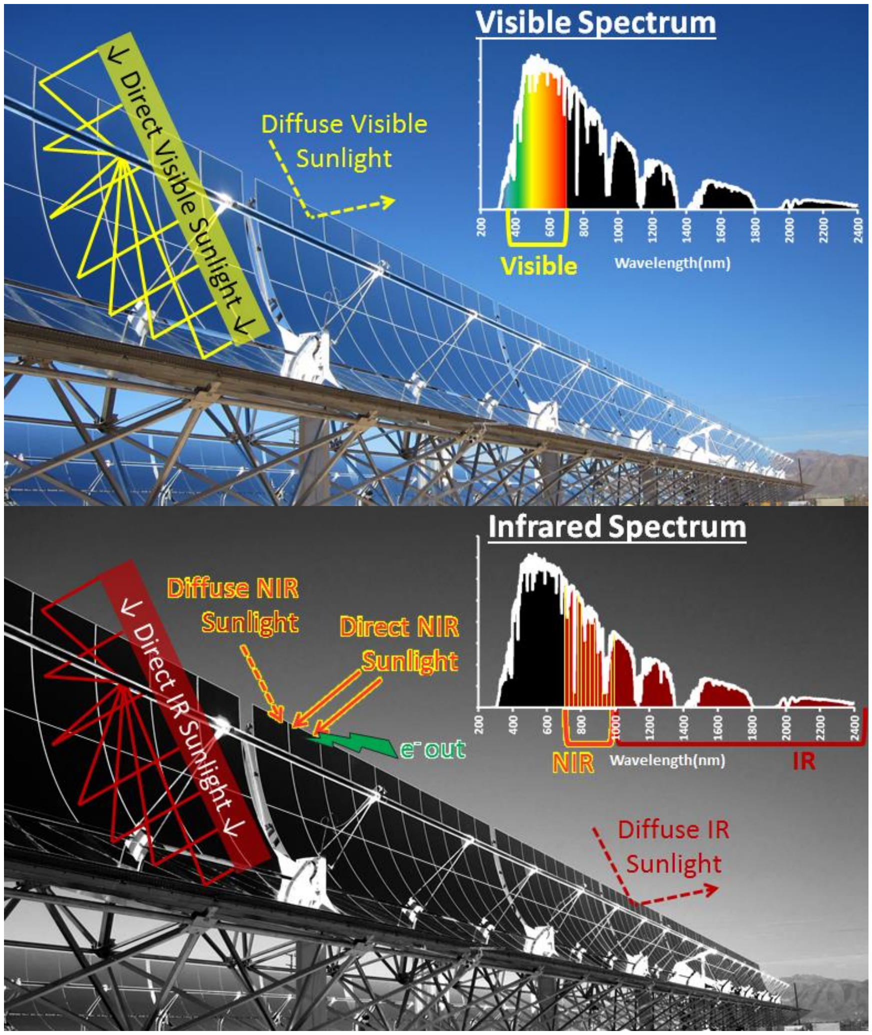


Figure 5.5: PVMirror in the visible spectrum (top) and NIR-IR spectrum (bottom). Background image adapted from (Gossamer Space Frames, 2012).

With the Si-PV providing high conversion efficiency in the NIR, the PVMirror out-performs a pure CSP trough plant in total output and out-performs a PV-only field by providing high-value dispatchable power (Figure 5.6). Two storage ratios are shown in

Figure 5.6. The latter maintains the same dispatchable level as a conventional CSP plant (Figure 5.1) but nearly doubles daytime (variable) output.

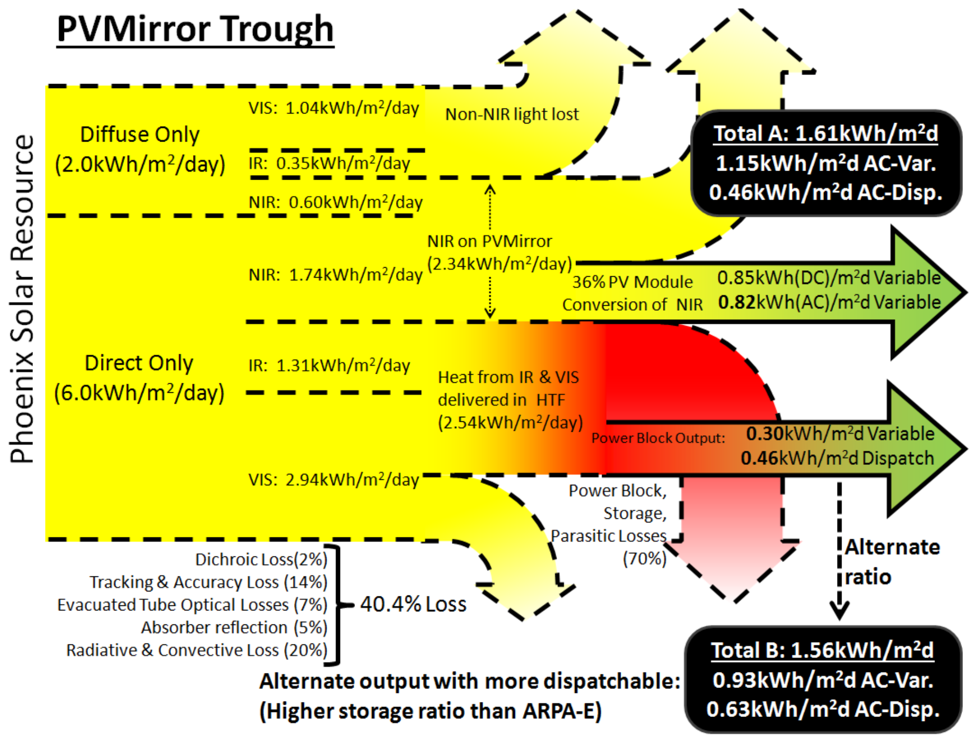


Figure 5.6: PVMirror loss mechanisms by wavelength range.

### 5.2 Dichroic Mirror

In an ARPA-E funded project ("PV Mirror: A Solar Concentrator Mirror Incorporating PV Cells" #DE-AR000474), Arizona State University and The University of Arizona are investigating technical approaches and economic tradeoffs to implement the PVMirror in CSP troughs. The most critical system component is the dichroic mirror. This dichroic may be deposited on the glass, deposited on individual PV cells, or laminated as a separate film between the glass and cells.

CSP troughs are tracked about a horizontal north-south oriented axis. This gives a solar incidence *along the trough vertex* limited by Equations 2.1 and 2.1. However, since troughs are curved, the incidence angle increases away from the vertex. Figure 5.7 shows this range as a function of solar skew angle and distance from the vertex. Note that along the trough vertex, the solar skew and incidence angle are identical. Even when the trough is illuminated at zero skew, the incidence angle varies from 0° at the vertex to >40° at the trough rim. As the skew angle increases, the incidence angle increases over the whole trough, but the *range* of incidence angles decreases.

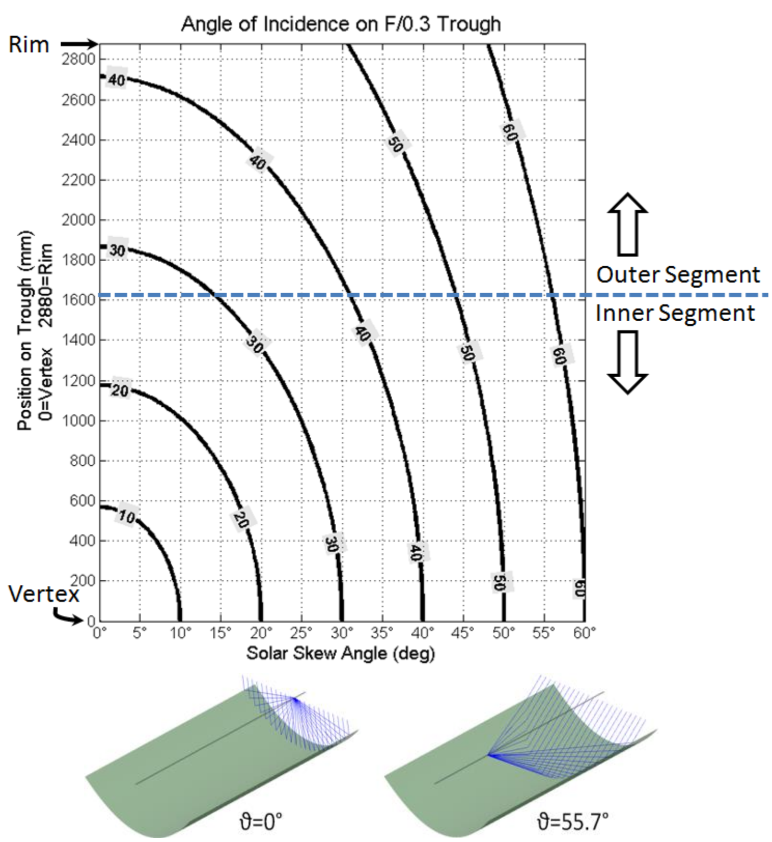


Figure 5.7: Top: incidence angle contours as a function of solar skew angle and distance from the vertex. Bottom: 0° and 55.7° skew cases.

Coatings have a tendency to blue shift as the incidence angle increases. This effect is clear in Figure 5.7, which plots the modeled (ideal) transmission of a 48-layer coating as a function of wavelength and external incidence angle (in air). The $TiO_2/SiO_2$ stack provides a highly discriminating band-pass window from 700-1000 nm. Note that as the angle of incidence increases, the band shifts to lower wavelengths blue shift). This performance was modeled in Macleod Essential (Thin Film Center Inc, 2014).

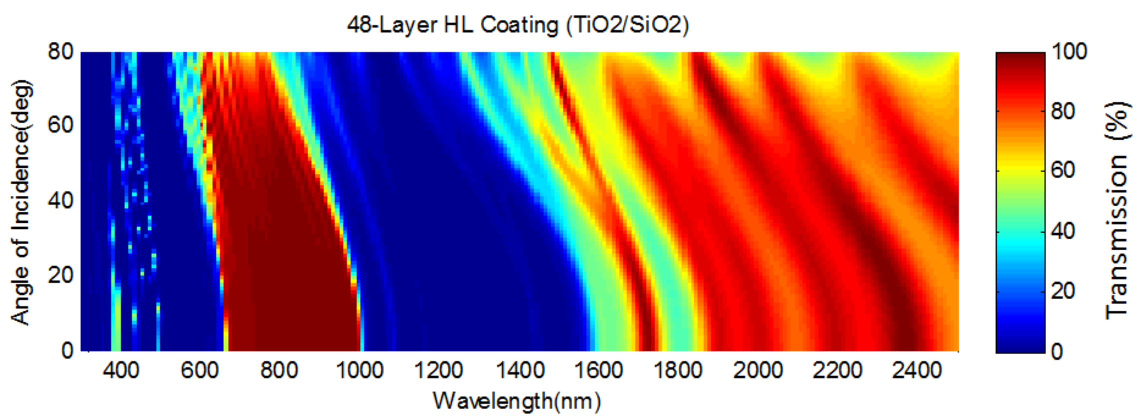


Figure 5.8: Modeled performance of a 48-layer bandpass filter ($TiO_2/SiO_2$).

In our hybrid converter, coating performance is more critical in the IR than the VIS. If a visible photon is transmitted, the PV cell utilizes it, albeit with higher thermalization than NIR photons. The PV cell, however, cannot use transmitted IR photons. Around 1600 nm the dichroic shown in Figure 5.8 begins to lose performance. However, the spectral intensity of sunlight beyond 1600 nm drops off quickly, as shown in Figure 5.9. The loss of coating performance beyond 1600 nm does not significantly impact the overall spectrum splitting between the thermal and PV receivers.

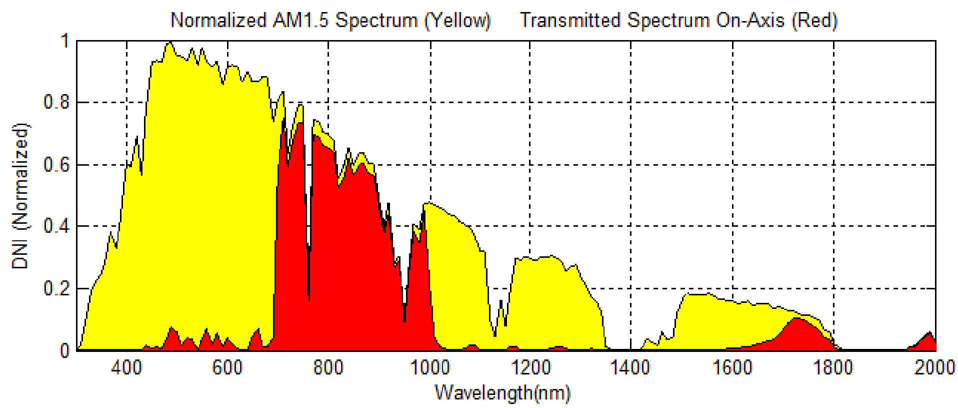


Figure 5.9: Normalized on-axis performance of 48-layer dichroic scaled to the AM1.5 spectrum. Red is transmitted sunlight.

We originally anticipated large-scale coating deposition in vacuum on either the curved glass or chemically polished Silicon heterojunction cells. Large-area glass coating has a heritage in the low-E window industry. However, deposition of a more complicated coating (such as that modeled in Figure 5.8) on curved glass is sure to increase costs. Deposition directly on the PV cells poses a separate problem: the cell surface must be specular. For light-trapping purposes, PV cells are usually textured. Arizona State University has developed a chemical polishing process for diamond-cut Si wafers which gives specular reflections in one dimension (Yu, Wheelwright, Angel, & Holman, 2015). Although this wafer process is promising, the lowest-cost dichroic is likely to be a separate film laminated between cells (polished or not) and the glass.

Working with 3M, the UA/ASU team is currently planning to incorporate a multi-layer polymeric film with a target spectral passband from 700-1100 nm. Figure 5.10

shows the coating performance achieved by 3M in two different batches. The first has more uniform performance across the film. The second is less homogenous, but more on average comes closer to the target window.

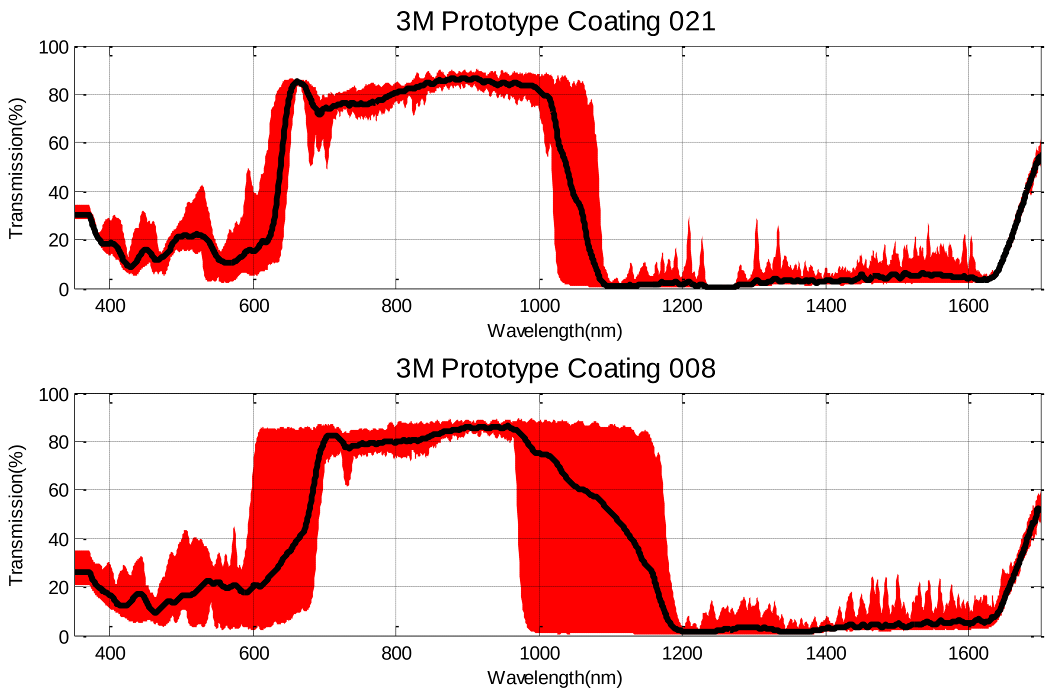


Figure 5.10: Prototype coating performance for two films. Average transmission (black line) and min/max range (red) from 25 measurements across film surface.

## 5.3 On-Sun Prototype Testing

As of this writing, our custom 3M bandpass film has not yet been laminated into a PVMirror module. Prior testing of PVMirrors with a long-pass 3M film is described below. Figure 5.11 shows a PVMirror with a film on the front surface (not internally laminated). When viewed at glancing incidence the film blue-shifts into the visible range, making the laminated PV cell visible.

Figure 5.11: Early PVMirror prototype making a line focus (left) and viewed at glancing incidence (left). Photos courtesy of Holman Lab (ASU).

On-sun PVMirror testing will proceed through three prototype scales, from 200 mm X 300 mm to 400 mm X 400 mm and finally a full trough segment. At this stage, 200 mm X 300 mm prototypes are being tested at the University of Arizona's Bear Down solar test area. A LabVIEW program reads temperature from a calorimeter mounted at the linear focus, controls the solar tracker, performs alternating IV sweeps on the PVMirror and a reference cell. The source meter used to perform the IV sweeps (Keithley 2460) has a single channel, so LabVIEW also controls a DPDT relay to switch between the two signals. The calorimeter is a blackened copper block that is heated and cooled in a cycle. Thermal power is calculated by analysis of the ramp rate during heating.

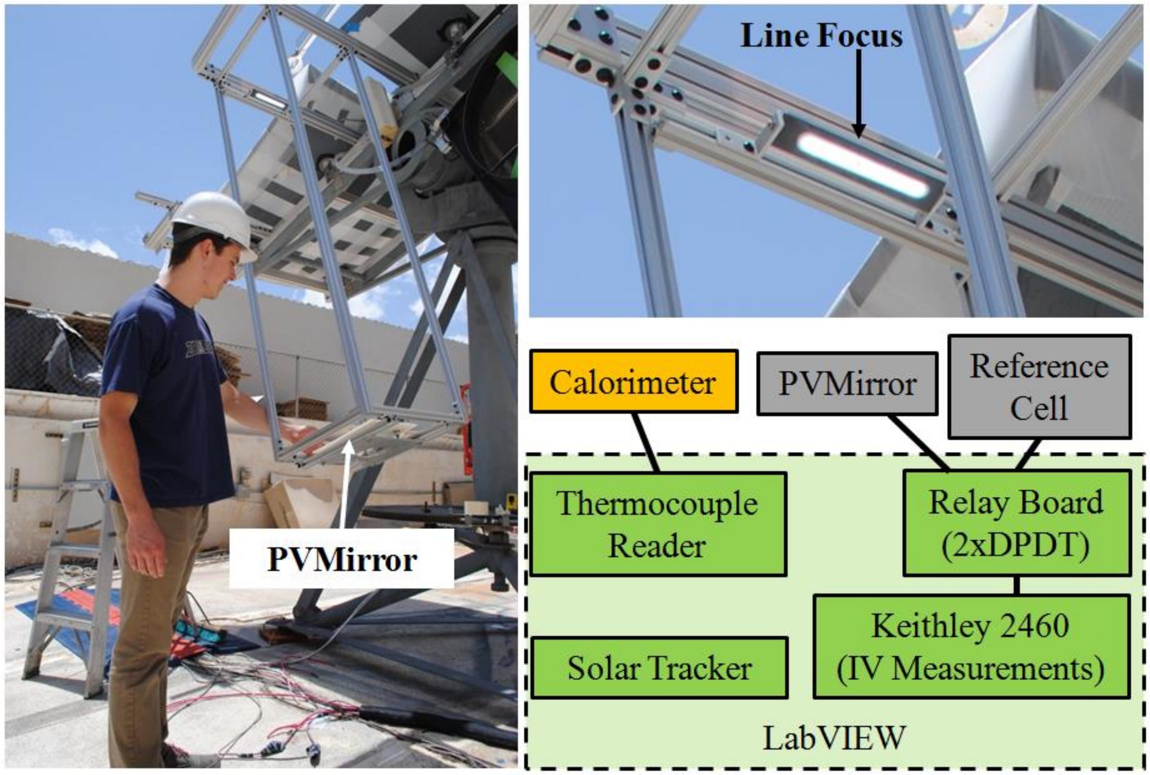


Figure 5.12: On-Sun testing of a PVMirror prototype.

The calibrated reference cell is used to calculate solar irradiance and system efficiency. As a backup, one-minute resolution solar intensity data is available from an NREL OASIS observation site located on The University of Arizona Campus (OASIS, 2015). Figure 5.13 compares OASIS observation data with the reference cell short-circuit current, $I_{sc}$, scaled according to nameplate calibration.

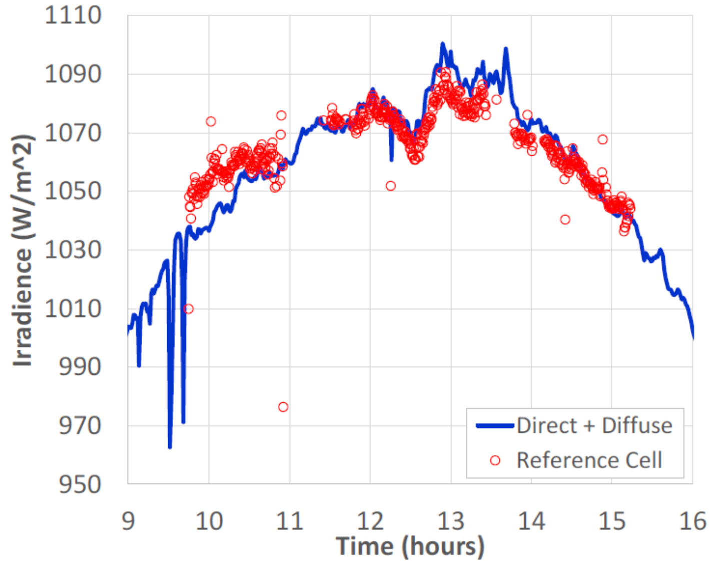


Figure 5.13: Reference cell scaled $I_{sc}$ and OASIS global irradiance.

Future work on this project includes lamination of the 3M film, optical testing of conformity between the glass and file, and on-sun testing of progressively larger prototypes.

# CONCLUSIONS AND OUTLOOK

As solar energy makes up a larger fraction of overall generation, the largest hurdle for *all* solar technologies will be the intermittency of the solar resource. In order to accommodate a significant (>5%) contribution from solar sources, proactive grid management and some form of storage is necessary. The optical solutions in Chapters 4 and 5 have the potential for thermal storage, which mitigates this problem by allowing nighttime generation. The CPV approaches in Chapter 2 & 3 do not have thermal storage potential and thus, like all conventional PV, will ultimately face diminishing value as daytime electricity becomes abundant (and cheap). The development of grid-scale batteries is at least as important to the future of the solar industry as the development of solar modules themselves.

A potential critique of the optical solutions described in this work is that they are too complicated to be economical. However, in many industries we find examples where early, prohibitively complex solutions eventually prevailed when properly engineered. For example, TFT LCD panels have enjoyed orders of magnitude of cost reduction while advancing performance in every metric. Technical solutions with *fundamentally* low cost are those which utilize Earth-abundant raw materials efficiently (and rare materials extremely efficiently) and have a path to large-scale production. In the solar industry, land is an additional resource to consider. Glass mirror-based solar concentrators, though more complex than flat PV modules, have the potential for very efficient land and material use.

Of the two CPV approaches described in Chapters 2 & 3, the author believes that the dish/lenslet approach has the best opportunity to leverage electrical, thermal, and manufacturing scaling benefits (Nielson, et al., 2012). A compact, lenslet-based dish-CPV receiver would feature a very small hermetic volume and a size/form-factor conducive to large-scale production. Both CPV approaches are only possible with trough and dish mirrors shaped to <1 mrad RMS slope error.

The trough, dish, and CSP systems in Chapters 2-4 make no use of diffuse light. The hybrid PV/thermal system in Chapter 5 only makes use of NIR diffuse light. As discussed in Section 1.4, this loss represents a serious handicap compared to traditional PV systems. Due in part to this loss of diffuse light, it is the author's opinion that CPV technologies will become most compelling to utilities serving high-DNI areas when production multi-junction cells reach 50% efficiency, which is expected in the 2020s (Figure 1.7). To broaden the market, CPV modules would also have to convert some diffuse light (ARPA-E, 2014). In the CSP and CPV industries, every opportunity to convert diffuse sunlight should be considered, as this has the dual benefit of increasing generation and broadening the potential market to medium-DNI sites.

Of all the technologies discussed in this dissertation, the PVMirror will be the most actively developed in the coming years. The UA/ASU team is early testing. The PVMirror boosts traditional CSP plants, converts some diffuse sunlight, and is fully compatible with current plant architectures, even allowing 'drop-in' capability in existing plants.

# APPENDIX A: SMARTS .INP PARAMETERS

Note that the $CO_2$ levels used in the ASTM_G173 standard (370 ppm) is no longer valid. For correct infrared transmission, use current $CO_2$ levels (402.8 ppm as of this writing).

| Description | Field inputs (use in .INP file) |
|---|---|
| Comments | 'USSA_AOD=0.084_ASTM_G173' |
| | 1 |
| Pressure(mb), Altitude(km), Height(km) | 1013.25 0 0 |
| | 1 |
| Reference Atmosphere (US Standard Atmosphere 1976) | 'USSA' |
| Water Vapor (Calculate from Reference) | 1 |
| Ozone (Calculate from Reference) | 1 |
| Gaseous Absorption(Calculate from Reference) | 1 |
| Carbon Dioxide(ppm) | 370 |
| Extraterrestrial Spectrum (Gueymard 2004) | 0 |
| Aerosol Model | 'S&F_RURAL' |
| | 0 |
| Turbidity (Aerosol optical depth at 500nm) | 0.084 |
| Albedo Card | 41 |
| | 1 |
| Tilt Albedo Card | 51 37. 180. |
| Spectral range (min, max, step in nm), Solar constant distance correction factor, solar constant(w/m2) | 280 4000 1.0 1366.1 |
| | 2 |
| Output sampling(min,max in nm) | 280 4000 .5 |
| | 2 |
| | 1 2 |
| | 1 |
| Circumsolar Card (Slope, aperture, limit) | 0 2.9 0 |
| Smoothing Filter (Bypass) | 0 |
| Illuminance (Bypass) | 0 |
| UV (Bypass) | 0 |
| Geometry (Use Air Mass) | 2 |
| Solar Geometry Card (Air Mass) | 1.5 |

## APPENDIX B: ROLL FORMING TOROIDAL LENSES

A prototype roll-forming machine with 316 stainless steel rollers was built to fabricate toroidal lens arrays in plastics (Figure A.1). The lenticulated roller was used in a furnace to slump-mold B270 glass lenses (Figure A.2).

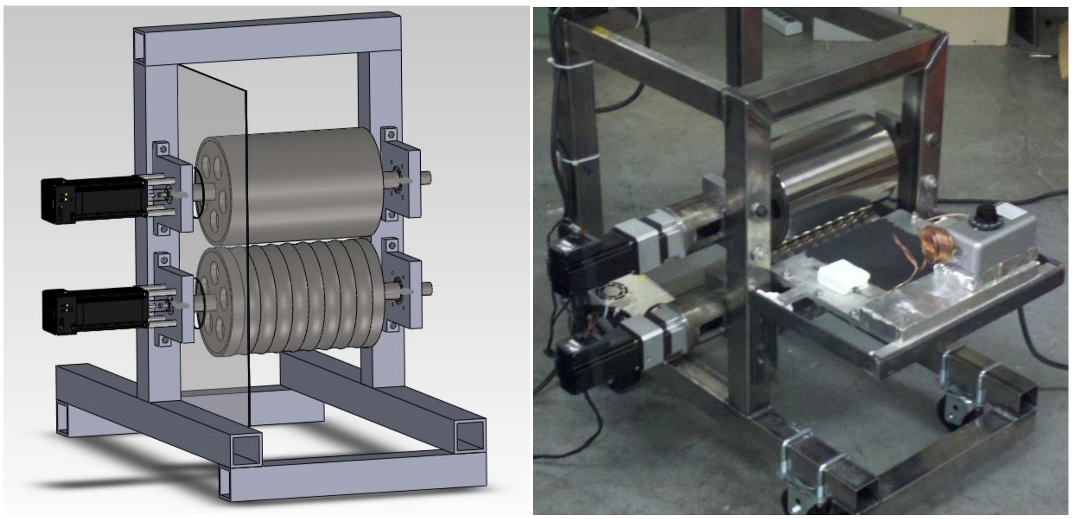

Figure A.1: Roll forming machine design (left) and as-built (right).

High-transmission .25in thick B270 glass pieces were slumped over the lenticulated roller in a test furnace. This resulted in a correctly formed surface on the side in contact with the roller, but an incorrect wavy artifact on the outside curve. THe outer surface was manually ground&polished to a cylinder. This is not a large-volume solution. In scaled production, toroidal lenses could be produced in a process similar to that used to form fluted windows.

Figure A.2: 8”x8” sheets of 0.25” B270 slumped over the lenticulated roller. Mold releases tested include graphite (left) and Boron Nitride (middle). A lens array after slumping (right).

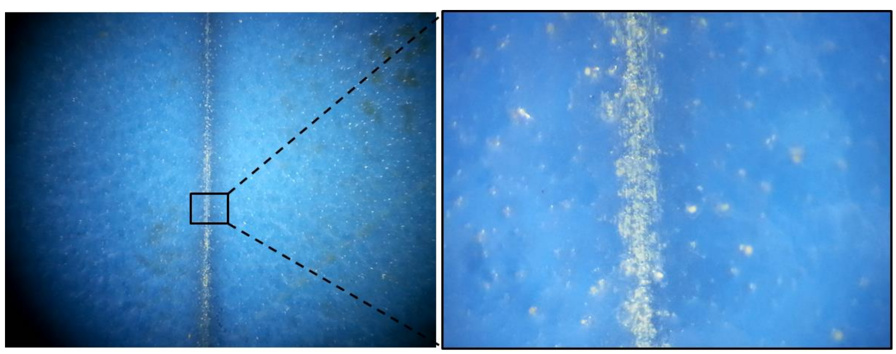

Figure A.3: Magnified images of a cusp between two unpolished banana lens segments. The pits are the result of mold release agents used between the heated glass and stainless steel mold.

# APPENDIX C: TROUGH METROLOGY

The University of Arizona developed a line-scanning reverse-Hartmann test for measuring trough mirror slope errors (Wheelwright B. , Angel, Weiser, Stalcup, & Coughenour, 2013). The LabVIEW-controlled system sequentially fires 56 lasers across the transverse trough plane while monitoring a target screen with a camera. An image processing routine recognizes the location of each reflected beam, allowing a direct slope error calculation. The line then shifts along the linear focus and repeats the measurement to sample the whole aperture. The lasers and target screen move together on a track-mounted arm (Figure B.1). Since this is a direct measurement of slope error, it has very high absolute accuracy. Accuracy was cross-validated against an industry metrology system to within 0.3mrad (see Figure 2.13).

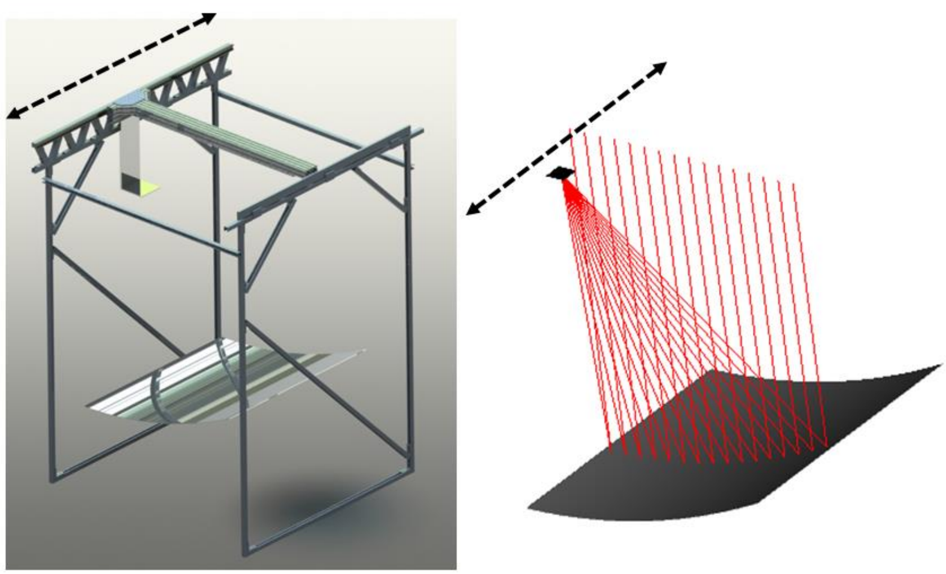

Figure B.1: Line-scanning measurement system(left) and simulated rays to show a single measurement cross-section (right).

Figure B.2 shows two long exposure photos of the system in action. The left photo shows the measurement arm range of motion will all lasers on. In the right photo, a piece of paper is moved through the fan of lasers while the measurement arm is fixed.

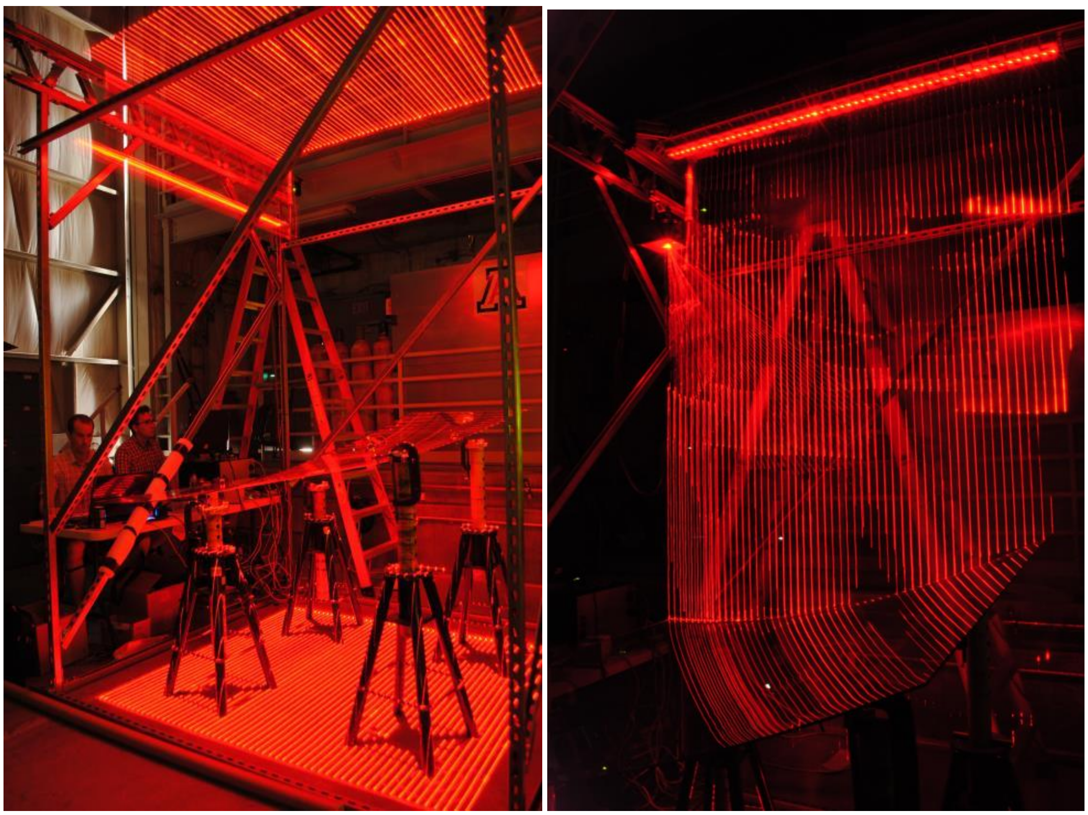

Figure B.2: Long exposure photos of line-scanning laser measurement system.

The laser line is a series of cheap lasers mounted into the spring-loaded lids of enclosures machined into L-shapes for tight interlocking. Adjustment of the three lid screws kinematically defines the laser pointing.

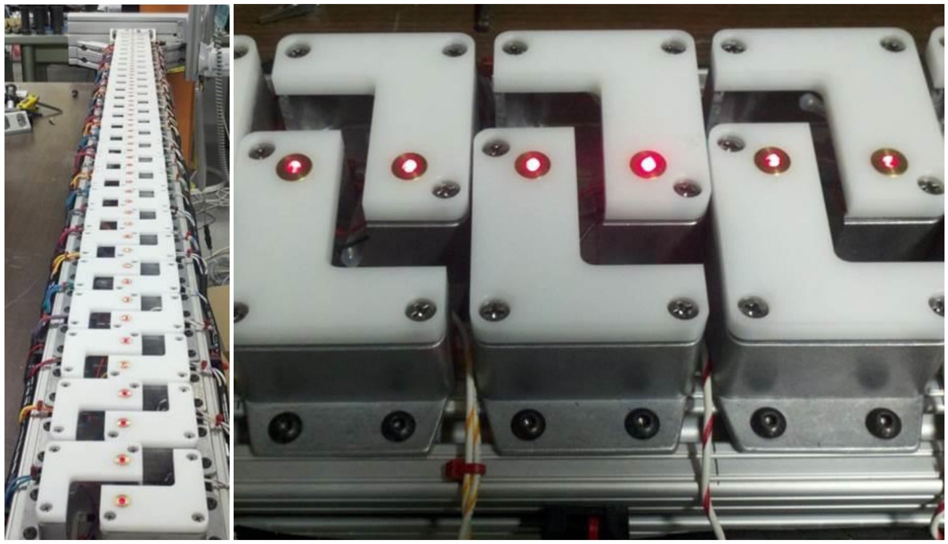

Figure B.3: Laser line mechanical mounting.

Initial calibration is performed by retroreflection from a pan of mineral oil. Each laser is adjusted until the beam reflects back onto itself (Figure B.4).

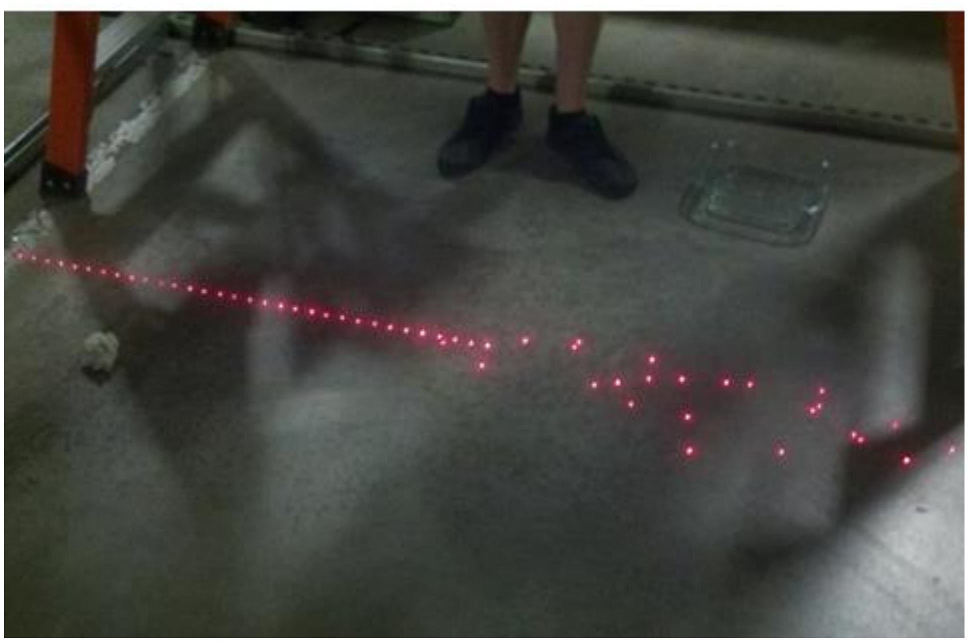

Figure B.4: Partially aligned laser line.

# REFERENCES


Angel, R. (2009). *Patent No. 8350145.* US.

Angel, R., Stalcup, T., Wheelwright, B., Warner, S., Hammer, K., & Frenkel, M. (2014). Shaping solar concentrator mirrors by radiative heating. *Proc. SPIE 9175 High and Low Concentrator Systems for Solar Energy Applications* .

ARPA-E. (2014). *CONCENTRATING SOLAR POWER: ADVANCED PROJECTS OFFERING LOW LCOE OPPORTUNITIES (APOLLO).* US Department of Energy.

ARPA-E. (2014). *Micro-Scale Optimized Solar-Cell Arrays with Integrated Concentration (MOSAIC).* US Department of Energy.

Bendt, P. (1979). *Optical Analysis and Optimization of Line Focus Solar Collectors.* Golden, Co: Department of Energy, Solar Research Institute.

Bird, R. (1981). *A Simplified Clear Sky Model for Direct and Diffuse Insolation on Horizontal Surfaces.* SERI Report No. TR-642-761.

Brunotte, M., Goetzberger, A., & Blieske, U. (1996). Two-stage Concentrator Permitting Concentration Factors Up to 300x with One-Axis Tracking. *Solar Energy* , 56.3: 285-300.

California ISO. (2013). *What the duck curve tells us about managing a green grid.* Folsom, CA.

Collado, F. (2008). Quick evaluation of the annual heliostat efficiency. *Solar Energy* , 82:379-384.

Cooper, T., Ambrosetti, G., Pedretti, A., & Steinfeld, A. (2013). Theory and design of line-to-point focus solar concentrators with tracking secondary optics. *Applied Optics* , 52,35,8586.

Coughenour, B., Stalcup, T., Wheelwright, B., Geary, A., Hammer, K., & Angel, R. (2014). Dish-based high concentration PV system with Köhler optics. *Optics Express* , 22: A211-A224.

CTAER. (2012). *Variable geometry experimental solar facility for central receiver systems*. Retrieved 07 1, 2015, from http://www.ctaer.com/en/infraestructuras/variable-geometry-experimental-solar-facility-central-receiver-systems

Denholm, P., & Mehos, M. (2011). *Enabling Greater Penetration of Solar Power via the Use of CSP with Thermal Energy Storage.* NREL Report No. TP-6A20-52978.

Di Vinadio, A., & Palazzetti, M. (2011). *Patent No. US20110232720.*

Falcone, P. (1986). *A handbook for solar central receiver design.* Sandia National Labs (SAND86-8009).

Fraunhofer ISE. (2015). Retrieved 7 1, 2015, from BINE Information Service: http://www.bine.info/en/newsoverview/news/vierfach-solarzelle-erreicht-rekord-wirkungsgrad/

Google. (2015). Retrieved 07 01, 2015, from Google Maps: https://www.google.com/maps/place/Ivanpah+Solar+Electric+Generating+System/@35.5342623,-115.4521711,2799m

Gossamer Space Frames. (2012, 5). *3M and Gossamer Space Frames to Inaugurate World's Largest Aperture Parabolic Trough Installation- A New Benchmark in Solar Collectors*. Retrieved 07 2015, from http://news.3m.com/es/press-release/company/3m-and-gossamer-space-frames-inaugurate-worlds-largest-aperture-parabolic-trou

Greenpeace International. (2014, 03 17). Retrieved from https://energypedia.info/wiki/Greenpeace_International_Concentrating_Solar_Power_Global_Outlook

Greivenkamp, J. (2004). *Field Guide to Geometrical Optics.* Bellingham, WA, USA: SPIE Press.

Hines, B., & Johnson, R. (2012). *Patent No. WO2012/125751.*

Kasten, F., & Young, A. (1989). REVISED OPTICAL AIR-MASS TABLES AND APPROXIMATION FORMULA. *Applied Optics* , 28(22), 4735-4738.

Koshel, R. (2013). *Illumination Engineering.* London, England: Wiley.

Lentine, A., Nielson, G., Okandan, M., Cruz-Campa, J., & Tauke-Pedretti, A. (2014). Voltage Matching and Optimal Cell Compositions for Microsystem-Enabled Photovoltaic Modules. *IEEE Journal of Photovoltaics* , Vol 4. No.6, 1593-1602.

Luque, A., & Andreev, V. (2007). *Concentrator Photovoltaics.* Berlin: Springer.

Nielson, G., Okandan, M., Cruz-Campa, J., Lentine, A., Sweatt, W., Gupta, V., et al. (2012). Leveraging scale effects to create next-generation photovoltaic systems through micro- and nanotechnologies. *Proc. SPIE 8373: Micro- and Nanotechnology Sensors, Systems, and Applications IV.*

NREL. (2015). *Best Research Cell Efficiencies.*

NREL. (1990). *Solar Radiation Data Manual for Flat-Plate and Concentrating Collectors 1961-1990 Average.*

OASIS. (2015). *Observed Atmospheric and Solar Information System*. Retrieved from http://www.nrel.gov/midc/ua_oasis/

Philipps, S., Bett, W., Horowitz, K., & Kurtz, S. (2015). *CURRENT STATUS OF CONCENTRATOR PHOTOVOLTAIC (CPV) TECHNOLOGY.* NREL & Fraunhofer ISE.

Ruiz Hernandez, V. (2014). *Patent No. US2014/0116419.*

Semprius. (2012, 3 28). Retrieved 07 1, 2015, from http://legacy.pitchengine.com/semprius/semprius-closes-75-million-in-funding

Spectrolab. (2011, 7 12). *C4MJ Metamophic Fourth Generation CPV Technology.* Retrieved from http://www.spectrolab.com/DataSheets/PV/CPV/C4MJ_40Percent_Solar_Cell.pdf

Stalcup, T., Angel, R., Coughenour, B., Wheelwright, B., Connors, T., Davison, W., et al. (2012). On-sun performance of an improved dish-based HCPV system. *Proc. SPIE 8468 High and Low Concentrator Systems for Solar Electric Applications VII.*

Thin Film Center Inc. (2014). Retrieved from http://www.thinfilmcenter.com/

Wang, U. (2012, 6). Ultra-efficient solar. *MIT Technology Review* .

Wheelwright, B., Angel, R., & Coughenour, B. (2014). Freeform lens design to schieve 1000X solar concentration with a parabolic trough reflector. *Proc. SPIE 9293, International Optical Design Conference* .

Wheelwright, B., Angel, R., & Coughenour, B. (2014). Tracking-integrated optics: applications in solar concentration. *Proc. SPIE 9293 International Optical Design Conference.*

Wheelwright, B., Angel, R., Coughenour, B., & Hammer, K. (2014). Freeform solar concentrator with a highly asymmetric acceptance cone. *Proc. SPIE 9175, High and Low Concentrator Systems for Solar Energy Applications IX* .


Wheelwright, B., Angel, R., Coughenour, B., & Hammer, K. (2014). Freeform solar concentrator with a highly asymmetric acceptance cone. *Proc. SPIE 9175, High and Low Concentrator Systems for Solar Energy Applications IX* .

Wheelwright, B., Angel, R., Coughenour, B., Hammer, K., Geary, A., & Stalcup, T. (2014). Field weighting model for tracking-integrated optics. *CPV-10 (AIP 1616)*, (pp. 237-241).

Wheelwright, B., Angel, R., Weiser, J., Stalcup, T., & Coughenour, B. (2013). A Line-Scanning Laser Hartmann Test for Parabolic Trough Mirrors. *OSA Renewable Energy and the Environment.*

Winston, R., & Zhang, W. (2010). Pushing concentration of stationary solar concentrators to the limit. *Optics Express* , 18.9, 64-72.

Winston, R., Minano, J., & Benitez, P. (2005). *Nonimaging Optics.* Burlington, MA, USA: Elsevier Academic Press.

Yu, Z., Fisher, K., Wheelwright, B., Angel, R., & Holman, Z. (2015). PVMirror: A New Concept for Tandem Solar Cells and Hybrid Solar Converters. *IEEE J. Photovoltaics* .

Yu, Z., Wheelwright, B., Angel, R., & Holman, Z. (2015). Silicon wafers with optically specular surfaces formed by chemical polishing. *In Preparation* .